

A Finite Element Method for Poroelasticity: Theory and Application to Lung Modelling



Lorenz Berger
Keble College
University of Oxford

A thesis submitted for the degree of
Doctor of Philosophy
Michaelmas Term 2014

Abstract

Modelling tissue deformation or ventilation in the lung separately does not give a good indication of how the integrated organ works, this is because both components are interdependent. To gain a better understanding of the biomechanics in the lung it is therefore necessary to fully couple the tissue deformation with the ventilation. To achieve this tight coupling between the tissue deformation and the ventilation we propose a multiscale lung model that approximates the lung parenchyma by a biphasic (tissue and air) poroelastic model, that is coupled to a fluid network model of the airways.

In this thesis we develop a stabilized finite element method for solving the equations of poroelasticity to enable such a computational lung model. For the proposed numerical scheme, we use the lowest possible approximation order: piecewise constant approximation for the pressure, and piecewise linear continuous elements for the displacements and fluid flux. Due to the discontinuous pressure approximation, sharp pressure gradients due to changes in material coefficients or boundary layer solutions can be captured reliably. We begin by developing theoretical results for approximating the linear poroelastic equations valid in small deformations. In particular, we prove existence and uniqueness, an energy estimate and an optimal a-priori error estimate for the discretized problem. We then extend this work and construct a stabilized finite element method to solve the poroelastic equations valid in large deformations. We present the linearization and discretisation for this nonlinear problem, and give a detailed account of the implementation. We rigorously

test both the linear and nonlinear finite element method using numerous test problems to verify theoretical stability and convergence results, and the method's ability to reliably capture steep pressure gradients.

Finally, we derive a poroelastic model for lung parenchyma coupled to an airway fluid network model, and develop a stable method to solve the coupled model. Numerical simulations, on a realistic lung geometry, illustrate the coupling between the poroelastic medium and the network flow model, and simulations of tidal breathing are shown to reproduce global physiologically realistic measurements. We also investigate the effect of airway constriction and tissue weakening on the ventilation, tissue stress and alveolar pressure distribution.

Publications

Below are a list of publications which directly relate to the work described in this thesis.

- **L. Berger**, R. Bordas, D. Kay, and S. Tavener; Stabilized low-order finite element approximation for linear three-field poroelasticity *SIAM Journal on Scientific Computing (Under Review)*
- **L. Berger**, R. Bordas, D. Kay, and S. Tavener; A stabilized nonlinear finite element method for three-field incompressible poroelasticity valid in large deformations *Computer Methods in Applied Mechanics and Engineering (Under Review)*
- **L. Berger**, R. Bordas, K. Burrowes, V. Grau, D. Kay; A poroelastic model of the lung *Journal of Computational Physics (Under Review)*

Conference Presentations

The work described in this thesis was presented at the following international conferences:

- **L. Berger**, R. Bordas, K. Burrowes, C. Brightling, R. Hartley, D. Kay; Understanding The Interdependence Between Parenchymal Deformation And Ventilation In Obstructive Lung Disease, *The American Thoracic Society conference, San Diego, May 2014. (Poster)*
- **L. Berger**, R. Bordas, D. Kay; Solving the Generalised Large Deformation Poroelastic Equations for Modelling Tissue Deformation and Ventilation in the Lung, *European Numerical Mathematics and Advanced Applications conference, EPFL, Lausanne, August 2013. (Oral)*

Contents

1	Introduction	1
1.1	Thesis motivation	1
1.2	Thesis goals	4
1.3	Thesis structure and contributions	5
2	Background	8
2.1	Lung physiology	8
2.1.1	Mechanics of breathing	8
2.1.2	Airway tree	9
2.1.3	Lung parenchyma	11
2.1.4	The diseased lung	12
2.2	Computational lung models	14
2.3	Poroelastic models for lung parenchyma and other biological tissue	15
2.4	Finite element methods for poroelasticity	17
2.4.1	Linear three-field discretisations	18

2.4.2	Discretisations valid in large deformations	20
3	Poroelasticity theory	21
3.1	Kinematics	22
3.2	Volume fractions	26
3.3	Conservation of mass	28
3.4	Conservation of momentum	29
3.5	Constitutive relations	30
3.6	Summary of the general poroelasticity model	32
3.7	Simplification and reformulation of the model	35
3.8	Linear poroelasticity	36
4	Finite element method	39
4.1	Introduction	39
4.2	Norms and spaces	40
4.3	Model problem	42
4.3.1	Weak formulation	43
4.3.2	Time discretisation	44
4.3.3	Finite element discretisation	45
4.4	Mixed methods	48
5	Stabilized low-order finite element approximation for linear three-field poroelasticity	53
5.1	Introduction	53

5.2	The poroelastic model	55
5.2.1	Governing equations	55
5.2.2	Weak formulation	56
5.2.3	Fully-discrete model	58
5.3	Norms and inequalities	60
5.3.1	Useful inequalities	60
5.3.2	J-norm	61
5.3.3	Approximation results	62
5.3.4	Triple-norms	64
5.4	Existence and uniqueness of solutions to the fully-discrete model	64
5.5	Energy estimate for the fully-discrete model	71
5.5.1	Bound on the displacement, fluid flux and pressure . .	71
5.5.2	Bound on the divergence of the fluid flux	75
5.5.3	The energy estimate	80
5.6	A-priori error analysis	80
5.6.1	Galerkin orthogonality	82
5.6.2	Auxiliary error estimates	83
5.6.3	The a priori error estimate	88
5.7	Implementation	89
5.7.1	Algorithm to assemble the stabilization matrix	90
5.8	Numerical Results	91
5.8.1	2D test problem	92
5.8.2	3D test problem	96

5.8.3	2D cantilever bracket problem	98
5.8.4	3D unconfined compression stress relaxation	99
5.9	Conclusion	102
6	A stabilized finite element method for nonlinear poroelasticity valid in large deformations	104
6.1	Introduction	104
6.2	The model	105
6.3	The stabilized finite element method	106
6.3.1	Weak formulation	106
6.3.2	The fully discrete model	107
6.3.3	Newton's Method	108
6.4	Implementation details	112
6.4.1	Newton algorithm	112
6.4.2	No-flux boundary condition	114
6.5	Numerical results	115
6.5.1	3D unconfined compression stress relaxation	116
6.5.2	Terzaghi's problem	118
6.5.3	Swelling test	122
6.6	Conclusion	124
7	A poroelastic-fluid-network model of the lung	126
7.1	Introduction	126
7.2	Lung model assumptions	127

7.2.1	Approximating lung parenchyma using a poroelastic medium	127
7.2.2	Approximating the airways using a fluid network model	130
7.3	Mathematical model	130
7.3.1	A poroelastic model for lung parenchyma	130
7.3.2	A network flow model for the airway tree	131
7.3.3	Summary of the coupled lung model.	135
7.4	Implementation	136
7.4.1	Discrete coupling of the fluid network to the poroelastic model	137
7.4.2	Finite element matrices	138
7.5	Model generation	140
7.5.1	Mesh generation	140
7.5.2	Reference state, boundary conditions and initial conditions	140
7.5.3	Simulation parameters	142
7.6	Model exploration	143
7.6.1	Normal breathing	143
7.6.2	Breathing with airway constriction	147
7.6.3	Breathing with locally weakened tissue	151
7.6.4	Dynamic hysteresis	152
7.7	Discussion	155

7.7.1	Contributors of airway resistance and tissue mechanics to lung function	156
7.7.2	Limitations and future work	157
7.8	Conclusion	160
8	Conclusion	161
8.1	Review and remarks	161
8.2	Future work	163
8.2.1	Numerics	163
8.2.2	Applications	164
A	Appendix	167
A.1	Spatial tangent modulus	167
A.2	Matrix Voigt notation	168
A.3	Neo-Hookean strain energy	169

Chapter 1

Introduction

1.1 Thesis motivation

The main function of the lungs is to exchange gas between air and blood, supplying oxygen during inspiration and removing carbon dioxide by subsequent expiration. Gas exchange is optimised by ensuring efficient matching between ventilation and blood flow, the distributions of which are largely governed by tissue deformation, gravity and branching structure of the airway and vascular trees. In this work, we focus on the link between tissue deformation and ventilation. Understanding the interdependence between structure, and mechanical function in the lung has traditionally relied on direct measurement or medical imaging. Limitations of these approaches include difficulty in isolating a specific subsystem from its influence on the rest of the organ to gain an indepth understanding of the underlying mechanics.

A carefully constructed computational model provides the advantage of exact control over functional parameters and the geometry of the solution domain, allowing for investigations into complex functional mechanisms. The work developed in this thesis is part of a longer term aim to link detailed anatomic imaging to computational analysis of structure-function relationships in the integrated pulmonary system through computational modelling of the lung and airway tree [91].

Previous work has typically focused on modelling either ventilation or tissue deformation in isolation. However evaluation of each component (i.e. tissue deformation and ventilation) separately does not necessarily give accurate ventilation predictions or provide a good indication of how the integrated organ works, this is because both components are interdependent. To gain a better understanding of the biomechanics in the lung it is therefore necessary to fully couple the tissue deformation with the ventilation. To achieve this tight coupling between the tissue deformation and the ventilation we propose a multiscale model that approximates the lung parenchyma by a biphasic (tissue and air, ignoring blood) poroelastic model, that is then coupled to an airway fluid network model.

An integrated model of ventilation and tissue mechanics will be particularly important for understanding respiratory diseases since nearly all pulmonary diseases lead to some abnormality of lung tissue mechanics [88]. For example, chronic obstructive pulmonary disease (COPD) encompasses emphysema (destruction of alveolar tissue) and chronic bronchitis which can

cause severe, airway remodelling, bronchoconstriction and air trapping, all of which can significantly alter tissue properties. If the tissue mechanics are affected so too will the ventilation and vice versa, again emphasising the importance of a model that fully couples the ventilation and tissue mechanics in the lung. The impact of alterations during disease, such as airway narrowing or changes in tissue properties, on regional ventilation and tissue stresses are not well understood. For example, one hypothesis is that airway disease may precede emphysema [39]. The computational lung model could be applied to investigate the impact of airway narrowing and tissue stiffness during obstructive lung diseases on tissue stresses, alveoli pressure and ventilation.

Developing such a fully coupled model has to our knowledge not yet been achieved. There are many difficulties involved in creating a model that is physiologically accurate and can be solved numerically. We will need to develop methodology to solve the poroelastic equations, and develop solution techniques to couple the poroelastic model to the airway fluid network model.

In particular, in the diseased lung, abrupt changes in tissue properties and heterogeneous airway narrowing are possible. This can result in a patchy ventilation and pressure distribution [95]. In this situation existing methods that solve the poroelastic equations using a continuous pressure approximation would struggle to capture the steep gradients in pressure, and result in localized oscillations in the pressure. By developing a method that utilises a discontinuous approximation for the pressure we will be able to approximate these steep pressure gradients reliably, and avoid localized oscillations in the

pressure.

The proposed methodology could also be adapted to model other biological tissues where blood vessels flow through and interact with a deforming tissue. For example, when modelling perfusion of blood flow in the beating myocardium [23, 26], modelling brain oedema [66] or hydrocephalus [105], or microcirculation of blood and interstitial fluid in the liver lobule [62]. In addition to this poroelasticity theory has also been used in various geomechanical applications ranging from reservoir engineering [79] to modelling earthquake fault zones [103]. The theory developed in this thesis could be applied in these fields.

1.2 Thesis goals

The main goal of this thesis is to rigorously develop a finite element method for solving the poroelastic equations, and then use this methodology to simulate the lung breathing on a realistic geometry. More specific targets are:

1. Develop a practical low-order finite element method for solving the linear poroelastic equations using a discontinuous pressure approximation. Prove theoretical results about the discretisation, including existence and uniqueness, an energy estimate and an optimal a-priori error estimate.
2. Extend the method to a non-linear finite element method to solve the poroelastic equations valid in large deformations.

3. Rigorously test the method using numerous test problems to verify theoretical stability and convergence results, and its ability to reliably capture steep pressure gradients.
4. Derive a poroelastic model for lung parenchyma coupled to an airway fluid network model, and develop a stable method to numerically solve the coupled model.
5. Solve the computational lung model on a realistic geometry, with boundary conditions extracted from imaging data, to simulate breathing. Evaluate the effect of tissue weakening and airway narrowing on lung function.

1.3 Thesis structure and contributions

The contributions of each chapter to the thesis are as follows:

Chapter 2: We give a brief overview of lung physiology, review the literature on ventilation models and existing porelastic models, and discuss numerical methods currently available to solve the poroelastic equations.

Chapter 3: We introduce the general theory of poroelasticity valid in large deformations, and state the linear poroelastic equations, valid in small deformations.

Chapter 4: We outline the basic concepts of the standard continuous Galerkin finite element method. We then discuss mixed problems and their stability requirement.

Chapter 5: A stabilized finite element method for the linear three-field (displacement, fluid flux and pressure) poroelasticity problem is presented. By applying a local pressure jump stabilization term to the mass conservation equation we avoid pressure oscillations. For the fully discretized problem we prove existence and uniqueness, an energy estimate and an optimal a-priori error estimate. Numerical experiments in 2D and 3D illustrate the convergence of the method, show the effectiveness of the method to overcome spurious pressure oscillations, and evaluate the added mass effect of the stabilization term.

Chapter 6: We apply the method developed in Chapter 5 to solve the three-field nonlinear quasi-static incompressible poroelasticity problem valid in large deformations. We present the linearization and discretisation of the equations, and give a detailed account of the implementation. Numerical experiments in 3D verify the method and illustrate its ability to reliably capture steep pressure gradients.

Chapter 7: We present the model assumptions required for the proposed

poroelastic lung model and outline its mathematical formulation and coupling to the airway fluid network. A numerical method is presented to discretize the equations in a monolithic way to ensure unconditional stability. Finally, numerical simulations on a realistic lung geometry that illustrate the coupling between the poroelastic medium and the network flow model are presented. Simulations of tidal breathing are shown to reproduce global physiologically realistic measurements. We also investigate the effect of airway constriction and tissue weakening on the ventilation, tissue stress and alveolar pressure distribution.

Chapter 8: We summarise the main results and propose future lines of research.

Chapter 2

Background

2.1 Lung physiology

We will now give a basic review of lung physiology. A more complete introduction can be found in [27, 101].

2.1.1 Mechanics of breathing

During inspiration, the volume of the thoracic cavity increases and air is drawn into the lung by creating a sub-atmospheric pressure distribution. The increase in volume is brought about mainly by contraction of the diaphragm, which causes it to descend, and partly by the action of the intercostal muscles, which raise the ribs. The lung is elastic and subsequently returns passively to its preinspiratory volume during resting breathing. During expiration the intra-alveolar pressure becomes slightly higher than atmospheric pressure

and gas flows out of the lungs [101].

2.1.2 Airway tree

The airway tree is divided into a conducting zone and a respiratory zone. The trachea divides into right and left main bronchi, which in turn divide into lobar and then segmental bronchi. This process continues down to the terminal bronchioles, which are the smallest airways without alveoli. All of these bronchi make up the conducting airways. The terminal bronchioles, which appear at around generation 15-16, then continue to divide into respiratory bronchioles, which have occasional alveoli budding from their walls. Finally, we get to the alveolar ducts, which are completely lined with alveoli, see Figure 2.1a. This alveolated region of the lung where the gas exchange occurs is known as the respiratory zone [101]. Table 2.1 documents the different flow characteristics found in the airway tree during slow and rapid breathing.

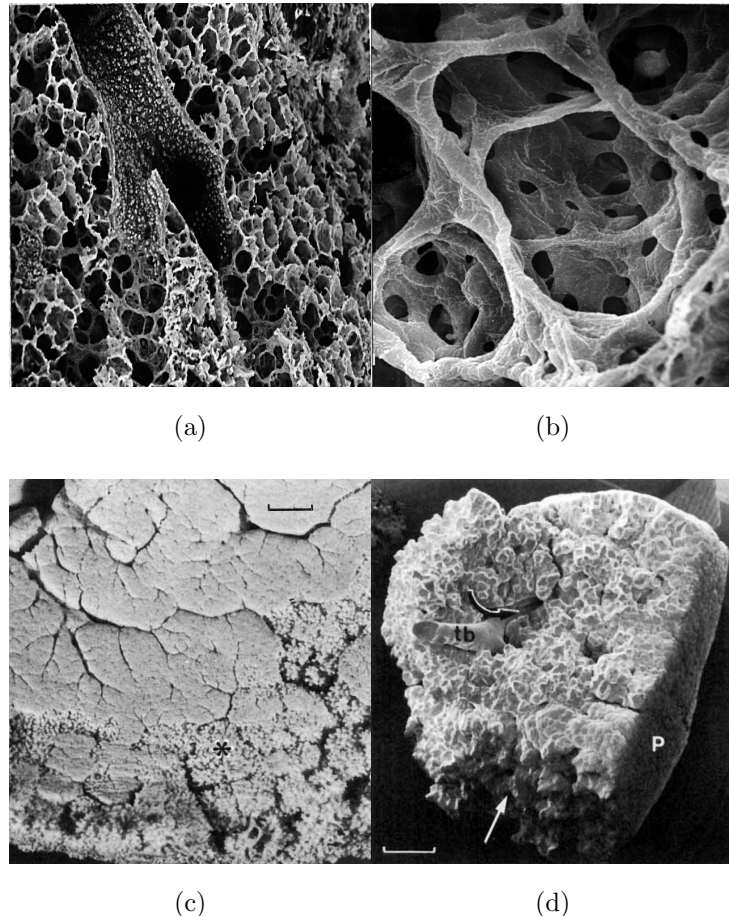


Figure 2.1: (a) Transition from terminal bronchiole to alveolar duct, from conducting airway to oxygen transfer area, diameter of terminal bronchiole is 0.5 mm. (b) A few alveoli in an alveolar duct. The dark round openings are pores between alveoli. The alveolar wall is quite thin and contains a network of capillaries. The average diameter of one alveoli is 0.2 mm. (c) Portions of silicone rubber casts of upper lobes of human lungs; asterisk marks incompletely filled regions. The outline of individual unfilled acinar units can also be seen. Scale marker, 5 mm. (d) Scanning electron micrograph of complete acinus with transitional bronchiole (tb) and surface abutting on pleura (P). Note the irregular surface where alveolar sacs of adjacent acini interdigitate (straight arrow). Scale marker, 1 mm. Images are reproduced from [59].

Generation	Diameter cm	Length cm	Flow rate 10L/min Velocity (m/s)	Re	Flow rate 100L/min Velocity (m/s)	Re
Trachea	1.80	12.0	65.8	775	658	7750
1	1.22	4.76	71.6	573	716	5730
5	0.35	1.07	53.6	123	536	1230
10	0.13	0.46	12.55	10.6	125	106
15	0.066	0.20	1.48	0.63	14.8	6.30
20	0.045	0.083	0.10	0.031	1.00	0.31

Table 2.1: Shows dimensions, velocity and the corresponding Reynolds number for different sections of the airway tree during slow and rapid breathing. These values have been taken from [78].

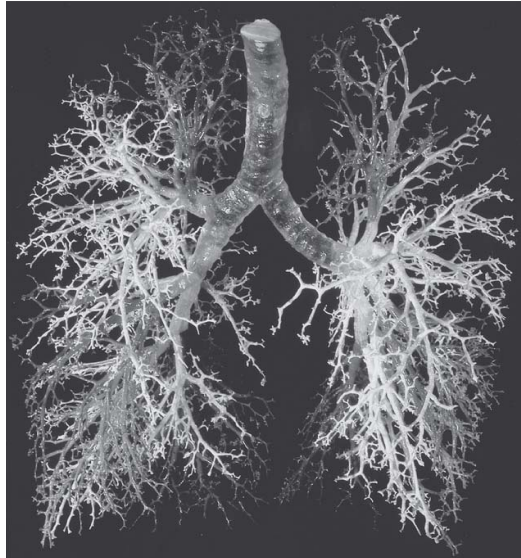


Figure 2.2: A rubber cast of the conducting airways of a human lung. The image is reproduced from [101].

2.1.3 Lung parenchyma

Lung parenchyma refers to the portion of the lung made up of the small air chambers (alveoli) participating in gas exchange. The alveoli are made up of

collagen, elastin fibers and membranous structures containing the capillary network, see Figure 2.1b. Alveoli are arranged in sponge like structures and fill the entire volume of the lungs surrounding the conducting passages. Figure 2.1c shows a rubber cast of lung parenchyma, the dark lines outline the branching structure of the airways. The right and left lung are partitioned into three and two lobes, respectively. Lung segments of conic shape are then the first subdivision of these lobes. These structures are bounded by connective tissue such that surgical separation is often possible. In the right lung, there are usually ten segments whereas only nine can be found in the left lung. Within the segments, the bronchi branch about six to twelve times. The terminal bronchioles which appear after roughly 15–16 branching generations then finally feed into approximately 30,000 so-called acini, see Figure 2.1d. These acini represent the largest lung units of which all airways are alveolated and thus participate in gas exchange [99].

2.1.4 The diseased lung

There exist numerous ways in which the mechanical function of the lung can be altered. In this section we will briefly describe pulmonary fibrosis, emphysema, and airway constriction.

Pulmonary fibrosis is a so-called restrictive diseases. Here, abnormal deposition and organization of connective proteins, particularly collagen, leaves lung tissue scarred and stiff with with compliance values decreasing to 20% of normal values [12, 27]

Emphysema is characterized by an abnormal, permanent enlargement of air spaces distal to the terminal bronchioles and the destruction of their walls associated with loss of the elastic connective tissue. Large areas of lung tissue completely break down leaving big holes, see Figure 2.3. This results in a reduced area for gas exchange and a reduction in the elastic recoil of the lungs.

Airway constriction, which occurs in asthma and COPD, changes airway resistance patterns. The level of airway resistance is sensitive to disease in the lungs. Narrowing of the airways can be caused through various mechanisms such as the airway inflammation or bronchoconstriction observed in asthma, mucous hyper-secretion and inflamed bronchi observed in chronic bronchitis, or the flaccid airways observed in emphysema [45]. This decrease in airway radius can significantly increase the resistance to flow.

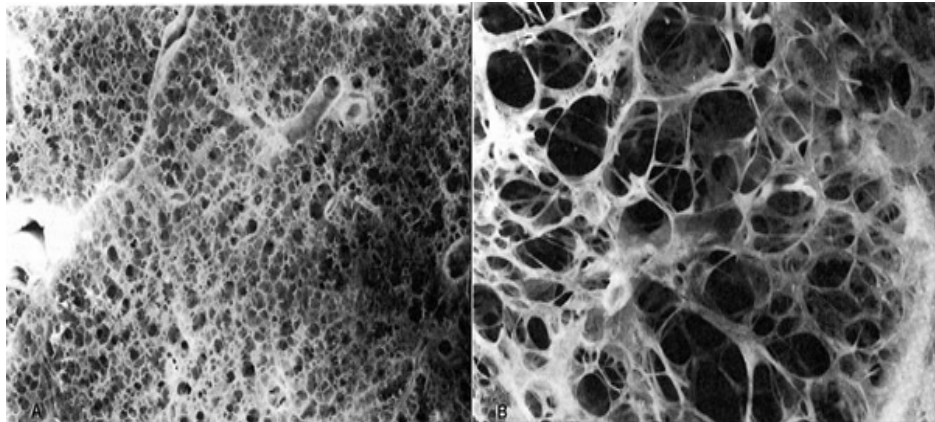


Figure 2.3: Left, a cross section of healthy parenchyma. Right, a cross section of diseased (emphysemic) lung parenchyma, with big holes appearing. Images are reproduced from G. Snell, ctsnet.org.

2.2 Computational lung models

There exist a large number of computational ventilation and deformation models for the lung. Some models are designed to model particular phenomena whilst others are more general. They also range in spatial complexity from 0D compartment type models to 3D models which are able to incorporate ‘patient-specific’ geometries extracted from CT images. In this review, we will focus on models that couple ventilation with tissue deformation and can be used as patient-specific models. One study that couples ventilation and tissue deformation using a one way coupling approach is described in [90]. Here a mechanics model for lung tissue is used to provide flow boundary conditions at terminal branches for an airway model. This makes the resultant ventilation distribution dependent on the tissue deformation, for example due to gravity. Other sophisticated models of the whole lung that model ventilation and tissue deformation also exist [49, 89]. Here the tissue is modelled by many independent elastic alveolar units. There is no clear way to conserve mass locally, so alveolar units can expand irrespectively of the size and position of neighbouring units. In reality the acini do not function as independent elastic balloons. They are physically coupled through fibrous scaffolding and shared alveolar septa. In our proposed model the tissue is modelled as one continuum, thus allowing us to conserve volume and couple neighbouring units. This is illustrated in Figure 2.4. Also, these lung models [49, 89] give information about the distribution of flow within the lung as

a result of a pleural pressure boundary condition. However it is not possible to experimentally measure the pleural pressure *in vivo* using imaging or other apparatus. As part of the simulation protocol, the pleural pressure is therefore often tuned until physiological realistic flow rates are achieved. To overcome this issue, [108, 109] proposed to estimate the flow boundary conditions for full organ ventilation models by means of image registration. However by solely relying on image registration to determine the ventilation distribution within the tissue one is not able to model the change in ventilation distribution due to progression of disease. In Chapter 7 we will build on [108] by integrating image registration based boundary conditions within the proposed poroelastic model of lung deformation. In particular, we propose to register expiratory images to the inspiratory images, to yield an estimate of the deformation boundary condition for the lung surface, and drive the simulation through this deformation boundary condition. Thus the tissue deformation and subsequent flow boundary condition for tree branches inside the lung and ventilation distribution is not pre-determined, but calculated from the coupled poroelastic-airway-tree model.

2.3 Poroelastic models for lung parenchyma and other biological tissue

Some early work on a mechanical model of lung parenchyma as a poroelastic medium has already been proposed in [55]. This work developed a similar

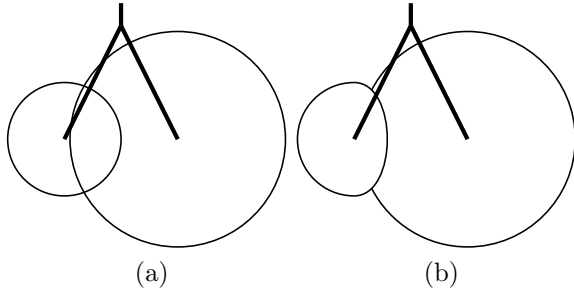


Figure 2.4: Sketch of two balloon models where the right unit is more compliant, thus being able to expand more easily. (a) Balloon model with independent alveolar units. The overlap in the alveolar units illustrates that mass is not conserved. (b) Balloon model where the alveolar units are coupled. Here the inflation of each alveolar unit is compromised by the expansion of its neighbor.

poroelastic model to the one we propose, however it has only been applied to a very simple 2D geometry. Also in [75] homogenisation theory has been used to derive macroscopic poroelastic equations for average air flows and tissue displacements in lung parenchyma during high frequency ventilation. The resulting model is a system of ordinary differential equations that is used to investigate the effect of high-frequency ventilation on strain in the parenchymal tissue. The use of a poroelastic model has also been applied to modelling other biological tissues. For example modelling protein based hydrogels embedded with cells [41], perfusion of blood flow in the beating myocardium [23, 26], the modelling of brain oedema (swelling) [66] and hydrocephalus [105]. Another application is the modelling of interstitial fluid and tissue in articular cartilage and intervertebral discs [40, 47, 72].

2.4 Finite element methods for poroelasticity

The method that we use for spatially discretising the equations in this work is the finite element method (FEM).

After many decades of research there remain numerous challenges associated with the numerical solution of the poroelastic equations. When using the finite element method the main challenge is to ensure stability and convergence of the method and prevent numerical instabilities that often manifest themselves in the form of spurious oscillations in the pressure. It has been suggested that this problem is caused by the saddle point structure in the coupled equations resulting in a violation of the famous Ladyzhenskaya-Babuska-Brezzi (LBB) condition, thus highlighting the need for a stable combination of mixed finite elements [43]. In addition to this, there has been a need for a method that is able to overcome localized pressure oscillations due to steep pressure gradients in the solution. Another numerical challenge in practical 3D applications is the algebraic system arising from the finite element discretisation. This can lead to a very large matrix system that has many unknowns and is severely ill-conditioned, making it difficult to solve using standard iterative solvers. Therefore low-order finite element methods that allow for efficient preconditioning are preferable [36, 104].

2.4.1 Linear three-field discretisations

The poroelastic equations are often solved in a reduced displacement and pressure formulation, from which the fluid flux can then be recovered [73, 103]. [73] have analysed the stability and convergence of this reduced displacement pressure (\mathbf{u}/p) formulation and were able to show error bounds for inf-sup stable combinations of finite element spaces (e.g. Taylor-Hood elements). In this work we will keep the fluid flux variable resulting in a three-field, displacement, fluid flux, and pressure formulation. Keeping the fluid flux as a primary variable has the following advantages:

- i It allows for greater accuracy in the fluid velocity field. This can be of interest whenever a poroelastic model is coupled with an advection diffusion equation, e.g. to account for gas exchange, thermal effects, contaminant transport or the transport of nutrients or drugs within a porous tissue [52].
- ii Physically meaningful boundary conditions can be applied at the interface when modelling the interaction between a fluid and a poroelastic structure [10].
- iii It allows for an easy extension of the fluid model from a Darcy to a Brinkman flow model, for which there are numerous applications in modelling biological tissues [52].
- iv It reduces the order of the spatial derivative of the pressure, allowing for

a discontinuous pressure approximation without any additional penalty terms.

- v It avoids the calculation of the fluid flux in post-processing.

Error estimates have been proven in [79, 80] for solving the three-field formulation problem using continuous piecewise linear approximations for displacements and mixed low-order Raviart Thomas elements for the fluid flux and pressure variables. However this method was found to be susceptible to spurious pressure oscillations [81]. To overcome these pressure oscillations, [65] analysed a discontinuous three-field method with moderate success, and [107] analysed a nonconforming three-field method. However no implementation of these methods in 3D has yet been presented. We hypothesize that this is due to the complexity of these non-standard elements used, making it very difficult to include them in existing finite element codes.

In addition to these monolithic approaches there has been considerable work on operating splitting (iterative) approaches where the poroelastic equations are separated into a fluid problem and deformation problem [35, 53, 102]. Although these methods are often able to take advantage of existing elasticity and fluid finite element software, and result in solving a smaller system of equations, these schemes are often only conditionally stable. To ensure that the method is unconditionally stable, monolithic approaches are often preferred. Within this work we will propose a method that is monolithic and therefore retains the advantage of being unconditionally stable.

2.4.2 Discretisations valid in large deformations

We will now give a brief overview of different approaches for solving the poroelastic equations valid in large deformations. There has been some work on operating splitting (iterative) approaches [23]. Again, this approach is only conditionally stable. Some notable quasi-static incompressible large deformation monolithic approaches include a mixed-penalty formulation, and a mixed solid velocity-pressure formulation, both outlined in [3], the solid velocity-pressure formulation is similar to the commonly used reduced (\mathbf{u}/p) formulation [8]. These two-field formulations require a stable mixed element pair such as the popular Taylor-Hood element to satisfy the LBB inf-sup stability requirement. The key difficulty, however, that these elements cannot escape is that jumps in material coefficients may introduce large solution gradients across the interface, requiring severe mesh refinement. This is because a continuous pressure element is used, which is unable to reliably capture jumps in the pressure solution [103]. In [63] a three-field (displacement, fluid flux, pressure) formulation has been outlined, however this method uses a low-order mixed finite element approximation without any stabilization and therefore is not inf-sup stable. A dynamic three-field finite element using a continuous pressure approximation has been implemented in [97].

Chapter 3

Poroelasticity theory

Two complementary approaches have been developed for modelling a deformable porous medium. Mixture theory, also known as the Theory of Porous Media (TPM) [1, 15, 18], has its roots in the classical theories of gas mixtures and makes use of a volume fraction concept in which the porous medium is represented by spatially superposed interacting media. An alternative, purely macroscopic approach is mainly associated with the work of Biot, a detailed description can be found in the book by Coussy [28]. Relationships between the two theories are explored by [29]. As is most common in biological applications, we use the mixture theory for poroelasticity as outlined in [15].

3.1 Kinematics

Within the theory of continuum mixture theory, a poroelastic medium is treated as the superposition of two interacting continua simultaneously occupying the same physical space. The superscript $\alpha \in \{s, f\}$ denotes a quantity related to the solid or fluid, respectively. Before presenting the mixture theory, we give a review of solid mechanics. This will form the basis of the description of the solid skeleton. The following review of continuum mechanics closely follows Chapter 4 in [42], and the standard Poromechanics book by [28].

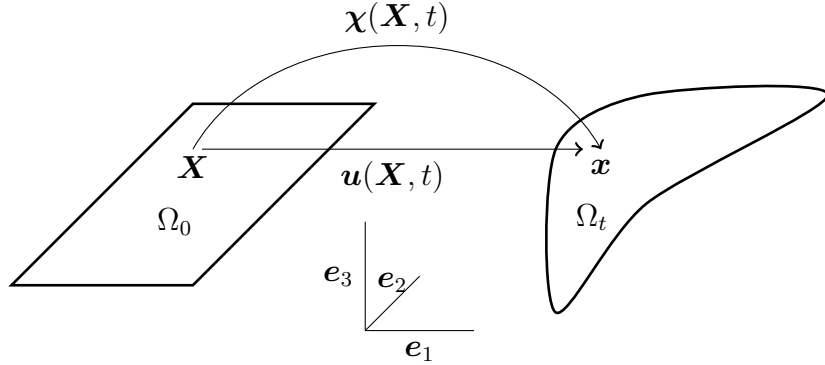


Figure 3.1: Illustration of the solid deformation.

Let the volume Ω_0 be the undeformed Lagrangian (material) reference configuration and let $\mathbf{X} = \{X\mathbf{e}_1 + Y\mathbf{e}_2 + Z\mathbf{e}_3\}$ indicate the position of a solid particle in Ω_0 at $t = 0$, where X, Y and Z are the components of the position with respect to the standard orthonormal basis $\{\mathbf{e}_1, \mathbf{e}_2, \mathbf{e}_3\}$ for \mathbb{R}^3 . The position of a solid particle in the current Eulerian (spatial) configuration

Ω_t is given by $\mathbf{x} = \{x\mathbf{e}_1 + y\mathbf{e}_2 + z\mathbf{e}_3\}$, with $\mathbf{x} = \chi(\mathbf{X}, t)$, shown in Figure 3.1. The deformation map, $\chi(\mathbf{X}, t)$, is a continuously differentiable, invertible mapping from Ω_0 to Ω_t . Thus the inverse of the deformation map, $\chi^{-1}(\mathbf{x}, t)$, is such that $\mathbf{X} = \chi^{-1}(\mathbf{x}, t)$. The displacement field is given by

$$\mathbf{u}(\mathbf{X}, t) = \chi(\mathbf{X}, t) - \mathbf{X}. \quad (3.1)$$

The deformation gradient tensor is

$$\mathbf{F} = \frac{\partial \chi(\mathbf{X}, t)}{\partial \mathbf{X}} = \mathbf{I} + \frac{\partial \mathbf{u}(\mathbf{X}, t)}{\partial \mathbf{X}}, \quad (3.2)$$

and maps a material line element in the reference configuration $d\mathbf{X}$, to a line element $d\mathbf{x}$ in the current configuration, i.e. $d\mathbf{x} = \mathbf{F}d\mathbf{X}$. The symmetric right Cauchy-Green deformation tensor is given by

$$\mathbf{C} = \mathbf{F}^T \mathbf{F}. \quad (3.3)$$

The Jacobian is defined as

$$J = \det(\mathbf{F}), \quad (3.4)$$

and represents the change in an infinitesimal small volume from the reference to the current configuration. Also note that $J > 0$, to avoid self penetration of the body. We also have that J represents the change in an infinitesimal small volume from a reference volume element $d\Omega_0$ to a current configuration

volume element $d\Omega_t$

$$d\Omega_t = J d\Omega_0. \quad (3.5)$$

Also, \mathbf{F} is invertible, and it is easy to see that the inverse of the deformation gradient is the deformation gradient of the inverse map

$$\mathbf{F}^{-1} = \frac{\partial \boldsymbol{\chi}^{-1}(\mathbf{x}, t)}{\partial \mathbf{x}} = \frac{\partial \mathbf{X}}{\partial \mathbf{x}}. \quad (3.6)$$

We denote by $\mathbf{V}(\mathbf{X}, t)$ the velocity at time t of the material (fixed) solid particle \mathbf{X} . By definition we have

$$\mathbf{V}(\mathbf{X}, t) = \frac{\partial}{\partial t} \boldsymbol{\chi}(\mathbf{X}, t). \quad (3.7)$$

Similarly, we denote by $\mathbf{A}(\mathbf{X}, t)$ the acceleration of the material solid particle, given by

$$\mathbf{A}(\mathbf{X}, t) = \frac{\partial^2}{\partial t^2} \boldsymbol{\chi}(\mathbf{X}, t). \quad (3.8)$$

We see that the velocity and acceleration of material particles are material fields. Also note that $\frac{\partial}{\partial t} \mathbf{u}(\mathbf{X}, t) = \frac{\partial}{\partial t} \boldsymbol{\chi}(\mathbf{X}, t)$. We will also require a spatial description of these fields. We denote by $\mathbf{v}^s(\mathbf{x}, t)$ the spatial description of the material solid velocity field, such that

$$\mathbf{v}^s(\mathbf{x}, t) = \left[\frac{\partial}{\partial t} \boldsymbol{\chi}(\mathbf{X}, t) \right]_{\mathbf{X}=\boldsymbol{\chi}^{-1}(\mathbf{x}, t)}. \quad (3.9)$$

Due to the definition of \mathbf{v}^s in (3.9) we also have (see section 4.4.4 in [42])

$$\mathbf{v}^s(\mathbf{x}, t)|_{\mathbf{x}=\chi(\mathbf{X}, t)} = \frac{\partial}{\partial t} \chi(\mathbf{X}, t). \quad (3.10)$$

To simplify notation we will follow [8] and write

$$\mathbf{v}^s(\mathbf{x}, t) = \frac{\partial}{\partial t} \chi(\mathbf{X}, t). \quad (3.11)$$

Similarly, for the spatial description of the solid acceleration, we have

$$\mathbf{a}^s(\mathbf{x}, t) = \left[\frac{\partial^2}{\partial t^2} \chi(\mathbf{X}, t) \right] \Big|_{\mathbf{X}=\chi^{-1}(\mathbf{x}, t)}. \quad (3.12)$$

Notice that $\mathbf{v}^s(\mathbf{x}, t)$ and $\mathbf{a}^s(\mathbf{x}, t)$ correspond to the velocity and acceleration of the solid material particle whose current coordinates are \mathbf{x} at time t . The acceleration of the fluid is given by (see section 3.1 in [15]),

$$\mathbf{a}^f = \frac{d^f \mathbf{v}^f}{dt} = \frac{\partial}{\partial t} \mathbf{v}^f + (\nabla \mathbf{v}^f) \mathbf{v}^f. \quad (3.13)$$

The **particle derivative of a field** $\mathcal{G}(\mathbf{x}, t)$ with respect to the particle α (s or f) is given by

$$\frac{d^\alpha}{dt} \mathcal{G} = \frac{\partial \mathcal{G}}{\partial t} + (\nabla \mathcal{G}) \mathbf{v}^\alpha, \quad (3.14)$$

where $\nabla(\cdot) = \frac{\partial(\cdot)}{\partial \mathbf{x}}$ denotes the partial derivative with respect to \mathbf{x} . Since nearly all our workings will be performed in the current configuration we will keep the shorthand notation ∇ to denote the spatial gradient in the current

configuration instead of explicitly writing $\nabla_{\boldsymbol{x}}$. The **particle derivative of a material volume** with respect to the α -constituent is given by (see section 1.3.1 in [28])

$$\frac{d^\alpha}{dt} \int_{\Omega_t} d\Omega_t = \int_{\Omega_t} \nabla \cdot \boldsymbol{v}^\alpha d\Omega_t. \quad (3.15)$$

The particle derivative also applies to a volume integral. Thus, for any quantity \mathcal{G} , associated with the α constituent, we have

$$\frac{d^\alpha}{dt} \int_{\Omega_t} \mathcal{G} d\Omega_t = \int_{\Omega_t} \left(\frac{d^\alpha \mathcal{G}}{dt} + \mathcal{G} \nabla \cdot \boldsymbol{v}^\alpha \right) d\Omega_t = \int_{\Omega_t} \left(\frac{\partial \mathcal{G}}{\partial t} + \nabla \cdot \mathcal{G} \boldsymbol{v}^\alpha \right) d\Omega_t. \quad (3.16)$$

This is commonly known as the Reynolds transport theorem. In the last step of (3.16) we have used the identity $\nabla \cdot (\psi \boldsymbol{s}) = \boldsymbol{s} \cdot \nabla \psi + \psi \nabla \cdot \boldsymbol{s}$ for some scalar ψ and vector \boldsymbol{s} .

3.2 Volume fractions

We restrict our attention to saturated porous media which are assumed to consist of solid and fluid parts. The fluid accounts for volume fractions $\phi_0(\boldsymbol{X}, t = 0)$ and $\phi(\boldsymbol{x}, t)$ of the total volume in the reference and the current and deformed configurations respectively, where ϕ is known as the porosity. The fractions for the solid are therefore $1 - \phi_0$ and $1 - \phi$ in the reference and the current configuration respectively. For a mixture the density in the

current configuration is given by

$$\rho := \rho^s(1 - \phi) + \rho^f\phi \quad \text{in } \Omega_t, \quad (3.17)$$

where ρ^s and ρ^f are the densities of the fluid and solid, respectively. We assume that both the solid and the fluid are incompressible so that $\rho^s = \rho_0^s$ and $\rho^f = \rho_0^f$. For notational convenience we also define

$$\hat{\rho}^s = \rho^s(1 - \phi), \quad (3.18)$$

and

$$\hat{\rho}^f = \rho^f\phi. \quad (3.19)$$

Due to mass conservation and the incompressibility of both the solid and the fluid phase we have

$$J = \frac{1 - \phi_0}{1 - \phi}, \quad (3.20)$$

where J represents the change in volume of the solid skeleton. The solid skeleton includes the solid (tissue in biological applications) and the voids occupied by the fluid. Note that although the solid is assumed to be incompressible the solid skeleton is able to change in volume, since fluid can enter or leave the solid skeleton.

3.3 Conservation of mass

When no mass change occurs, neither for the solid skeleton or the fluid contained in Ω_t , using the Reynolds transport theorem (3.16), the balance of mass, for a volume $V(t)$ that moves with the deforming poroelastic medium, can be expressed as

$$\frac{d^s}{dt} \int_{V(t)} (1 - \phi) \rho^s d\Omega_t = \int_{V(t)} \left(\frac{\partial(1 - \phi)\rho^s}{\partial t} + \nabla \cdot ((1 - \phi)\rho^s \mathbf{v}^s) \right) d\Omega_t,$$

$$\frac{d^f}{dt} \int_{V(t)} \phi \rho^f d\Omega_t = \int_{V(t)} \left(\frac{\partial \phi \rho^f}{\partial t} + \nabla \cdot (\phi \rho^f \mathbf{v}^f) \right) d\Omega_t.$$

Thus, the balance of mass for the solid is given by

$$\frac{\partial(1 - \phi)\rho^s}{\partial t} + \nabla \cdot ((1 - \phi)\rho^s \mathbf{v}^s) = 0 \quad \text{in } \Omega_t, \quad (3.21)$$

where \mathbf{v}^s is the velocity vector of the solid. Similarly, the balance of mass for the fluid is given by

$$\frac{\partial \phi \rho^f}{\partial t} + \nabla \cdot (\phi \rho^f \mathbf{v}^f) = \rho^f g \quad \text{in } \Omega_t, \quad (3.22)$$

where \mathbf{v}^f is the velocity vector of the fluid and g is a general source or sink term. Noting that ρ^s and ρ^f are constants (in space and time), these can be factored out of equations (3.21) and (3.22). Adding these two equations then provides the mass balance or continuity equation of the mixture (see section

8.3 in [15]),

$$\nabla \cdot ((1 - \phi)\mathbf{v}^s) + \nabla \cdot (\phi\mathbf{v}^f) = g \quad \text{in } \Omega_t. \quad (3.23)$$

3.4 Conservation of momentum

The balance law of linear momentum for each individual constituent is given by

$$\frac{d^\alpha}{dt} \int_{V(t)} \hat{\rho}^\alpha \mathbf{v}^\alpha d\Omega_t = \int_{V(t)} \nabla \cdot \boldsymbol{\sigma}^\alpha + \hat{\rho}^\alpha \mathbf{f} + \hat{\mathbf{p}}^\alpha + \Theta^\alpha \mathbf{v}^\alpha d\Omega_t. \quad (3.24)$$

Here $\boldsymbol{\sigma}^\alpha$ is the Cauchy stress tensor of the α constituent, \mathbf{f} is a volume force acting on the constituents, $\hat{\mathbf{p}}^\alpha$ are interaction forces representing frictional interactions between the solid and fluid, defined later in section 7.3.1, and $\Theta^\alpha \mathbf{v}^\alpha$ is the variation of momentum due to the α constituent source term [24]. Note that from (3.21) and (3.22) that we have $\Theta^s = 0$ and $\Theta^f = \rho^f g$. Using the first step of the Reynolds transport theorem (3.16), and the chain rule, we obtain

$$\nabla \cdot \boldsymbol{\sigma}^\alpha + \hat{\rho}^\alpha \mathbf{f} + \hat{\mathbf{p}}^\alpha + \Theta^\alpha \mathbf{v}^\alpha = \hat{\rho}^\alpha \mathbf{a}^\alpha + \mathbf{v}^\alpha \left(\frac{d^\alpha \hat{\rho}^\alpha}{dt} + \hat{\rho}^\alpha \nabla \cdot \mathbf{v}^\alpha \right) \quad \text{in } \Omega_t, \quad (3.25)$$

where \mathbf{a}^α are acceleration vectors of the constituents. Since each constituent exerts an equal and opposite interaction force on the other,

$$\hat{\mathbf{p}}^s + \hat{\mathbf{p}}^f = 0. \quad (3.26)$$

3.5 Constitutive relations

The interaction force is given by (see [28, eqn. (3.49)])

$$\hat{\mathbf{p}}^s = -\hat{\mathbf{p}}^f = -p\nabla\phi + \phi^2\mathbf{k}^{-1} \cdot (\mathbf{v}^f - \mathbf{v}^s), \quad (3.27)$$

where \mathbf{k} is the (dynamic) permeability tensor. The first term, $p\nabla\phi$, accounts for the pressure effect resulting from the variation of the section offered to the fluid flow, and the second term, $\phi^2\mathbf{k} \cdot (\mathbf{v}^f - \mathbf{v}^s)$, describes the viscous resistance opposed by the shear stress to the fluid flow from the drag at the internal walls of the porous network [28]. This particular choice for the interaction force means that the momentum balance for the fluid flow can later be reduced to the well known Darcy law.

The permeability tensor in the current configuration is given by

$$\mathbf{k} = J^{-1}\mathbf{F}\mathbf{k}_0(\chi)\mathbf{F}^T, \quad (3.28)$$

where $\mathbf{k}_0(\chi)$ is the permeability in the reference configuration, which may be chosen to be some (nonlinear) function dependent on the deformation. Examples of deformation dependent permeability tensors for biological tissues can be found in [47, 56, 57].

The solid stress tensor is given by the effective stress principle (see eqn. (8.62) in [15]),

$$\boldsymbol{\sigma}^s = \boldsymbol{\sigma}_e^s - (1 - \phi)\mathbf{I}p, \quad (3.29)$$

where $\boldsymbol{\sigma}_e^s$ is the effective stress tensor given by

$$\boldsymbol{\sigma}_e^s = \frac{1}{J} \mathbf{F} \cdot 2 \frac{\partial W(\boldsymbol{\chi})}{\partial \mathbf{C}} \cdot \mathbf{F}^T. \quad (3.30)$$

Here $W(\boldsymbol{\chi})$ denotes a strain-energy law (hyperelastic Helmholtz energy functional) dependent on the deformation of the solid. The fluid stress tensor can be written as (see [15, eqn. (8.63)])

$$\boldsymbol{\sigma}^f = \boldsymbol{\sigma}_{vis}^f - \phi \mathbf{I} p, \quad (3.31)$$

where $\boldsymbol{\sigma}_{vis}^f$ denotes the viscous stress tensor of the fluid, given by (see [15, eqn. (6.145)])

$$\boldsymbol{\sigma}_{vis}^f = \mu_f \phi (\nabla \mathbf{v}_f + (\nabla \mathbf{v}_f)^T - \frac{2}{3} \nabla \cdot \mathbf{v}_f), \quad (3.32)$$

where μ_f is the dynamic viscosity of the fluid.

Summing the conservation laws (3.25) for its constituents and applying the constitutive relations, the conservation of linear momentum for the mixture is

$$\begin{aligned} \hat{\rho}^s \mathbf{a}^s + \hat{\rho}^f \mathbf{a}^f + \mathbf{v}^s \left(\frac{d^s \hat{\rho}^s}{dt} + \hat{\rho}^s \nabla \cdot \mathbf{v}^s \right) + \mathbf{v}^f \left(\frac{d^f \hat{\rho}^f}{dt} + \hat{\rho}^f \nabla \cdot \mathbf{v}^f \right) \\ = \nabla \cdot (\boldsymbol{\sigma}_e + \boldsymbol{\sigma}_{vis} - p \mathbf{I}) + \rho \mathbf{f} + g \mathbf{v}^f \quad \text{in } \Omega_t. \end{aligned} \quad (3.33)$$

Applying (3.21) and (3.22), along with applications of (3.14), we get

$$\hat{\rho}^s \mathbf{a}^s + \hat{\rho}^f \mathbf{a}^f = \nabla \cdot (\boldsymbol{\sigma}_e + \boldsymbol{\sigma}_{vis} - p\mathbf{I}) + \rho \mathbf{f} \quad \text{in } \Omega_t. \quad (3.34)$$

The momentum equation for the fluid flow can be identified from (3.25) with $\alpha = f$ as

$$\hat{\rho}^f \mathbf{a}^f = \nabla \cdot (\boldsymbol{\sigma}_{vis}^f - \phi p \mathbf{I}) + \hat{\rho}^f \mathbf{f} + p \nabla \phi - \phi^2 \mathbf{k}^{-1} (\mathbf{v}^f - \mathbf{v}^s) \quad \text{in } \Omega_t. \quad (3.35)$$

3.6 Summary of the general poroelasticity model

We consider Ω_t to be a bounded domain in \mathbb{R}^2 or \mathbb{R}^3 , and for the purpose of defining boundary conditions, $\partial\Omega_t = \Gamma_D \cup \Gamma_N$ for displacement and stress boundary conditions and $\partial\Omega_t = \Gamma_P \cup \Gamma_F$ for pressure and flux boundary conditions, with outward pointing unit normal \mathbf{n} . The strong problem for the full mixture theory model is to find $\chi(\mathbf{X}, t)$, $\mathbf{v}^f(\mathbf{x}, t)$ and $p(\mathbf{x}, t)$ such that

$$\hat{\rho}^s \mathbf{a}^s + \hat{\rho}^f \mathbf{a}^f = \nabla \cdot (\boldsymbol{\sigma}_e + \boldsymbol{\sigma}_{vis} - p\mathbf{I}) + \rho \mathbf{f} \quad \text{in } \Omega_t, \quad (3.36a)$$

$$\hat{\rho}^f \mathbf{a}^f = \nabla \cdot (\boldsymbol{\sigma}_{vis}^f - \phi p \mathbf{I}) + p \nabla \phi - \phi \mathbf{k}^{-1} (\mathbf{v}^f - \mathbf{v}^s) + \hat{\rho}^f \mathbf{f} \quad \text{in } \Omega_t, \quad (3.36b)$$

$$\nabla \cdot ((1 - \phi) \mathbf{v}^s) + \nabla \cdot (\phi \mathbf{v}^f) = g \quad \text{in } \Omega_t, \quad (3.36c)$$

$$\chi = \mathbf{X} + \mathbf{u}_D \quad \text{on } \Gamma_D, \quad (3.36d)$$

$$(\boldsymbol{\sigma}_e + \boldsymbol{\sigma}_{vis} - p\mathbf{I})\mathbf{n} = \mathbf{t}_N \quad \text{on } \Gamma_N, \quad (3.36e)$$

$$\mathbf{v}^f = \mathbf{v}_D^f \quad \text{on } \Gamma_F, \quad (3.36f)$$

$$(\boldsymbol{\sigma}_{vis} - \phi p\mathbf{I})\mathbf{n} = \mathbf{s}_P \quad \text{on } \Gamma_P, \quad (3.36g)$$

$$\boldsymbol{\chi}(0) = \mathbf{X} + \mathbf{u}^0, \quad \mathbf{v}^s(0) = \mathbf{v}^{s0}, \quad \mathbf{v}^f(0) = \mathbf{v}^{f0} \quad \text{in } \Omega_0. \quad (3.36h)$$

We have also summarized all the variables and corresponding equations in Table 3.1.

Unknown	Notation	Equation
Primary variables		Primary equations (general model)
Motion of the solid	χ	$\hat{\rho}^s \mathbf{a}^s + \hat{\rho}^f \mathbf{a}^f = \nabla \cdot (\boldsymbol{\sigma}_e + \boldsymbol{\sigma}_{vis} - p \mathbf{I}) + \rho \mathbf{f}$ (3.34)
Fluid velocity	\mathbf{v}^f	$\hat{\rho}^f \mathbf{a}^f = \nabla \cdot (\boldsymbol{\sigma}_{vis}^f - \phi p \mathbf{I}) + p \nabla \phi - \phi \mathbf{k}^{-1}(\mathbf{v}^f - \mathbf{v}^s) + \hat{\rho}^f \mathbf{f}$ (3.35)
Pressure of the fluid	p	$\nabla \cdot ((1 - \phi) \mathbf{v}^s) + \nabla \cdot (\phi \mathbf{v}^f) = g$ (3.23)
Secondary variables		Secondary equations
Deformation gradient tensor	\mathbf{F}	$\mathbf{F} = \frac{\partial}{\partial \mathbf{X}} \chi(\mathbf{X}, t)$ (3.2)
Right Cauchy-Green tensor	\mathbf{C}	$\mathbf{C} = \mathbf{F}^T \mathbf{F}$ (3.3)
Jacobian	J	$J = \det(\mathbf{F})$ (3.4)
Velocity of the solid	\mathbf{v}^s	$\mathbf{v}^s(\mathbf{x}, t) _{\mathbf{x}=\chi(\mathbf{X}, t)} = \frac{\partial}{\partial t} \chi(\mathbf{X}, t)$ (3.10)
Acceleration of the solid	\mathbf{a}^s	$\mathbf{a}^s(\mathbf{x}, t) _{\mathbf{x}=\chi(\mathbf{X}, t)} = \frac{\partial^2}{\partial t^2} \chi(\mathbf{X}, t)$ (???)
Acceleration of the fluid	\mathbf{a}^f	$\mathbf{a}^f = \frac{\partial}{\partial t} \mathbf{v}^f + (\nabla \mathbf{v}^f) \mathbf{v}^f$ (3.13)
Porosity	ϕ	$\phi = 1 - \frac{1 - \phi_0}{J}$ (3.20)
Mixture density	ρ	$\rho = \rho^s(1 - \phi) + \rho^f \phi$ (3.17)
Eulerian solid density	$\hat{\rho}_s$	$\hat{\rho}^s = \rho^s(1 - \phi)$ (3.18)
Eulerian fluid density	$\hat{\rho}_f$	$\hat{\rho}^f = \rho^f \phi$ (3.19)
Constitutive variables		Constitutive equations
Solid elastic stress tensor	$\boldsymbol{\sigma}_e$	$\boldsymbol{\sigma}_e^s = \frac{1}{J} \mathbf{F} \cdot 2 \frac{\partial W(\chi)}{\partial \mathbf{C}} \cdot \mathbf{F}^T$ (3.30)
Fluid viscous stress tensor	$\boldsymbol{\sigma}_{vis}$	$\boldsymbol{\sigma}_{vis}^f = \mu_f \phi (\nabla \mathbf{v}_f + (\nabla \mathbf{v}_f)^T - \frac{2}{3} \nabla \cdot \mathbf{v}_f)$ (3.31)
Permeability tensor	\mathbf{k}	$\mathbf{k} = J^{-1} \mathbf{F} \mathbf{k}_0(\chi) \mathbf{F}^T$ (3.28)

Table 3.1: Recapitulating the unknowns and equations of the general poroelasticity model.

3.7 Simplification and reformulation of the model

To arrive at the quasi-static, fully saturated, incompressible three-field large deformation poroelasticity model, we will now ignore inertia forces (left hand side of (3.34) and (3.35)), and ignore the viscous shear stress in the fluid ($\boldsymbol{\sigma}_{vis}^f$ in (3.35)). Justifications for making these modelling assumptions with respect to the proposed lung model will be given in section 7.2. After making these assumptions, and rewriting the equations in terms of the fluid flux, given by

$$\mathbf{z} = \phi(\mathbf{v}^f - \mathbf{v}^s), \quad (3.37)$$

the resulting problem is to find $\chi(\mathbf{X}, t)$, $\mathbf{z}(\mathbf{x}, t)$ and $p(\mathbf{x}, t)$ such that

$$-\nabla \cdot (\boldsymbol{\sigma}_e - p\mathbf{I}) = \rho\mathbf{f} \quad \text{in } \Omega_t, \quad (3.38a)$$

$$\mathbf{k}^{-1}\mathbf{z} + \nabla p = \rho^f\mathbf{f} \quad \text{in } \Omega_t, \quad (3.38b)$$

$$\nabla \cdot (\mathbf{v}^s + \mathbf{z}) = g \quad \text{in } \Omega_t, \quad (3.38c)$$

$$\chi = \mathbf{X} + \mathbf{u}_D \quad \text{on } \Gamma_D, \quad (3.38d)$$

$$(\boldsymbol{\sigma}_e - p\mathbf{I})\mathbf{n} = \mathbf{t}_N \quad \text{on } \Gamma_N, \quad (3.38e)$$

$$\mathbf{z} \cdot \mathbf{n} = q_D \quad \text{on } \Gamma_F, \quad (3.38f)$$

$$p = p_D \quad \text{on } \Gamma_P, \quad (3.38g)$$

$$\chi(0) = \mathbf{X} + \mathbf{u}^0, \quad \text{in } \Omega_0. \quad (3.38h)$$

This is the large deformation model we will consider from here onwards.

3.8 Linear poroelasticity

To allow us to perform rigorous analysis of the proposed finite element scheme presented in Chapter 5, we will now assume small deformations to yield a linear model of poroelasticity. This model is often referred to as the ‘Biot model’ in the geomechanics community and contains some additional terms. We will introduce the full Biot model here for use with a 2D cantilever bracket problem later tested in section 5.8.3, and to highlight that any subsequent theory developed in later chapters can be extended to the full Biot model. The governing equations of the Biot model, with displacement \mathbf{u} , fluid flux \mathbf{z} , and pressure p as primary variables are summarized below:

$$-\nabla \cdot \boldsymbol{\sigma} = \mathbf{f} \quad \text{in } \Omega \times (0, T), \quad (3.39a)$$

$$\mathbf{k}^{-1} \mathbf{z} + \nabla p = \mathbf{b} \quad \text{in } \Omega \times (0, T), \quad (3.39b)$$

$$\nabla \cdot \mathbf{z} + \frac{\partial}{\partial t}(\alpha \nabla \cdot \mathbf{u} + c_0 p) = g \quad \text{in } \Omega \times (0, T), \quad (3.39c)$$

$$\mathbf{u} = \mathbf{u}_D \quad \text{on } \Gamma_D \times (0, T), \quad (3.39d)$$

$$\boldsymbol{\sigma} \mathbf{n} = \mathbf{t}_N \quad \text{on } \Gamma_N \times (0, T), \quad (3.39e)$$

$$p = p_D \quad \text{on } \Gamma_P \times (0, T), \quad (3.39f)$$

$$\mathbf{z} \cdot \mathbf{n} = q_D \quad \text{on } \Gamma_F \times (0, T), \quad (3.39g)$$

$$\mathbf{u}(0, \cdot) = \mathbf{u}^0, \quad p(0) = p^0, \quad \text{in } \Omega. \quad (3.39h)$$

Here $\boldsymbol{\sigma}$ is the total stress tensor given by $\boldsymbol{\sigma} = \lambda \text{tr}(\boldsymbol{\epsilon}(\mathbf{u}))\mathbf{I} + 2\mu_s \boldsymbol{\epsilon}(\mathbf{u}) - \alpha p \mathbf{I}$, with the linear strain tensor defined as $\boldsymbol{\epsilon}(\mathbf{u}) = \frac{1}{2} (\nabla \mathbf{u} + (\nabla \mathbf{u})^T)$, g is the fluid source term, \mathbf{f} is the body force on the mixture, and \mathbf{b} is the body force on the fluid. Here Ω is a bounded domain in \mathbb{R}^2 or \mathbb{R}^3 , and for the purpose of defining boundary conditions, $\partial\Omega = \Gamma_D + \Gamma_N$ for displacement and stress boundary conditions and $\partial\Omega = \Gamma_P + \Gamma_F$ for pressure and flux boundary conditions, with outward pointing unit normal \mathbf{n} . The parameters along with a description are given in Table 6.3.

Parameter	
Lamé's first parameter	λ ,
Lamé's second parameter (shear modulus)	μ_s ,
Dynamic permeability tensor	\mathbf{k} ,
Biot-Willis constant	α ,
Constrained specific storage coefficient	c_0 .

Table 3.2: Poroelasticity parameters.

A derivation and more detailed explanation of these equations can be found in [79] and [86]. In this work we will mainly consider a simplification of the full Biot model (3.39), by setting $\alpha = 1$ and $c_0 = 0$. This yields a fully incompressible poroelastic model that retains all the numerical difficulties associated with approximating the original system of equations (3.39), see Remark 1. The linear fully saturated and incompressible poroelastic model

is given by:

$$-(\lambda + \mu_s) \nabla(\nabla \cdot \mathbf{u}) - \mu_s \nabla^2 \mathbf{u} + \nabla p = \mathbf{f} \quad \text{in } \Omega \times (0, T), \quad (3.40a)$$

$$\mathbf{k}^{-1} \mathbf{z} + \nabla p = \mathbf{b} \quad \text{in } \Omega \times (0, T), \quad (3.40b)$$

$$\nabla \cdot (\mathbf{u}_t + \mathbf{z}) = g \quad \text{in } \Omega \times (0, T), \quad (3.40c)$$

$$\mathbf{u} = \mathbf{u}_D \quad \text{on } \Gamma_D \times (0, T), \quad (3.40d)$$

$$\boldsymbol{\sigma} \mathbf{n} = \mathbf{t}_N \quad \text{on } \Gamma_N \times (0, T), \quad (3.40e)$$

$$p = p_D \quad \text{on } \Gamma_P \times (0, T), \quad (3.40f)$$

$$\mathbf{z} \cdot \mathbf{n} = q_D \quad \text{on } \Gamma_F \times (0, T), \quad (3.40g)$$

$$\mathbf{u}(0, \cdot) = \mathbf{u}^0 \quad \text{in } \Omega. \quad (3.40h)$$

This model is the small deformation version of the simplified and reformulated large deformation poroelasticity model (3.38), and will be the small deformation model considered from here onwards.

Remark 1. *The extension of the theoretical results presented in Chapter 5 from (3.40) to the full Biot equations (3.39), with $\alpha \in \mathbb{R}_{>0}$ and $c_0 \in \mathbb{R}_{>0}$ is straightforward. In the analysis in Chapter 5, the constant α would just get absorbed by a general constant C . When $c_0 > 0$, an additional pressure term is introduced into the mass conservation equation. Since this term is coercive, it only improves the stability of the system.*

Chapter 4

Finite element method

4.1 Introduction

A large proportion of the mathematical models in science and engineering take the form of differential equations. Only in the simplest cases, or under strong assumptions, is it possible to find exact analytical solutions to the equations in the model. Numerical methods are an established means of solving differential equations that are of practical interest in a variety of applied problems. Finite difference, finite volume and finite element methods are the most widely used types of such methods. Their basic idea is replacing the infinite-dimensional problem by a finite-dimensional approximation, which is, generally speaking, easier to compute. Finite element methods are based on weakening the restrictions on the solution space in the continuous setting, and searching for the approximate solution in the subspace which spans ba-

sis functions supported on small regions inside the domain. These methods are well-suited to solving problems on complex domains, and are therefore widely used in practical applications. In this work we consider only finite element methods (FEMs) for solving partial differential equations. This chapter comprises an overview of several theoretical and practical aspects of classical FEMs. The theory and notation presented here are essential in developing the techniques that form the core of this thesis. Most of the work presented in this chapter is based on work already presented in [6, 7, 13, 19, 20].

4.2 Norms and spaces

Let Ω be a bounded domain in \mathbb{R}^2 or \mathbb{R}^3 , and $\partial\Omega$ be the associated boundary. The space of square integrable functions is then given by

$$L^2(\Omega) = \left\{ u : \int_{\Omega} |u(x)|^2 dx < \infty \right\},$$

with norm

$$\|u\|_{0,\Omega} = \left\{ \int_{\Omega} |u(x)|^2 dx \right\}^{1/2}.$$

This space is equipped with the inner product

$$(u, v) := \int_{\Omega} u(x)v(x)dx,$$

such that $\|u\|_{0,\Omega} = (u, v)^{1/2}$. Throughout this thesis we shall frequently refer to the Sobolev spaces $H^1(\Omega)$ and $H^2(\Omega)$. The definitions of these are as follows:

$$H^1(\Omega) = \left\{ u \in L^2(\Omega) : \frac{\partial u}{\partial x_j} \in L_2(\Omega), j = 1, \dots, n, \right\},$$

$$H^2(\Omega) = \left\{ u \in L^2(\Omega) : \frac{\partial u}{\partial x_j} \in L_2(\Omega), j = 1, \dots, n, \frac{\partial^2 u}{\partial x_i \partial x_j} \in L_2(\Omega), i, j = 1, \dots, n \right\}.$$

The corresponding norms are defined as

$$\|u\|_{1,\Omega} = \left\{ \|u\|_{0,\Omega}^2 + \sum_{j=1}^n \left\| \frac{\partial u}{\partial x_j} \right\|_{0,\Omega}^2 \right\}^{1/2},$$

$$\|u\|_{2,\Omega} = \left\{ \|u\|_{0,\Omega}^2 + \sum_{j=1}^n \left\| \frac{\partial u}{\partial x_j} \right\|_{0,\Omega}^2 + \sum_{i,j=1}^n \left\| \frac{\partial^2 u}{\partial x_i \partial x_j} \right\|_{0,\Omega}^2 \right\}^{1/2}.$$

We also define the divergence space

$$H_{div}(\Omega) = \left\{ \mathbf{v} \in L^2(\Omega) : \nabla \cdot \mathbf{v} \in L^2(\Omega) \right\}.$$

The set of functions of $L^2(\partial\Omega)$ which are traces of functions of $H^1(\Omega)$ onto the boundary, constitutes a subspace of $L^2(\partial\Omega)$ denoted by $H^{1/2}(\partial\Omega)$. We will also briefly use linear and bounded functionals (dual spaces) of H^1 , $H^{1/2}$ and H_{div} , which will be denoted by H^{-1} , $H^{-1/2}$ and H_{div}^{-1} , respectively.

We define the following norms for continuous in time functions u such

that the norm $L^2(0, T; X)$ satisfies

$$\|u\|_{L^2(X)} = \left(\int_0^T \|u(s, \cdot)\|_X^2 ds \right)^{1/2},$$

and the norm $L^\infty(0, T; X)$ satisfies

$$\|u\|_{L^\infty(X)} = \sup \{ \|u(s, \cdot)\|_X : s \in [0, T] \},$$

where X is any given function space over Ω . We partition $[0, T]$ into N evenly spaced non-overlapping regions $(t_{n-1}, t_n]$, $n = 1, 2, \dots, N$. For any sufficiently smooth function $u(t, x)$ we define $u^n(x) = u(t_n, x)$. Let the discrete approximation for all time to be the piecewise constant in time functions $v(t, x) := v^n(x)$ for $t \in (t_{n-1}, t_n]$. For such piecewise constant in time functions, v , we define the norms

$$\|v\|_{L^2(X)} = \left(\sum_{n=1}^N \Delta t \|v^n\|_X^2 \right)^{1/2},$$

and

$$\|v\|_{L^\infty(X)} = \max \{ \|v^n\|_X, n = 1, 2, \dots, N \}.$$

4.3 Model problem

It is instructive to begin at a simple level and proceed by incrementally adding to the complexity of the equations we are discretising when explaining the

use of the FEM, so we begin by considering the classical heat equation: given $T > 0$, for $t \in [0, T]$ find $u(t, x)$ such that

$$\frac{\partial u}{\partial t} - \nabla \cdot \nabla u = 0 \quad \text{in } \Omega_t, \quad (4.1a)$$

$$\mathbf{n} \cdot \nabla u = g_N \quad \text{on } \Gamma_N, \quad (4.1b)$$

$$u = g_D \quad \text{on } \Gamma_D, \quad (4.1c)$$

$$u(0, x) = u^0(x) \quad \text{in } \Omega. \quad (4.1d)$$

Here Ω is a bounded domain in \mathbb{R}^2 or \mathbb{R}^3 , with boundary $\partial\Omega = \Gamma_N \cup \Gamma_D$, that has an outward pointing unit normal \mathbf{n} . The initial condition is given by $u^0(x)$. In the case where $g_N = 0$, system (4.1) can describe the evolution of heat in an object with geometry described by Ω , where we have perfect thermal insulation on Γ_N and fixed temperature distributions given by the function g_D defined on the boundary due to some part of the environment with fixed temperature contacting the object along Γ_D .

4.3.1 Weak formulation

The strong form of (4.1) requires u to be at least twice differentiable. To weaken the regularity restrictions we multiply equation (4.1a) by an arbitrary function v , called a test function, and integrate over Ω :

$$\left(\frac{\partial u}{\partial t}, v \right) - (\nabla \cdot \nabla u, v) = 0.$$

Applying the divergence theorem, this equation can be rewritten:

$$\begin{aligned} \left(\frac{\partial u}{\partial t}, v \right) - (\nabla u \cdot \mathbf{n}, v)_{\partial\Omega} + (\nabla u, \nabla v) \\ = \left(\frac{\partial u}{\partial t}, v \right) - (\nabla u \cdot \mathbf{n}, v)_{\Gamma_D} - (g_N, v)_{\Gamma_N} + (\nabla u, \nabla v) = 0. \end{aligned}$$

Here $(\cdot, \cdot)_{\Gamma_N}$ and $(\cdot, \cdot)_{\Gamma_D}$ denote the inner product taken over Γ_N and Γ_D , respectively. Taking note of the Dirichlet condition (4.1c), and letting $v = 0$ on Γ_D , we arrive at the following equation:

$$\left(\frac{\partial u}{\partial t}, v \right) + (\nabla u, \nabla v) = (g_N, v)_{\Gamma_N}.$$

Note that in this equation the second derivatives of u need not exist. With that in mind, both the solution and the test functions can come from the space $H^1(\Omega)$, as long as they satisfy the appropriate Dirichlet boundary conditions. For convenience we will use the notation $X_D = \{v \in H^1(\Omega) | v = u_D \text{ on } \Gamma_D\}$ and $X_0 = \{v \in H^1(\Omega) | v = 0 \text{ on } \Gamma_D\}$. The weak formulation of (4.1a) is as follows: Find $u \in X_D$ such that

$$\left(\frac{\partial u}{\partial t}, v \right) + (\nabla u, \nabla v) = (g_N, v)_{\Gamma_N} \quad \forall v \in X_0. \quad (4.2)$$

4.3.2 Time discretisation

We also need to choose a method of treating the time derivative. In this work, we do so using Euler difference quotients, and so we make the approximation

$u_t(t + \Delta t, x) \approx \frac{u(t + \Delta t, x) - u(t, x)}{\Delta t}$ for some constant time step Δt . We write $u(x)^n$ for the temporally-semidiscrete approximation to $u(n\Delta t, x)$, and our numerical scheme will yield approximations at times $t = 0, \Delta t, 2\Delta t, \dots, T$. Inserting this difference quotient and assuming that ΔT divides T , equation (4.3) becomes: for $n = 1, 2, \dots, \frac{T}{\Delta t}$, find $u^n \in X_D$ such that

$$(u^n, v) + \Delta t (\nabla u^n, \nabla v) = (g_N, v)_{\Gamma N} + (u^{n-1}, v) \quad \forall v \in X_0. \quad (4.3)$$

4.3.3 Finite element discretisation

In order to solve this problem numerically, we must make it finite dimensional by discretising it suitably. The finite element approximation space is constructed as follows: first, the problem domain is partitioned into small element domains, and second, the element is defined by prescribing for each element domain a set of nodes and nodal values, and defining suitable basis functions on these, for example, as piecewise-linear basis functions.

Element domains are normally shaped as triangles or squares in \mathbb{R}^2 , tetrahedra or hexahedra in \mathbb{R}^3 . All the nodes, edges and faces of element domains constitute the problem mesh. Defining local basis functions completes the finite element space. For a rigorous definition of finite elements, and a description of different types of elements we refer to [19].

Let \mathcal{T}^h be a partition of Ω into non-overlapping elements K . We denote by h the size of the largest element in \mathcal{T}^h . On the given partition \mathcal{T}^h we

then define the following finite element spaces, to solve the model problem:

$$X_{hD} = \{u \in C^0(\Omega) : u|_K \in P_1(K); u = u_D \text{ on } \Gamma_D; \forall K \in \mathcal{T}^h\},$$

$$X_{h0} = \{u \in C^0(\Omega) : u|_K \in P_1(K); u = 0 \text{ on } \Gamma_D; \forall K \in \mathcal{T}^h\},$$

where $P_1(K)$ is the space of linear polynomials on K , and $C^0(\Omega)$ is the space of continuous functions on Ω . The discretised problem, for each time step, is to find $u_h^n \in X_{hD}$ such that

$$(u_h^n, v_h) + \Delta t (\nabla u_h^n, \nabla v_h) = (g_N, v_h)_{\Gamma N} + (u_h^{n-1}, v_h) \quad \forall v_h \in X_{h0}. \quad (4.4)$$

We now choose the Lagrangian basis $\{\phi_1, \phi_2, \dots, \phi_m\}$ of X^h defined by the nodal values at the nodes $\{\mathbf{x}_1, \mathbf{x}_2, \dots, \mathbf{x}_m\}$, namely

$$\phi_i(\mathbf{x}_j) = \delta_{i,j} = \begin{cases} 1, & i = j \\ 0, & i \neq j \end{cases},$$

We observe that a basis of X_{h0} can be constructed by removing ϕ_i with $\mathbf{x}_i \in \Gamma_D$ from the basis of X_h . Let us assume that the indices of such basis functions are $1, \dots, m$, and therefore $X_{h0} = \text{span}\{\phi_1, \dots, \phi_m\}$. The finite-dimensional weak problem (4.4) is equivalent to: Find $u_h^n \in X_{hD}$ such that

$$(u_h^n, \phi_i) + \Delta t (\nabla u_h^n, \nabla \phi_i) = (g_N, \phi_i)_{\Gamma N} + (u_h^{n-1}, \phi_i) \quad \forall i = 1, \dots, m. \quad (4.5)$$

Any function from X_h can be presented in the form of a basis expansion. Let this basis expansion for u_h be

$$u_h^n = \sum_{i=1}^m u_i^n \phi_i,$$

with $u_i^n = u_h^n(\mathbf{x}_i)$. We define the vector of nodal values to be $\mathbf{u}^n = [u_1^n, \dots, u_m^n]^T$. Substituting this expression into (4.5), we finally obtain a linear system which we can solve for \mathbf{u}^n :

$$(\mathbf{M} + \Delta t \mathbf{A}) \mathbf{u}^n = \mathbf{M} \mathbf{u}^{n-1} + \mathbf{g}, \quad (4.6)$$

where we have defined the following matrices and vectors:

$$\mathbf{A} = [\mathbf{a}_{ij}], \quad \mathbf{a}_{ij} = \int_{\Omega} \nabla \phi_i \cdot \nabla \phi_j \, dx,$$

$$\mathbf{M} = [\mathbf{m}_{ij}], \quad \mathbf{m}_{ij} = \int_{\Omega} \phi_i \cdot \phi_j \, dx,$$

$$\mathbf{g} = [\mathbf{g}_i], \quad \mathbf{g}_i = \int_{\Gamma_N} g_N \cdot \phi_i \, ds,$$

The linear system of equations (4.6) can be solved using standard methods such as Gaussian elimination.

4.4 Mixed methods

Before considering the discretisation of the poroelasticity equations in Chapter 5 we first consider the problems of Darcy and Stokes flow. This is because many of the difficulties in solving the three-field poroelasticity problem are present when coupling the Stokes equations (elasticity of the porous mixture) with the Darcy equations (fluid flow through pores), with a modified incompressibility constraint that combines the divergence of the displacement velocity and the fluid flux. We begin with a general formulation of both the Darcy and Stokes flow equations:

$$\mathbf{A}(\mathbf{u}) + \nabla p = \mathbf{f} \quad \text{in } \Omega_t, \tag{4.7a}$$

$$\nabla \cdot \mathbf{u} = 0 \quad \text{in } \Omega_t, \tag{4.7b}$$

where \mathbf{u} denotes the velocity vector, p the pressure, $\mathbf{f} \in [L^2(\Omega)]^d$, with $d = 2, 3$, and \mathbf{A} represents the two cases:

- $\mathbf{A}(\mathbf{u}) := \mathbf{k}^{-1}\mathbf{u}$, corresponding to Darcy's equation.
- $\mathbf{A}(\mathbf{u}) := -2\mu_f \nabla \cdot \boldsymbol{\epsilon}(\mathbf{u})$, corresponding to Stokes equation.

For simplicity we assume Dirichlet conditions on the boundary, that is, $\mathbf{u} = 0$ on Γ_D for Stokes and $\mathbf{u} \cdot \mathbf{n} = 0$ on Γ_N for Darcy. Mixed methods refer to the discretisation of different variables using different finite elements. In order to formulate our finite element method we first need the weak formulation of

problem (4.7). To do this we introduce the spaces

$$W^D = \{\mathbf{v} \in H_{div}(\Omega) : \mathbf{v} \cdot \mathbf{n} = 0 \text{ on } \partial\Omega\},$$

$$W^S = \{\mathbf{v} \in [H_1(\Omega)]^d : \mathbf{v} = 0 \text{ on } \Gamma_D\},$$

and

$$L_0^2 = \left\{ q \in L_2(\Omega) : \int_{\Gamma} q \, dx = 0 \right\}.$$

We denote the product space $\mathcal{W}^X := W^X \times L_0^2$, where X is chosen to be D for the Darcy equations or S for the Stokes equations. We also define the following norm on \mathcal{W}^X :

$$\|(\mathbf{u}, p)\|_{\mathcal{W}^X}^2 = \|\mathbf{u}\|_{l,\Omega}^2 + \|\nabla \cdot \mathbf{u}\|_{0,\Omega}^2 + \|p\|_{0,\Omega}^2,$$

with $l = 0$ for Darcy and $l = 1$ for Stokes. Let $a(\mathbf{u}, \mathbf{v})$ be the bilinear form corresponding to the weak formulation of $A(\mathbf{u})$

$$a(\mathbf{u}, \mathbf{v}) = \begin{cases} (\mathbf{k}^{-1}\mathbf{u}, \mathbf{v}) \, dx & \text{if Darcy's equation} \\ \int_{\Omega} 2\mu(\epsilon(\mathbf{u}) : \epsilon(\mathbf{v})) + \lambda(\nabla \cdot \mathbf{u})(\nabla \cdot \mathbf{v}) \, dx & \text{if Stokes equation} \end{cases}.$$

Now consider the combined bilinear form

$$B[(\mathbf{u}, p), (\mathbf{v}, q)] = a(\mathbf{u}, \mathbf{v}) - (p, \nabla \cdot \mathbf{v}) + (q, \nabla \cdot \mathbf{u}).$$

The continuous weak formulation of (4.7) is now to find $(\mathbf{u}, p) \in \mathcal{W}^X$ such that

$$B[(\mathbf{u}, p), (\mathbf{v}, q)] = (\mathbf{f}, \mathbf{v}) \quad \forall (\mathbf{v}, q) \in \mathcal{W}^X.$$

For a given finite element subspace $\mathcal{W}_h^X \in \mathcal{W}^X$, we are left with the finite dimensional problem: find $(\mathbf{u}_h, p_h) \in \mathcal{W}_h^X$ such that:

$$B[(\mathbf{u}_h, p_h), (\mathbf{v}_h, q_h)] = (\mathbf{f}, \mathbf{v}_h) \quad \forall (\mathbf{v}_h, q_h) \in \mathcal{W}_h^X.$$

To ensure stability and convergence of the discretisation, the discrete subspace (mixed element) has to be chosen such that the following discrete inf-sup condition, [9], is fulfilled:

$$\gamma \|(\mathbf{u}_h, p_h)\|_{\mathcal{W}_h^X} \leq \sup_{(\mathbf{v}_h, q_h) \in \mathcal{W}_h^X} \frac{B_h[(\mathbf{u}_h, p_h), (\mathbf{v}_h, q_h)]}{\|(\mathbf{v}, q)\|_{\mathcal{W}_h^X}} \quad \forall (\mathbf{u}, p) \in \mathcal{W}_h^X, \quad (4.8)$$

where $\gamma > 0$ is a constant independent of any mesh parameters. Establishing this condition ensures wellposedness of the discretization so that the linear system arising from the fully discrete method is non-singular and can be solved using standard methods. It is not trivial to prove (4.8) for different combinations of finite element. This task has resulted in its own research field within Numerical Analysis, and countless papers have been published on this topic. In table 4.1 we have documented some popular standard finite element pairs for solving the Stokes and Darcy equations, and outlined whether these satisfy (4.8), thereby yielding a stable and optimally converging method, or

not. Note that many other possible discretisations exist.

Mixed element	Stokes	Darcy
$P1 - P1$	✗	✗
$P2 - P1$	✓	✗
$P1 - P1 + stab$	✓	✓
$P1 - P0$	✗	✗
$RT - P0$	✗	✓
$P1 - P0 + stab$	✓	✓

Table 4.1: Possible finite element combinations for Stokes and Darcy flow, showing whether a particular choice of elements is stable and optimally converging or not.

The naive choice of piecewise linear finite elements for both the velocities and the pressure, denoted by $(P1 - P1)$, or piecewise linear finite elements for the velocities and piecewise constants for the pressure, $(P1 - P0)$, result in an ill posed discretization [22]. Intuitively, this is because the velocity space is not rich enough to constrain the pressures, thus resulting in spurious pressure oscillations. A detailed explanation of this along with some worked examples can be found in [33]. The Taylor-Hood element, $(P2 - P1)$ - piecewise quadratic for the velocities and piecewise linear for the pressure, is a commonly used element for the Stokes equations. However for the Darcy equations this element does not converge at the right order and fails to converge for the divergence of the velocities [22]. The Raviart-Thomas element, $(RT - P0)$, first proposed in [83] is a divergence free element, often used to solve the Darcy equations. However this element is not able to control H^1 velocities, and therefore can not be used to solve the Stokes equations.

When the finite element discretisation is based on a discrete subspace that does not satisfy the discrete inf-sup condition (4.8), a procedure aiming at stabilizing the discrete system may be accomplished. The philosophy of stabilized methods is to strengthen formulations by adding an extra term, often to the mass conservation equation, so that discrete approximations, which would otherwise be unstable, become stable and convergent [71]. Numerous stabilization techniques exist. To stabilize the equal order piecewise linear pair, a polynomial pressure projection has been proposed that results in a stable element for both the Stokes and Darcy equations, ($P1 - P1 + stab$), [14]. Also, a pressure jump stabilization, ($P1 - P0 + stab$), that uses a piecewise constant pressure approximation and is stable and optimally converging for both the Stokes and Darcy equation has been analysed in [22]. This is the stabilization we will modify to solve the poroelasticity equations.

Chapter 5

Stabilized low-order finite element approximation for linear three-field poroelasticity

5.1 Introduction

In this chapter we develop a stabilized, low-order, mixed finite element method for poroelastic models of biological tissues and restrict our attention to the fully saturated, incompressible, small deformation case. Our mixed scheme uses the lowest possible approximation order: piecewise constant approximation for the pressure and piecewise linear continuous elements for the displacement and fluid flux.

To ensure stability, a mixed finite element method must satisfy the

Ladyzhenskaya-Babuska-Brezzi (LBB) condition. In this work we use a local pressure jump stabilization method pioneered by [22] for the study of Stokes and Darcy flows that are coupled via an interface. This approach provides the natural H^1 stability for the displacements and $H\text{div}$ stability for the fluid flux. The naive approach of using the stabilization of the pressure, as is done for the Darcy and Stokes equations in [22], results in an approximation that does not converge at an optimal rate. Stabilization using the time derivative of pressure in the stabilization term is shown to be crucial for stability and optimal convergence with refinement and counterexamples are provided in Section 6.5.

In section 5.2 we formulate the model and its continuous weak formulation and construct a fully-discrete approximation. We prove existence and uniqueness of solutions to this discrete model at each time step in section 5.4, provide an energy estimate over time in section 5.5, and derive an optimal order a-priori error estimate in section 5.6. Finally in section 6.5, we present numerical experiments to illustrate the convergence of the method and its ability to overcome pressure oscillations.

5.2 The poroelastic model

5.2.1 Governing equations

Following [79] and [86], we recall the governing equations (3.40) for a fully saturated, incompressible poroelastic model

$$-(\lambda + \mu)\nabla(\nabla \cdot \mathbf{u}) - \mu\nabla^2\mathbf{u} + \nabla p = \mathbf{f} \quad \text{in } \Omega \times (0, T), \quad (5.1a)$$

$$\mathbf{k}^{-1}\mathbf{z} + \nabla p = \mathbf{b} \quad \text{in } \Omega \times (0, T), \quad (5.1b)$$

$$\nabla \cdot (\mathbf{u}_t + \mathbf{z}) = g \quad \text{in } \Omega \times (0, T), \quad (5.1c)$$

$$\mathbf{u} = \mathbf{u}_D \quad \text{on } \Gamma_D \times (0, T), \quad (5.1d)$$

$$\boldsymbol{\sigma}\mathbf{n} = \mathbf{t}_N \quad \text{on } \Gamma_N \times (0, T), \quad (5.1e)$$

$$\mathbf{z} \cdot \mathbf{n} = q_D \quad \text{on } \Gamma_F \times (0, T), \quad (5.1f)$$

$$p = p_D \quad \text{on } \Gamma_P \times (0, T), \quad (5.1g)$$

$$\mathbf{u}(0, \cdot) = \mathbf{u}^0 \quad \text{in } \Omega. \quad (5.1h)$$

Remark 5.2.1. Since the above resulting system of equations is linear, for ease of presentation, we will assume all Dirichlet boundary conditions are homogeneous, ie., $\mathbf{u}_D = 0, q_D = 0, p_D = 0$.

5.2.2 Weak formulation

We define the following spaces for displacement, fluid flux and pressure respectively,

$$\begin{aligned}\mathbf{W}^E(\Omega) &= \{\mathbf{u} \in (H^1(\Omega))^d : \mathbf{u} = 0 \text{ on } \Gamma_D\}, \\ \mathbf{W}^D(\Omega) &= \{\mathbf{z} \in H_{div}(\Omega) : \mathbf{z} \cdot \mathbf{n} = 0 \text{ on } \Gamma_F\}, \\ \mathcal{L}(\Omega) &= \begin{cases} L^2(\Omega) & \text{if } \Gamma_N \cup \Gamma_P \neq \emptyset \\ L_0^2(\Omega) & \text{if } \Gamma_N \cup \Gamma_P = \emptyset, \end{cases},\end{aligned}$$

where $L_0^2(\Omega) = \{q \in L^2(\Omega) : \int_{\Omega} q \, dx = 0\}$, which we combine to construct the mixed solution space

$$\mathcal{W}^X = \{\mathbf{W}^E(\Omega) \times \mathbf{W}^D(\Omega) \times \mathcal{L}(\Omega)\}.$$

We define the bilinear form

$$a(\mathbf{u}, \mathbf{v}) = \int_{\Omega} 2\mu(\epsilon(\mathbf{u}) : \epsilon(\mathbf{v})) + \lambda(\nabla \cdot \mathbf{u})(\nabla \cdot \mathbf{v}) \, dx,$$

for $\mathbf{u}, \mathbf{v} \in \mathbf{W}^E(\Omega)$. This bilinear form is continuous such that

$$a(\mathbf{u}, \mathbf{v}) \leq C_c \|\mathbf{u}\|_{1,\Omega} \|\mathbf{v}\|_{1,\Omega} \quad \forall \mathbf{u}, \mathbf{v} \in (H^1(\Omega))^d. \quad (5.2)$$

Using Korn's inequality [19, 25], and $\int_{\Omega} \lambda(\nabla \cdot \mathbf{v})(\nabla \cdot \mathbf{v}) \geq 0$ we have

$$\|\mathbf{v}\|_{a,\Omega}^2 = a(\mathbf{v}, \mathbf{v}) \geq 2\mu \|\epsilon(\mathbf{v})\|_{0,\Omega}^2 \geq C_k \|\mathbf{v}_h\|_{1,\Omega}^2 \quad \forall \mathbf{v} \in \mathbf{W}^E(\Omega). \quad (5.3)$$

Since \mathbf{k} is assumed to be a symmetric and strictly positive definite tensor, there exists eigenfunctions $\lambda_{min}, \lambda_{max} > 0$ such that $\forall \mathbf{x} \in \Omega, \lambda_{min} \|\boldsymbol{\eta}\|_{0,\Omega} \leq \boldsymbol{\eta}^t \mathbf{k}(\mathbf{x}) \boldsymbol{\eta} \leq \lambda_{max} \|\boldsymbol{\eta}\|_{0,\Omega} \quad \forall \boldsymbol{\eta} \in \mathbb{R}^d$, and

$$\lambda_{min}^{-1} \|\mathbf{w}\|_{0,\Omega}^2 \geq (\mathbf{k}^{-1} \mathbf{w}, \mathbf{w}) \geq \lambda_{max}^{-1} \|\mathbf{w}\|_{0,\Omega}^2 \quad \forall \mathbf{w} \in \mathbf{W}^D(\Omega). \quad (5.4)$$

The continuous weak problem is: Find $\mathbf{u}(x, t) \in \mathbf{W}^E(\Omega), \mathbf{z}(x, t) \in \mathbf{W}^D(\Omega)$, and $p(x, t) \in \mathcal{L}(\Omega)$ for any time $t \in [0, T]$ such that:

$$a(\mathbf{u}, \mathbf{v}) - (p, \nabla \cdot \mathbf{v}) = (\mathbf{f}, \mathbf{v}) + (\mathbf{t}_N, \mathbf{v})_{\Gamma_N} \quad \forall \mathbf{v} \in \mathbf{W}^E(\Omega), \quad (5.5a)$$

$$(\mathbf{k}^{-1} \mathbf{z}, \mathbf{w}) - (p, \nabla \cdot \mathbf{w}) = (\mathbf{b}, \mathbf{w}) \quad \forall \mathbf{w} \in \mathbf{W}^D(\Omega), \quad (5.5b)$$

$$(\nabla \cdot \mathbf{u}_t, q) + (\nabla \cdot \mathbf{z}, q) = (g, q) \quad \forall q \in \mathcal{L}(\Omega). \quad (5.5c)$$

We will assume the following regularity requirements on the data,

$$\begin{aligned} \mathbf{f} &\in C^1([0, T]; (H^{-1}(\Omega))^d), & \mathbf{t}_N &\in C^1([0, T]; H^{-1/2}(\Gamma_N)), \\ \mathbf{b} &\in C^1([0, T]; H_{div}^{-1}(\Omega)), & g &\in C^0([0, T]; (L^2(\Omega))^d). \end{aligned} \quad (5.6)$$

For the initial conditions we require that $\mathbf{u}^0 \in (H^1(\Omega))^d$. The well-posedness of the continuous two-field formulation has been proven by [86]. [67] proves

well-posedness for the continuous three-field formulation (6.2). In this work we also establish the well-posedness of (6.2) as a result of the energy estimates proven in section 5.5, see remark 5.5.1.

5.2.3 Fully-discrete model

We define the following finite element spaces,

$$\begin{aligned} \mathbf{W}_h^E &= \left\{ \mathbf{u}_h \in C^0(\Omega) : \mathbf{u}_h|_K \in P_1(K) \ \forall K \in \mathcal{T}^h, \mathbf{u}_h = 0 \text{ on } \Gamma_D \right\}, \\ \mathbf{W}_h^D &= \left\{ \mathbf{z}_h \in C^0(\Omega) : \mathbf{z}_h|_K \in P_1(K) \ \forall K \in \mathcal{T}^h, \mathbf{z}_h \cdot \mathbf{n} = 0 \text{ on } \Gamma_F \right\}, \\ Q_h &= \begin{cases} \left\{ p_h : p_h|_K \in P_0(K) \ \forall K \in \mathcal{T}^h \right\} & \text{if } \Gamma_N \cup \Gamma_P \neq \emptyset \\ \left\{ p_h : p_h|_K \in P_0(K), \int_{\Omega} p_h = 0 \ \forall K \in \mathcal{T}^h \right\} & \text{if } \Gamma_N \cup \Gamma_P = \emptyset \end{cases}, \end{aligned}$$

where $P_0(K)$ and $P_1(K)$ are respectively the spaces of constant and linear polynomials on K . We partition $[0, T]$ into N evenly spaced non-overlapping regions $(t_{n-1}, t_n]$, $n = 1, 2, \dots, N$, where $t_n - t_{n-1} = \Delta t$. For any sufficiently smooth function $v(t, x)$ we define $v^n(x) = v(t_n, x)$ and the discrete time derivative by $v_{\Delta t}^n := \frac{v^n - v^{n-1}}{\Delta t}$.

The fully discrete weak problem is: For $n = 1, 2, \dots, N$, $\mathbf{u}_h^n \in \mathbf{W}_h^E$, find $\mathbf{z}_h^n \in \mathbf{W}_h^D$ and $p_h^n \in Q_h$ such that

$$a(\mathbf{u}_h^n, \mathbf{v}_h) - (p_h^n, \nabla \cdot \mathbf{v}_h) = (\mathbf{f}^n, \mathbf{v}_h) + (\mathbf{t}_N, \mathbf{v}_h)_{\Gamma_N} \quad \forall \mathbf{v}_h \in \mathbf{W}_h^E, \quad (5.7a)$$

$$(\mathbf{k}^{-1} \mathbf{z}_h^n, \mathbf{w}_h) - (p_h^n, \nabla \cdot \mathbf{w}_h) = (\mathbf{b}^n, \mathbf{w}_h) \quad \forall \mathbf{w}_h \in \mathbf{W}_h^D, \quad (5.7b)$$

$$(\nabla \cdot \mathbf{u}_{\delta t, h}^n, q_h) + (\nabla \cdot \mathbf{z}_h^n, q_h) + J(p_{\delta t, h}^n, q_h) = (g^n, q_h) \quad \forall q_h \in Q_h. \quad (5.7c)$$

The stabilization term is

$$J(p, q) = \delta \sum_K \int_{\partial K \setminus \partial \Omega} h_{\partial K} [p][q] \, ds. \quad (5.8)$$

Here δ is a stabilization parameter that is independent of h and Δt . Here $h_{\partial K}$ denotes the size (diameter) of an element edge in 2D or face in 3D, and $[\cdot]$ is the jump across an edge or face (taken on the interior edges only). We will see in the numerical results, section 6.5 that the convergence is not sensitive to δ . The set of all elements is denoted by K , $h_{\partial K}$ denotes the size of an element edge in 2D or face in 3D, and $[\cdot]$ is the jump across an edge. As an example consider $[p_h]$, the jump operator on the piecewise constant pressure. The jump in pressure $[p_h]$ across an element or face E adjoining elements T and S is defined such that

$$(p_h|_T - p_h|_S) \mathbf{n}_{E,T} = (p_h|_S - p_h|_T) \mathbf{n}_{E,S}.$$

Here $\mathbf{n}_{E,T}$ is the outward normal from element T , with respect to edge E , $\mathbf{n}_{E,S}$ is the corresponding inward facing normal, and $p_h|_T$ and $p_h|_S$ denote the pressure in element T and S , respectively.

We also assume

$$a(\mathbf{u}_h^0, \mathbf{v}_h) = a(\mathbf{u}^0, \mathbf{v}_h) \quad \forall \mathbf{v}_h \in \mathbf{W}_h^E, \quad (5.9a)$$

$$J(p_h^0, q_h) = J(p^0, q_h) \quad \forall q_h \in Q_h, \quad (5.9b)$$

where $p^0 \in \mathcal{L}(\Omega)$.

5.3 Norms and inequalities

In this section we will introduce some norms and inequalities required for the remainder of this chapter. Throughout this work, we will let C denote a generic positive constant, whose value may change from instance to instance, but is independent of any mesh parameters.

5.3.1 Useful inequalities

Detailed derivations of the following four inequalities can be found in [19]. If $f, g \in L^2(\Omega)$ then by the **Cauchy-Schwarz** inequality we have

$$\int_{\Omega} |f(x)g(x)|dx \leq \|f\|_{0,\Omega} \|g\|_{0,\Omega}.$$

From the **triangle inequality** we have

$$\|f + g\|_{0,\Omega} \leq \|f\|_{0,\Omega} + \|g\|_{0,\Omega}.$$

For any real numbers a and b , by **Young's inequality**,

$$ab \leq \frac{\epsilon}{2}a^2 + \frac{1}{2\epsilon}b^2 \quad \forall \epsilon > 0.$$

This inequality is sometimes referred to as the arithmetic-geometric mean inequality. Next, the **Poincaré inequality**, also known as Poincaré-Friedrich's inequality says

$$\|v\|_{0,\Omega} \leq C_p \|\nabla v\|_{0,\Omega} \quad \forall v \in H^1(\Omega).$$

5.3.2 J-norm

The stabilization term gives rise to the semi-norm

$$|q|_{J,\Omega} := J(q, q)^{1/2}.$$

Using the scaling argument, also used in [22],

$$\|h^{1/2} p_h\|_{0,\partial K} \leq c_z \|p_h\|_{0,K}, \quad (5.10)$$

Cauchy-Schwarz and the triangle inequality the following bounds for the stabilization term hold.

$$|p_h|_{J,\Omega} \leq C \|p_h\|_{0,\Omega} \text{ and } J(p_h, q_h) \leq |p_h|_{J,\Omega} |q_h|_{J,\Omega}, \quad \forall p_h, q_h \in Q_h. \quad (5.11)$$

Furthermore, for any $q \in H^1(\Omega)$,

$$J(p, q) = 0, \quad \forall p \in \mathcal{L}(\Omega), \quad (5.12)$$

see lemma 1.23 in [32].

5.3.3 Approximation results

We now give some approximation results that will be useful later. Let $\pi_h^1 : H^1(\Omega) \rightarrow \mathbf{W}_h^E$ and $\pi_h^0 : L^2(\Omega) \rightarrow Q_h$ be Clément projections (interpolation operators), see [25].

Lemma 5.3.1. *For all $v \in (H^2(\Omega))^d$ and $q \in H^1(\Omega)$ the interpolation operators satisfy: For $s = 0, 1$*

$$\|v - \pi_h^1 v\|_{s,\Omega} \leq Ch^{2-s} \|v\|_{2,\Omega}, \quad (5.13)$$

$$\|q - \pi_h^0 q\|_{0,\Omega} \leq Ch \|q\|_{1,\Omega}, \quad (5.14)$$

$$|q - \pi_h^0 q|_{J,\Omega} \leq Ch \|q\|_{1,\Omega}. \quad (5.15)$$

Proof. The first two results are standard [19]. The final result is obtained by using the element error estimate provided in [96] and then summing over all elements. \square

Due to the surjectivity of the divergence operator, for every $p \in L^2(\Omega)$ there exists a function $\mathbf{v}_p \in (H^1(\Omega))^d$ such that $\nabla \cdot \mathbf{v}_p = -p$ and $\|\mathbf{v}_p\|_{1,\Omega} \leq c\|p\|_{0,\Omega}$. This last inequality can be shown to hold by considering the famous inf-sup condition related to the continuous Stokes problem [19, 21]. We assume that the projection, $\pi_h^1 \mathbf{v}_p$, is stable such that

$$\|\pi_h^1 \mathbf{v}_p\|_{1,\Omega} \leq \hat{c} \|p\|_{0,\Omega}. \quad (5.16)$$

Furthermore, for any element $K \in \mathcal{T}^h$

$$\|\mathbf{v}_p - \pi_h^1 \mathbf{v}_p\|_{L^2(K)} \leq Ch \|\mathbf{v}_p\|_{H^1(\omega_K)}, \quad (5.17)$$

where ω_K is a domain made of the elements in \mathcal{T}^h neighboring K , i.e. the union of all elements $J \in \mathcal{T}^h$ such that $\bar{K} \cap \bar{J} \neq \emptyset$. For more details about the properties of this projection we refer to section 4.8 in [19]. This projection will allow us to obtain stability of the pressure and avoid spurious pressure oscillations. The discrepancy between the projection and its continuous counterpart will eventually be made up by the stabilization term, shown in section 5.4. Combining the above with the trace inequality, see lemma 3.1 in [96],

$$\|(\mathbf{v}_p - \pi_h^1 \mathbf{v}_p) \cdot \mathbf{n}\|_{0,\partial K}^2 \leq C \|\mathbf{v}_p - \pi_h^1 \mathbf{v}_p\|_{0,K} (h^{-1} \|\mathbf{v}_p - \pi_h^1 \mathbf{v}_p\|_{0,K} + \|\mathbf{v}_p - \pi_h^1 \mathbf{v}_p\|_{1,K}), \quad (5.18)$$

we obtain

$$\|(\mathbf{v}_p - \pi_h^1 \mathbf{v}_p) \cdot \mathbf{n}\|_{0,\partial K}^2 \leq Ch \|\mathbf{v}_p\|_{H^1(\omega_K)}^2. \quad (5.19)$$

Taking into account $\|\mathbf{v}_p\|_{1,\Omega} \leq c \|p\|_{0,\Omega}$, we may write

$$\sum_K \int_{\partial K} h^{-1} |(\mathbf{v}_p - \pi_h^1 \mathbf{v}_p) \cdot \mathbf{n}|^2 ds \leq c_t \|p\|_{0,\Omega}^2. \quad (5.20)$$

We also have the following approximation for the time-discretization er-

ror: For all $v \in H^2(0, T; (L^2(\Omega))^d)$

$$\sum_{n=1}^N \Delta t \left\| v_{\Delta t}^n - \frac{\partial v}{\partial t}(t^n, \cdot) \right\|_{0,\Omega}^2 \leq \Delta t^2 \int_0^T \|v_{tt}\|_{0,\Omega}^2 ds. \quad (5.21)$$

See [19, 93] for details.

5.3.4 Triple-norms

For all $[v, w, q] \in [(H^1(\Omega))^d \times H_{div}(\Omega) \times L^2(\Omega)]$ we define the norm

$$\| \cdot \|_A^2 := \|v\|_{1,\Omega}^2 + \Delta t^2 \|\nabla \cdot w\|_{0,\Omega}^2 + \Delta t \|w\|_{0,\Omega}^2 + \|q\|_{0,\Omega}^2 + |q|_{J,\Omega}^2. \quad (5.22)$$

For all $[v, w, q] \in [L^\infty(0, T; (H^1(\Omega))^d) \times L^2(0, T; H_{div}(\Omega)) \times L^2(0, T; L^2(\Omega))]$ the norm

$$\| \cdot \|_B^2 := \|v\|_{L^\infty(H^1)}^2 + \|w\|_{L^2(L^2)}^2 + \|q\|_{L^2(L^2)}^2, \quad (5.23)$$

5.4 Existence and uniqueness of solutions to the fully-discrete model

Well-posedness of the unstabilized fully-discretized system (5.7) (i.e., for $\delta = 0$), with the use of a low order Raviart-Thomas approximation for the fluid velocity is shown by [80] for $c_0 > 0$, and by [67] for $c_0 \geq 0$. Although as the permeability tends to zero and the porous mixture becomes impermeable,

the three-field linear poroelasticity tends to a mixed linear elasticity problem [43]. Hence, in this case this element becomes unstable, as expected since the elasticity $P1 - P0$ approximation is known to be unstable. Our method is stable for both the Darcy problem (as the elasticity coefficients tend to infinity) and the mixed linear elasticity problem (as the permeability tends to zero), and is therefore stable for all permeabilities and elasticity coefficients.

Combining the fully discrete equations (5.7a), (5.7b) and (5.7c), after first multiplying (5.7b) and (5.7c) by Δt , gives the equivalent problem; For $n = 1, 2, \dots, n$ find $(\mathbf{u}_h, \mathbf{z}_h, p_h)$ such that

$$\begin{aligned} & B_h^n[(\mathbf{u}_h, \mathbf{z}_h, p_h), (\mathbf{v}_h, \mathbf{w}_h, q_h)] \\ &= (\mathbf{f}^n, \mathbf{v}_h) + (\mathbf{t}_N, \mathbf{v}_h)_{\Gamma_N} + \Delta t(\mathbf{b}^n, \mathbf{w}_h) + \Delta t(g^n, q_h) \\ &\quad + (\nabla \cdot \mathbf{u}_h^{n-1}, q_h) + J(p_h^{n-1}, q_h) \quad \forall (\mathbf{v}_h, \mathbf{w}_h, q_h) \in \mathcal{W}_h^X, \end{aligned}$$

where

$$\begin{aligned} & B_h^n[(\mathbf{u}_h, \mathbf{z}_h, p_h), (\mathbf{v}_h, \mathbf{w}_h, q_h)] \\ &= a(\mathbf{u}_h^n, \mathbf{v}_h) + \Delta t(\mathbf{k}^{-1} \mathbf{z}_h^n, \mathbf{w}_h) - (p_h^n, \nabla \cdot \mathbf{v}_h) - \Delta t(p_h^n, \nabla \cdot \mathbf{w}_h) \\ &\quad + (\nabla \cdot \mathbf{u}_h^n, q_h) + \Delta t(\nabla \cdot \mathbf{z}_h^n, q_h) + J(p_h^n, q_h). \quad (5.24) \end{aligned}$$

The linear form satisfies the following continuity property

$$|B_h^n[(\mathbf{u}_h, \mathbf{z}_h, p_h), (\mathbf{v}_h, \mathbf{w}_h, q_h)]| \leq C \|(\mathbf{u}_h^n, \mathbf{z}_h^n, p_h^n)\|_A \|(\mathbf{v}_h, \mathbf{w}_h, q_h)\|_A.$$

We apply Babuska's theory [9] to show well-posedness (existence and uniqueness) of this discretized system at a particular time step. This requires us to prove a discrete inf-sup type result (Theorem 5.4.1) for the combined bilinear form (5.24).

Theorem 5.4.1. *Let $\gamma > 0$ be a constant independent of any mesh parameters. Then the finite element formulation (5.7) satisfies the following discrete inf-sup condition*

$$\gamma \|\|(\mathbf{u}_h^n, \mathbf{z}_h^n, p_h^n)\|\|_A \leq \sup_{(\mathbf{v}_h, \mathbf{w}_h, q_h) \in \mathcal{V}_h^X} \frac{B_h^n[(\mathbf{u}_h, \mathbf{z}_h, p_h), (\mathbf{v}_h, \mathbf{w}_h, q_h)]}{\|\|(\mathbf{v}_h, \mathbf{w}_h, q_h)\|\|_A} \quad \forall (\mathbf{u}_h, \mathbf{z}_h, p_h) \in \mathcal{W}_h^X. \quad (5.25)$$

Hence, given a solution at the previous time step the linear system arising from the fully discrete method for the subsequent time step is non-singular.

The following proof follows ideas presented by [22].

Proof.

Step 1, bounding $\|\mathbf{u}_h^n\|_{1,\Omega}$, $\Delta t^{1/2}\|\mathbf{z}_h^n\|_{0,\Omega}$, and $|p_h^n|_{J,\Omega}$.

Choose $(\mathbf{v}_h, \mathbf{w}_h, q_h) = (\mathbf{u}_h^n, \mathbf{z}_h^n, p_h^n)$, then using (5.3) and (5.4), we obtain,

$$\begin{aligned} B_h^n[(\mathbf{u}_h, \mathbf{z}_h, p_h), (\mathbf{u}_h^n, \mathbf{z}_h^n, p_h^n)] &= a(\mathbf{u}_h^n, \mathbf{u}_h^n) + \Delta t(\mathbf{k}^{-1}\mathbf{z}_h^n, \mathbf{z}_h^n) + J(p_h^n, p_h^n) \\ &\geq C_k \|\mathbf{u}_h^n\|_{1,\Omega}^2 + \lambda_{max}^{-1} \Delta t \|\mathbf{z}_h^n\|_{0,\Omega}^2 + |p_h^n|_{J,\Omega}^2. \end{aligned} \quad (5.26)$$

Step 2, bounding $\|p_h^n\|_{0,\Omega}$.

Choose $(\mathbf{v}_h, \mathbf{w}_h, q_h) = (\pi_h^1 \mathbf{v}_{p_h^n}, 0, 0)$ and add $0 = \|p_h^n\|_{0,\Omega}^2 + (p_h^n, \nabla \cdot \mathbf{v}_{p_h^n})$ to obtain

$$B_h^n[(\mathbf{u}_h, \mathbf{z}_h, p_h), (\pi_h^1 \mathbf{v}_{p_h^n}, 0, 0)] = a(\mathbf{u}_h^n, \pi_h^1 \mathbf{v}_{p_h^n}) + \|p_h^n\|_{0,\Omega}^2 + (p_h^n, \nabla \cdot (\mathbf{v}_{p_h^n} - \pi_h^1 \mathbf{v}_{p_h^n})). \quad (5.27)$$

Focusing on the third term in (5.27) only, we apply the divergence theorem and split the integral over local elements to get

$$(p_h^n, \nabla \cdot (\mathbf{v}_{p_h^n} - \pi_h^1 \mathbf{v}_{p_h^n})) = \sum_K \int_{\partial K} p_h^n (\mathbf{v}_{p_h^n} - \pi_h^1 \mathbf{v}_{p_h^n}) \cdot \mathbf{n} \, ds = \sum_K \frac{1}{2} \int_{\partial K} [p_h^n] (\mathbf{v}_{p_h^n} - \pi_h^1 \mathbf{v}_{p_h^n}) \cdot \mathbf{n} \, ds.$$

We thus have

$$B_h^n[(\mathbf{u}_h, \mathbf{z}_h, p_h), (\pi_h^1 \mathbf{v}_{p_h^n}, 0, 0)] = \|p_h^n\|_{0,\Omega}^2 + a(\mathbf{u}_h^n, \pi_h^1 \mathbf{v}_{p_h^n}) + \sum_K \frac{1}{2} \int_{\partial K} [p_h^n] (\mathbf{v}_{p_h^n} - \pi_h^1 \mathbf{v}_{p_h^n}) \cdot \mathbf{n} \, ds.$$

Now first applying the Cauchy-Schwarz inequality and (5.2) on the right hand side to get

$$\begin{aligned} B_h^n[(\mathbf{u}_h, \mathbf{z}_h, p_h), (\pi_h^1 \mathbf{v}_{p_h^n}, 0, 0)] &\geq \|p_h^n\|_{0,\Omega}^2 - C_c \|\mathbf{u}_h^n\|_{1,\Omega} \|\pi_h^1 \mathbf{v}_{p_h^n}\|_{1,\Omega} \\ &\quad - \sum_K \frac{1}{2} \left(\int_{\partial K} (h^{1/2} [p_h^n])^2 \, ds \right)^{1/2} \cdot \left(\int_{\partial K} (h^{-1/2} (\mathbf{v}_{p_h^n} - \pi_h^1 \mathbf{v}_{p_h^n}) \cdot \mathbf{n})^2 \, ds \right)^{1/2}. \end{aligned}$$

Now apply Young's inequality and (5.16) to obtain

$$\begin{aligned} B_h^n[(\mathbf{u}_h, \mathbf{z}_h, p_h), (\pi_h^1 \mathbf{v}_{p_h^n}, 0, 0)] &\geq \|p_h^n\|_{0,\Omega}^2 - \frac{C_c^2}{2\epsilon} \|\mathbf{u}_h^n\|_{1,\Omega}^2 - \frac{\epsilon \hat{c}}{2} \|p_h^n\|_{0,\Omega}^2 \\ &\quad - \frac{1}{2\epsilon\delta} J(p_h^n, p_h^n) - \frac{\epsilon}{2} \sum_K \int_{\partial K} h^{-1} |(\mathbf{v}_{p_h^n} - \pi_h^1 \mathbf{v}_{p_h^n}) \cdot \mathbf{n}|^2 ds. \end{aligned}$$

Applying (5.20) we obtain

$$\begin{aligned} B_h^n[(\mathbf{u}_h, \mathbf{z}_h, p_h), (\pi_h^1 \mathbf{v}_{p_h^n}, 0, 0)] &\geq -\frac{C_c^2}{2\epsilon} \|\mathbf{u}_h^n\|_{1,\Omega}^2 + \left(1 - (\hat{c} + c_t) \frac{\epsilon}{2}\right) \|p_h^n\|_{0,\Omega}^2 - \frac{1}{2\epsilon\delta} |p_h^n|_{J,\Omega}^2. \end{aligned} \tag{5.28}$$

Step 3, bounding $\Delta t \|\nabla \cdot \mathbf{z}_h^n\|_{0,\Omega}$.

Choosing $(\mathbf{v}_h, \mathbf{w}_h, q_h) = (0, 0, \Delta t \nabla \cdot \mathbf{z}_h^n)$ yields

$$B_h^n[(\mathbf{u}_h, \mathbf{z}_h, p_h), (0, 0, \Delta t \nabla \cdot \mathbf{z}_h^n)] = (\nabla \cdot \mathbf{u}_h^n, \Delta t \nabla \cdot \mathbf{z}_h^n) + \Delta t^2 \|\nabla \cdot \mathbf{z}_h^n\|_{0,\Omega}^2 + J(p_h^n, \Delta t \nabla \cdot \mathbf{z}_h^n).$$

We bound the first term using the Cauchy-Schwarz inequality followed by Young's inequality such that

$$(\nabla \cdot \mathbf{u}_h^n, \Delta t \nabla \cdot \mathbf{z}_h^n) \leq \frac{C_p}{2\epsilon} \|\mathbf{u}_h^n\|_{1,\Omega}^2 + \frac{\epsilon \Delta t^2}{2} \|\nabla \cdot \mathbf{z}_h^n\|_{0,\Omega}^2.$$

We can also bound the third term as before using the Cauchy-Schwarz in-

equality followed by Young's inequality such that

$$\begin{aligned}
J(p_h^n, \Delta t \nabla \cdot \mathbf{z}_h^n) &\leq \frac{1}{2\epsilon} J(p_h^n, p_h^n) + \frac{\epsilon \Delta t^2}{2} J(\nabla \cdot \mathbf{z}_h^n, \nabla \cdot \mathbf{z}_h^n) \\
&= \frac{1}{2\epsilon} J(p_h^n, p_h^n) + \epsilon \delta \Delta t^2 \sum_K \int_{\partial K} |h^{1/2} \nabla \cdot \mathbf{z}_h^n|^2 \, ds \\
&\leq \frac{1}{2\epsilon} J(p_h^n, p_h^n) + \epsilon \delta c_z \Delta t^2 \|\nabla \cdot \mathbf{z}_h^n\|_{0,\Omega}^2. \quad (5.29)
\end{aligned}$$

Here we have used the scaling argument (5.10) which relates line and surface integrals and assumes that $\nabla \cdot \mathbf{z}_h^n$ is element-wise constant, and (5.11). This yields

$$\begin{aligned}
B_h^n[(\mathbf{u}_h, \mathbf{z}_h, p_h), (0, 0, \Delta t \nabla \cdot \mathbf{z}_h^n)] &\geq (1 - \epsilon \delta c_z - \frac{\epsilon}{2}) \Delta t^2 \|\nabla \cdot \mathbf{z}_h^n\|_{0,\Omega}^2 \\
&\quad - \frac{1}{2\epsilon} |p_h^n|_{J,\Omega}^2 - \frac{C_p}{2\epsilon} \|\mathbf{u}_h^n\|_{1,\Omega}^2. \quad (5.30)
\end{aligned}$$

Step 4, Combining steps 1-3.

Finally we can combine (5.26), (5.28) and (5.30) to get control over all the norms by choosing $(\mathbf{v}_h, \mathbf{w}_h, q_h) = (\beta \mathbf{u}_h^n + \pi_h^1 \mathbf{v}_{p_h^n}, \beta \mathbf{z}_h^n, \beta p_h^n + \Delta t \nabla \cdot \mathbf{z}_h^n)$, which

yields

$$\begin{aligned}
B_h^n[(\mathbf{u}_h, \mathbf{z}_h, p_h), (\beta \mathbf{u}_h^n + \pi_h^1 \mathbf{v}_{p_h^n}, \beta \mathbf{z}_h^n, \beta p_h^n + \Delta t \nabla \cdot \mathbf{z}_h^n)] &\geq \\
(\beta C_k - \frac{C_c^2 + C_p}{2\epsilon}) \|\mathbf{u}_h^n\|_{1,\Omega}^2 + \beta \lambda_{max}^{-1} \Delta t \|\mathbf{z}_h^n\|_{0,\Omega}^2 + \left(1 - \epsilon \delta c_z - \frac{\epsilon}{2}\right) \Delta t^2 \|\nabla \cdot \mathbf{z}_h^n\|_{0,\Omega}^2 \\
+ \left(1 - (\hat{c} + c_t) \frac{\epsilon}{2}\right) \|p_h^n\|_{0,\Omega}^2 + \left(\beta - \frac{1}{2\epsilon} - \frac{1}{2\epsilon\delta}\right) |p_h^n|_{J,\Omega}^2, \quad (5.31)
\end{aligned}$$

where we can choose

$$\beta \geq \max \left[\frac{C_c^2 + C_p}{2\epsilon C_k} + \frac{1 - \bar{C}\epsilon}{C_k}, \lambda_{max} (1 - \bar{C}\epsilon), \frac{1}{2\epsilon} + \frac{1}{2\epsilon\delta} + 1 - \bar{C}\epsilon \right],$$

with $\bar{C} = \max \left[\frac{\hat{c} + c_t}{2}, \delta c_z - \frac{1}{2} \right]$. This yields

$$B_h^n[(\mathbf{u}_h, \mathbf{z}_h, p_h), (\beta \mathbf{u}_h^n + \pi_h^1 \mathbf{v}_{p_h^n}, \beta \mathbf{z}_h^n, \beta p_h^n + \nabla \cdot \mathbf{z}_h^n)] \geq (1 - \bar{C}\epsilon) \|\|(\mathbf{u}_h^n, \mathbf{z}_h^n, p_h^n)\|\|_A^2.$$

To complete the proof, we let $(\mathbf{v}_h, \mathbf{w}_h, q_h) = (\beta \mathbf{u}_h^n + \pi_h^1 \mathbf{v}_{p_h^n}, \beta \mathbf{z}_h^n, \beta p_h^n + \Delta t \nabla \cdot \mathbf{z}_h^n)$ and show that for ϵ sufficiently small there exists a constant C such that $\|\|(\mathbf{u}_h^n, \mathbf{z}_h^n, p_h^n)\|\|_A \geq C \|\|(\mathbf{v}_h, \mathbf{w}_h, q_h)\|\|_A$. Using the triangle inequality and (5.16) we obtain

$$\begin{aligned}
&\|\|(\beta \mathbf{u}_h^n + \pi_h^1 \mathbf{v}_{p_h^n}, \beta \mathbf{z}_h^n, \beta p_h^n + \Delta t \nabla \cdot \mathbf{z}_h^n)\|\|_A^2 \\
&\leq C \left(\beta^2 \|\mathbf{u}_h^n\|_{1,\Omega}^2 + \|\pi_h^1 \mathbf{v}_{p_h^n}\|_{1,\Omega}^2 + \Delta t^2 (1 + \beta)^2 \|\nabla \cdot \mathbf{z}_h^n\|_{0,\Omega}^2 + \beta^2 \Delta t \|\mathbf{z}_h^n\|_{0,\Omega}^2 \right. \\
&\quad \left. + \beta^2 \|p_h^n\|_{0,\Omega}^2 + \beta^2 |p_h^n|_{J,\Omega}^2 + \Delta t^2 |\nabla \cdot \mathbf{z}_h^n|_{J,\Omega}^2 \right) \\
&\leq C \|\|(\mathbf{u}_h^n, \mathbf{z}_h^n, p_h^n)\|\|_A^2,
\end{aligned}$$

as desired. \square

5.5 Energy estimate for the fully-discrete model

In this section we construct two new combined bilinear forms, $B_{\Delta t, h}^n$ (lemmas 5.5.1 and 5.5.2) and \mathcal{B}_h^n (lemmas 5.5.3 and 5.5.4). These bilinear forms are bounded below by Lemmas 5.5.1 and 5.5.3 respectively. Lemma 5.5.2 uses lemma 5.5.1 to provide a bound on \mathbf{u}_h , \mathbf{z}_h and p_h . Lemma 5.5.4 uses lemma 5.5.3 to provide a bound on $\nabla \cdot \mathbf{z}_h$.

5.5.1 Bound on the displacement, fluid flux and pressure

Adding (5.7a), (5.7b) and (5.7c), and assuming $\mathbf{t}_N = 0$ on Γ_t , we get the following

$$B_{\Delta t, h}^n[(\mathbf{u}_h, \mathbf{z}_h, p_h), (\mathbf{v}_h, \mathbf{w}_h, q_h)] = (\mathbf{f}^n, \mathbf{v}_h) + (\mathbf{b}^n, \mathbf{w}_h) + (g^n, q_h) \quad \forall (\mathbf{v}_h, \mathbf{w}_h, q_h) \in \mathcal{W}_h^X, \quad (5.32)$$

where

$$\begin{aligned} B_{\Delta t, h}^n[(\mathbf{u}_h, \mathbf{z}_h, p_h), (\mathbf{v}_h, \mathbf{w}_h, q_h)] &= a(\mathbf{u}_h^n, \mathbf{v}_h) + (\mathbf{k}^{-1} \mathbf{z}_h^n, \mathbf{w}_h) - (p_h^n, \nabla \cdot \mathbf{v}_h) \\ &\quad - (p_h^n, \nabla \cdot \mathbf{w}_h) + (\nabla \cdot \mathbf{u}_{\delta t, h}^n, q_h) + (\nabla \cdot \mathbf{z}_h^n, q_h) + J(p_{\delta t, h}^n, q_h). \end{aligned} \quad (5.33)$$

Lemma 5.5.1. $(\mathbf{u}_h, \mathbf{z}_h, p_h)$ satisfies

$$\begin{aligned} & \left(\sum_{n=1}^N \Delta t B_{\Delta t, h}^n [(\mathbf{u}_h, \mathbf{z}_h, p_h), (\mathbf{u}_{\delta t, h}^n + \pi_h^1 \mathbf{v}_{p_h^n}, \mathbf{z}_h^n, p_h^n)] \right. \\ & \quad \left. + \|\mathbf{u}_h^0\|_{1,\Omega}^2 + |p_h^0|_{J,\Omega}^2 + \|\mathbf{u}_h\|_{L^2(H^1)}^2 + \|p_h\|_{L^2(J)}^2 \right) \\ & \geq C \left(\|\mathbf{u}_h^N\|_{1,\Omega}^2 + |p_h^N|_{J,\Omega}^2 + \|\mathbf{z}_h\|_{L^2(L^2)}^2 + \|p_h\|_{L^2(L^2)}^2 \right). \end{aligned}$$

Proof. For $n = 1, 2, \dots, N$ we choose $(\mathbf{v}_h, \mathbf{w}_h, q_h) = (\mathbf{u}_{\delta t, h}^n + \pi_h^1 \mathbf{v}_{p_h^n}, \mathbf{z}_h^n, p_h^n)$ in (5.33), multiplying by Δt , and summing over all time steps, we get

$$\begin{aligned} & \sum_{n=1}^N \Delta t B_{\Delta t, h}^n [(\mathbf{u}_h, \mathbf{z}_h, p_h), (\mathbf{u}_{\delta t, h}^n + \pi_h^1 \mathbf{v}_{p_h^n}, \mathbf{z}_h^n, p_h^n)] \\ & = \sum_{n=1}^N \Delta t a(\mathbf{u}_h^n, \mathbf{u}_{\delta t, h}^n) + \sum_{n=1}^N \Delta t J(p_{\delta t, h}^n, p_h^n) + \sum_{n=1}^N \Delta t \mathbf{k}^{-1}(\mathbf{z}_h^n, \mathbf{z}_h^n) \\ & \quad + \sum_{n=1}^N \Delta t a(\mathbf{u}_h^n, \pi_h^1 \mathbf{v}_{p_h^n}) - \sum_{n=1}^N \Delta t (p_h^n, \nabla \cdot \pi_h^1 \mathbf{v}_{p_h^n}). \quad (5.34) \end{aligned}$$

We now bound each of the above terms on the right hand side of (5.34) individually before combining the results.

$$\begin{aligned} \sum_{n=1}^N \Delta t a(\mathbf{u}_h^n, \mathbf{u}_{\delta t, h}^n) & = \sum_{n=1}^N \Delta t \left(\frac{1}{\Delta t} \|\mathbf{u}_h^n\|_{a,\Omega}^2 - \frac{1}{\Delta t} a(\mathbf{u}_h^n, \mathbf{u}_h^{n-1}) \right) \\ & \geq \frac{C_k}{2} \|\mathbf{u}_h^N\|_{1,\Omega}^2 - \frac{C_c}{2} \|\mathbf{u}_h^0\|_{1,\Omega}^2, \end{aligned} \quad (5.35)$$

where we have used (5.2) and (5.3) in the last step. Using (5.28) we have

$$\begin{aligned} \sum_{n=1}^N \Delta t a(\mathbf{u}_h^n, \pi_h^1 \mathbf{v}_p) - \sum_{n=1}^N \Delta t(p_h^n, \nabla \cdot \pi_h^1 \mathbf{v}_p) &\geq -\frac{C_c}{2\epsilon} \|\mathbf{u}_h\|_{L^2(H^1)}^2 \\ &+ \left(1 - \left(\hat{c} + \frac{c_t}{2}\right) \frac{\epsilon}{2}\right) \|p_h\|_{L^2(L^2)}^2 - \frac{1}{4\epsilon} \|p_h\|_{L^2(J)}^2. \end{aligned}$$

Using (5.4),

$$\sum_{n=1}^N \Delta t(\mathbf{k}^{-1}(\mathbf{z}_h^n, \mathbf{z}_h^n)) \geq \lambda_{max}^{-1} \|\mathbf{z}_h\|_{L^2(L^2)}^2. \quad (5.36)$$

The intermediate steps for the next bound have been omitted because they are very similar to (5.35). Thus

$$\sum_{n=1}^N \Delta t J(p_{\delta t, h}^n, p_h^n) \geq \frac{1}{2} |p_h^N|_{J, \Omega}^2 - \frac{1}{2} |p_h^0|_{J, \Omega}^2. \quad (5.37)$$

We can now combine these intermediate results (5.35), (5.5.1), (5.36) and (5.37) to obtain from (5.34)

$$\begin{aligned} \sum_{n=0}^N \Delta t B_{\delta t, h}^n[(\mathbf{u}_h, \mathbf{z}_h, p_h), (\mathbf{u}_{\delta t, h}^n + \pi_h^1 \mathbf{v}_p, \mathbf{z}_h^n, p_h^n)] &+ \frac{C_c}{2} \|\mathbf{u}_h^0\|_{1, \Omega}^2 \\ &+ \frac{C_c}{2\epsilon} \|\mathbf{u}_h\|_{L^2(H^1)}^2 + \frac{1}{4\epsilon} \|p_h\|_{L^2(J)}^2 + \frac{1}{2} |p_h^0|_{J, \Omega}^2 \\ &\geq \frac{C_k}{2} \|\mathbf{u}_h^N\|_{1, \Omega}^2 + \frac{1}{2} |p_h^N|_{J, \Omega}^2 + \lambda_{max}^{-1} \|\mathbf{z}_h\|_{L^2(L^2)}^2 + (1 - C\epsilon) \|p_h\|_{L^2(L^2)}^2. \quad (5.38) \end{aligned}$$

Finally, choosing ϵ sufficiently small completes the proof.

□

Lemma 5.5.2. $(\mathbf{u}_h, \mathbf{z}_h, p_h)$ satisfies

$$\|\mathbf{u}_h^N\|_{1,\Omega}^2 + |p_h^N|_{J,\Omega}^2 + \|\mathbf{z}_h\|_{L^2(L^2)}^2 + \|p_h\|_{L^2(L^2)}^2 \leq C(T).$$

Proof. For $n = 1, 2, \dots, N$ we choose $(\mathbf{v}_h, \mathbf{w}_h, q_h) = (\mathbf{u}_{\delta t,h}^n + \pi_h^1 \mathbf{v}_{p_h^n}, \mathbf{z}_h^n, p_h^n)$ in (5.33), multiplying by Δt , and summing yields

$$\begin{aligned} \sum_{n=1}^N \Delta t B_{\Delta t,h}^n [(\mathbf{u}_h^n, \mathbf{z}_h^n, p_h^n), (\mathbf{u}_{\delta t,h}^n + \pi_h^1 \mathbf{v}_{p_h^n}, \mathbf{z}_h^n, p_h^n)] &= \sum_{n=1}^N \Delta t (\mathbf{f}^n, \mathbf{u}_{\delta t,h}^n + \pi_h^1 \mathbf{v}_{p_h^n}) \\ &\quad + \sum_{n=1}^N \Delta t (\mathbf{b}^n, \mathbf{z}_h^n) + \sum_{n=1}^N \Delta t (g^n, p_h^n). \end{aligned}$$

Let us note that,

$$\begin{aligned} \sum_{n=1}^N \Delta t (\mathbf{f}^n, \mathbf{u}_{\delta t,h}^n) &= \sum_{n=1}^N (\mathbf{f}^n, \mathbf{u}_h^n - \mathbf{u}_h^{n-1}) \\ &= (\mathbf{f}^N, \mathbf{u}_h^N) - (\mathbf{f}^1, \mathbf{u}_h^0) - \sum_{n=1}^{N-1} (\mathbf{f}^{n+1} - \mathbf{f}^n, \mathbf{u}_h^n), \quad (5.39) \end{aligned}$$

and further that

$$\begin{aligned} - \sum_{n=1}^{N-1} (\mathbf{f}^{n+1} - \mathbf{f}^n, \mathbf{u}_h^n) &\leq C \sum_{n=1}^{N-1} \|\mathbf{f}^{n+1} - \mathbf{f}^n\|_{0,\Omega} \|\mathbf{u}_h^n\|_{0,\Omega} \\ &\leq C \sum_{n=1}^{N-1} \left\{ \int_{t_n}^{t_{n+1}} \|\mathbf{f}_t\|_{0,\Omega} \right\}^{1/2} \|\mathbf{u}_h^n\|_{1,\Omega} \leq C \left(\frac{1}{2\epsilon} \|\mathbf{f}_t\|_{L^2(L^2)}^2 + \frac{\epsilon}{2} \|\mathbf{u}_h\|_{L^2(L^2)}^2 \right). \end{aligned}$$

Now using the above, lemma 5.5.1, the Cauchy-Schwarz and Young's inequality

ties, choosing ϵ sufficiently small, and noting (5.16), we arrive at

$$\begin{aligned} \|\mathbf{u}_h^N\|_{1,\Omega}^2 + |p_h^N|_{J,\Omega}^2 + \|\mathbf{z}_h\|_{L^2(L^2)}^2 + \|p_h\|_{L^2(L^2)}^2 &\leq C \left(\|\mathbf{u}_h\|_{L^2(H^1)}^2 + \|p_h\|_{L^2(J)}^2 + \|\mathbf{f}^N\|_{0,\Omega}^2 \right. \\ &+ \|\mathbf{f}_t\|_{L^2(L^2)}^2 + \|\mathbf{u}_h^0\|_{0,\Omega}^2 + |p_h^0|_{J,\Omega}^2 + \|\mathbf{f}^1\|_{L^2(L^2)}^2 + \|\mathbf{f}\|_{L^2(L^2)}^2 + \|\mathbf{b}\|_{L^2(L^2)}^2 + \|g\|_{L^2(L^2)}^2 \left. \right). \end{aligned}$$

Using Lemma 5.5.2 and regularity to bound the third term and upwards on the righthand side we obtain

$$\|\mathbf{u}_h^N\|_{1,\Omega}^2 + |p_h^N|_{J,\Omega}^2 + \|\mathbf{z}_h\|_{L^2(L^2)}^2 + \|p_h\|_{L^2(L^2)}^2 \leq C \left(1 + \|\mathbf{u}_h\|_{L^2(H^1)}^2 + \|p_h\|_{L^2(J)}^2 \right).$$

Upon applying the Gronwall lemma to the above inequality we obtain the desired result.

□

5.5.2 Bound on the divergence of the fluid flux

In order to bound the divergence of the fluid flux we now define the bilinear form \mathcal{B}_h^n . We first show how we derive \mathcal{B}_h^n from the fully-discrete weak form (5.7), for which we know that a solution $(\mathbf{u}_h, \mathbf{z}_h, p_h)$ exists for test functions $(\mathbf{v}_h, \mathbf{w}_h, q_h) \in \mathcal{V}_h^X$. Adding (5.7a) and (5.7b), assuming $\mathbf{t}_N = 0$ on Γ_t , and

summing we have

$$\begin{aligned} \sum_{n=1}^N a(\mathbf{u}_h^n, \mathbf{v}_h) + \sum_{n=1}^N (\mathbf{k}^{-1} \mathbf{z}_h^n, \mathbf{w}_h) - \sum_{n=1}^N (p_h^n, \nabla \cdot \mathbf{v}_h) - \sum_{n=1}^N (p_h^n, \nabla \cdot \mathbf{w}_h) \\ = \sum_{n=1}^N (\mathbf{f}^n, \mathbf{v}_h) + \sum_{n=1}^N (\mathbf{b}^n, \mathbf{w}_h) \quad \forall (\mathbf{v}_h, \mathbf{w}_h, q_h) \in \mathcal{V}_h^X. \end{aligned} \quad (5.40)$$

For the purposes of this proof we now introduce initial conditions for the fluid flux and the pressure, $\mathbf{z}^0 \in H_{div}(\Omega)$ and $p^0 \in \mathcal{L}(\Omega)$ respectively. We also define their projections into their respective finite element spaces by $\mathbf{z}_h^0 := \pi_h^0 \mathbf{z}^0$ and $p_h^0 := \pi_h^0 p^0$.

Adding (5.7a) and (5.7b), and summing from 0 to $N - 1$, we have

$$\begin{aligned} \sum_{n=1}^N a(\mathbf{u}_h^{n-1}, \mathbf{v}_h) + \sum_{n=1}^N (\mathbf{k}^{-1} \mathbf{z}_h^{n-1}, \mathbf{w}_h) - \sum_{n=1}^N (p_h^{n-1}, \nabla \cdot \mathbf{v}_h) - \sum_{n=1}^N (p_h^{n-1}, \nabla \cdot \mathbf{w}_h) \\ = \sum_{n=1}^N (\mathbf{f}^{n-1}, \mathbf{v}_h) + \sum_{n=1}^N (\mathbf{b}^{n-1}, \mathbf{w}_h) \quad \forall (\mathbf{v}_h, \mathbf{w}_h, q_h) \in \mathcal{V}_h^X. \end{aligned} \quad (5.41)$$

Taking (5.7c), multiplying by Δt , and summing we have

$$\begin{aligned} \sum_{n=1}^N \Delta t (\nabla \cdot \mathbf{u}_{\delta t, h}^n, q_h) + \sum_{n=1}^N \Delta t (\nabla \cdot \mathbf{z}_h^n, q_h) + \sum_{n=1}^N \Delta t J(p_{\delta t, h}^n, q_h) \\ = \sum_{n=1}^N \Delta t (g^n, q_h) \quad \forall (\mathbf{v}_h, \mathbf{w}_h, q_h) \in \mathcal{V}_h^X. \end{aligned} \quad (5.42)$$

Now adding (5.40) and (5.42), and subtracting (5.41) we get

$$\begin{aligned} & \sum_{n=1}^N \Delta t \mathcal{B}_h^n[(\mathbf{u}_h, \mathbf{z}_h, p_h), (\mathbf{v}_h, \mathbf{w}_h, q_h)] \\ &= \sum_{n=1}^N \Delta t(\mathbf{f}_{\Delta t}^n, \mathbf{v}_h) + \sum_{n=1}^N \Delta t(\mathbf{b}_{\Delta t}^n, \mathbf{w}_h) + \sum_{n=1}^N \Delta t(g^n, q_h) \quad \forall (\mathbf{v}_h, \mathbf{w}_h, q_h) \in \mathcal{V}_h^X, \end{aligned}$$

where

$$\begin{aligned} \mathcal{B}_h^n[(\mathbf{u}_h, \mathbf{z}_h, p_h), (\mathbf{v}_h, \mathbf{w}_h, q_h)] &= a(\mathbf{u}_{\delta t, h}^n, \mathbf{v}_h) + (\mathbf{k}^{-1} \mathbf{z}_{\delta t, h}^n, \mathbf{w}_h) \\ &- (p_{\delta t, h}^n, \nabla \cdot \mathbf{v}_h) - (p_{\delta t, h}^n, \nabla \cdot \mathbf{w}_h) + (\nabla \cdot \mathbf{u}_{\delta t, h}^n, q_h) + (\nabla \cdot \mathbf{z}_h^n, q_h) + J(p_{\delta t, h}^n, q_h). \end{aligned} \tag{5.43}$$

With these preliminaries, we may now bound \mathcal{B}_h^n from below.

Lemma 5.5.3. *For all $\beta > \beta^* > 0$, $(\mathbf{u}_h, \mathbf{z}_h, p_h)$ satisfies*

$$\begin{aligned} & \sum_{n=1}^N \Delta t \mathcal{B}_h^n[(\mathbf{u}_h, \mathbf{z}_h, p_h), (\beta \mathbf{u}_{\delta t, h}^n + \pi_h^1 v_p, \beta \mathbf{z}_h^n, \beta p_{\delta t, h}^n + \nabla \cdot \mathbf{z}_h^n)] + \|\mathbf{z}_h^0\|_{0, \Omega}^2 \geq \\ & C \left(\|\mathbf{u}_{\delta t, h}\|_{L^2(H^1)}^2 + \|\mathbf{z}_h^N\|_{0, \Omega}^2 + \|p_{\delta t, h}\|_{L^2(L^2)}^2 + \|p_{\delta t, h}\|_{L^2(J)}^2 + \|\nabla \cdot \mathbf{z}_h\|_{L^2(L^2)}^2 \right). \end{aligned}$$

Proof. For $n = 1, 2, \dots, N$ we choose $(\mathbf{v}_h, \mathbf{w}_h, q_h) = (\beta \mathbf{u}_{\delta t, h}^n + \pi_h^1 \mathbf{v}_{p_h^n}, \beta \mathbf{z}_h^n, \beta p_{\delta t, h}^n +$

$\nabla \cdot \mathbf{z}_h^n)$ in (5.43)

$$\begin{aligned}
& \sum_{n=1}^N \Delta t \mathcal{B}_h^n[(\mathbf{u}_h, \mathbf{z}_h, p_h), (\beta \mathbf{u}_{\delta t, h}^n + \pi_h^1 \mathbf{v}_p, \beta \mathbf{z}_h^n, \beta p_{\delta t, h}^n + \nabla \cdot \mathbf{z}_h^n)] \\
&= \sum_{n=1}^N \Delta t a(\mathbf{u}_{\delta t, h}^n, \beta \mathbf{u}_{\delta t, h}^n) + \sum_{n=1}^N \Delta t \mathbf{k}^{-1}(\mathbf{z}_{\delta t, h}^n, \beta \mathbf{z}_h^n) + \sum_{n=1}^N \Delta t (\nabla \cdot \mathbf{z}_h^n, \nabla \cdot \mathbf{z}_h^n) \\
&+ \sum_{n=1}^N \Delta t (\mathbf{u}_{\delta t, h}^n, \nabla \cdot \mathbf{z}_h^n) + \sum_{n=1}^N \Delta t J(p_{\delta t, h}^n, \nabla \cdot \mathbf{z}_h^n) + \sum_{n=1}^N \Delta t J(p_{\delta t, h}^n, \beta p_{\delta t, h}^n) \\
&+ \sum_{n=1}^N \Delta t a(\mathbf{u}_{\delta t, h}^n, \pi_h^1 \mathbf{v}_p) - \sum_{n=1}^N \Delta t (p_{\delta t, h}^n, \nabla \cdot \pi_h^1 \mathbf{v}_p). \quad (5.44)
\end{aligned}$$

For all $\epsilon > 0$ using (5.3), (5.4), the Cauchy-Schwarz, Young's and Poincaré inequalities, (5.11) and (5.10) on $\nabla \cdot \mathbf{z}_h^n$, and an approach similar to step 2 in the proof of Theorem 5.4.1 for the final two terms on the righthand side, we obtain

$$\begin{aligned}
& \sum_{n=1}^N \Delta t \mathcal{B}_h^n[(\mathbf{u}_h, \mathbf{z}_h, p_h), (\beta \mathbf{u}_{\delta t, h}^n + \pi_h^1 \mathbf{v}_p, \beta \mathbf{z}_h^n, \beta p_{\delta t, h}^n + \nabla \cdot \mathbf{z}_h^n)] \\
&\geq \left(\beta C_k - \frac{C_p + C_c}{2\epsilon} \right) \|\mathbf{u}_{\delta t, h}\|_{L^2(H^1)}^2 + \frac{\beta \lambda_{max}^{-1}}{2} \|\mathbf{z}_h^N\|_{0,\Omega}^2 + \left(\beta - \frac{3}{4\epsilon} \right) \|p_{\delta t, h}\|_{L^2(J)}^2 \\
&+ (1 - \epsilon(1 + c_z)) \|\nabla \cdot \mathbf{z}_h\|_{L^2(L^2)}^2 - \frac{\beta \lambda_{min}^{-1}}{2} \|\mathbf{z}_h^0\|_{0,\Omega}^2 + (1 - C\epsilon) \|p_{\delta t, h}\|_{L^2(L^2)}^2. \quad (5.45)
\end{aligned}$$

Finally choosing ϵ sufficiently small and $\beta \geq \max \left[\frac{C_p}{2C_k\epsilon}, \frac{3}{4\epsilon} \right]$ completes the proof.

□

The following Lemma shows the divergence control of the fluid flow.

Lemma 5.5.4. \mathbf{z}_h obtained from (5.43) satisfies

$$\|\nabla \cdot \mathbf{z}_h\|_{L^2(L^2)}^2 \leq C.$$

Proof. For $n = 1, 2, \dots, N$ we choose $(\mathbf{v}_h, \mathbf{w}_h, q_h) = (\beta \mathbf{u}_{\delta t, h}^n + \pi_h^1 \mathbf{v}_{p_h^n}, \beta \mathbf{z}_h^n, \beta p_{\delta t, h}^n + \nabla \cdot \mathbf{z}_h^n)$ in (5.43) yielding

$$\begin{aligned} & \sum_{n=1}^N \Delta t \mathcal{B}_h^n[(\mathbf{u}_h^n, \mathbf{z}_h^n, p_h^n), (\beta \mathbf{u}_{\delta t, h}^n + \pi_h^1 \mathbf{v}_{p_h^n}, \mathbf{z}_h^n, \beta p_{\delta t, h}^n + \nabla \cdot \mathbf{z}_h^n)] \\ &= \sum_{n=1}^N \Delta t (\mathbf{f}_{\Delta t}^n, \beta \mathbf{u}_{\delta t, h}^n + \pi_h^1 \mathbf{v}_{p_h^n}) + \sum_{n=1}^N \Delta t (\mathbf{b}_{\Delta t}^n, \beta \mathbf{z}_h^n) + \sum_{n=1}^N \Delta t (g^n, \beta p_{\delta t, h}^n + \nabla \cdot \mathbf{z}_h^n). \end{aligned}$$

Using lemma 5.5.3, the Cauchy-Schwarz and Young's inequalities, and (5.16), along with ideas already presented in the proof of lemma 5.5.2

$$\begin{aligned} & \|\mathbf{u}_{\delta t, h}\|_{L^2(H^1)}^2 + \|p_{\delta t, h}\|_{L^2(L^2)}^2 + \|p_{\delta t, h}\|_{L^2(J)}^2 + \|\mathbf{z}_h^N\|_{0, \Omega}^2 + \|\nabla \cdot \mathbf{z}_h\|_{L^2(L^2)}^2 \\ & \leq C \left(\|\mathbf{f}_t\|_{L^2(L^2)}^2 + \|\mathbf{b}_t\|_{L^2(L^2)}^2 + \|p_h\|_{L^2(L^2)}^2 + \|\mathbf{z}_h\|_{L^2(L^2)}^2 + \|g\|_{L^2(L^2)}^2 \right). \end{aligned}$$

Finally, using Lemma 5.5.2 to bound $\|p_h\|_{L^2(L^2)}$, applying a Gronwall lemma, and using regularity, we obtain the desired result.

□

5.5.3 The energy estimate

Theorem 5.5.5. *The solution to the fully-discrete problem (5.7) satisfies the energy estimate*

$$\|\mathbf{u}_h\|_{L^\infty(H^1)}^2 + \|p_h\|_{L^\infty(J)}^2 + \|\mathbf{z}_h\|_{L^2(L^2)}^2 + \|p_h\|_{L^2(L^2)}^2 + \|\nabla \cdot \mathbf{z}_h\|_{L^2(L^2)}^2 \leq C.$$

Proof. The proof follows from combining lemma 5.5.2 and lemma 5.5.4, and noting that these lemmas hold for all time steps $n = 0, 1, \dots, N$. This then gives the desired discrete in time L^∞ bounds. \square

Remark 5.5.1. *Having proven Theorem 5.5.5, it is now a standard calculation to show that the discrete Galerkin approximation converges weakly, as $\Delta t, h \rightarrow 0$, to the continuous problem with respect to continuous versions of the norms of the energy estimate in Theorem 5.5.5. This in turn shows that the continuous variational problem is well-posed. Due to the linearity of the variational form and noting that $|\mathbf{v}|_{J,\Omega} \rightarrow 0$ as $h \rightarrow 0$, these calculations are straight forward and closely follow the existence and uniqueness proofs presented in [110] and [11] for the linear two-field Biot problem and a nonlinear Biot problem, respectively.*

5.6 A-priori error analysis

Lemma 5.6.1 provides a Galerkin orthogonality result obtained by comparing continuous and discrete weak forms, which is the corner stone of the error

analysis. Lemma 5.3.1 is a standard approximation result for projections. Lemma 5.6.2 bounds the auxiliary errors for displacement, flux and pressure in the appropriate norms and Lemma 5.6.3 bounds the auxiliary error for the divergence of the flux. Since Lemmas 5.6.2 and 5.6.3 bound the auxiliary errors at the same order as the projection errors, combining projection and auxiliary errors in Theorem 5.6.4 provides an optimal error estimate.

We define the finite element error functions

$$\mathbf{e}_u := \mathbf{u} - \mathbf{u}_h, \quad \mathbf{e}_z := \mathbf{z} - \mathbf{z}_h, \quad e_p := p - p_h.$$

We introduce the following projection errors:

$$\boldsymbol{\eta}_u := \mathbf{u} - \pi_h^1 \mathbf{u}, \quad \boldsymbol{\eta}_z := \mathbf{z} - \pi_h^1 \mathbf{z}, \quad \eta_p := p - \pi_h^0 p,$$

where we have assumed $\mathbf{z}(t_n, \cdot) \in (H^1(\Omega))^d$.

Auxiliary errors:

$$\boldsymbol{\theta}_u^n(\cdot) := \pi_h^1 \mathbf{u}(t_n, \cdot) - \mathbf{u}_h^n(\cdot), \quad \boldsymbol{\theta}_z^n(\cdot) := \pi_h^1 \mathbf{z}(t_n, \cdot) - \mathbf{z}_h^n(\cdot), \quad \theta_p^n(\cdot) := \pi_h^0 p(t_n, \cdot) - p_h^n(\cdot), \quad (5.46)$$

and time-discretization errors:

$$\boldsymbol{\rho}_u^n(\cdot) := \frac{\mathbf{u}(t_n, \cdot) - \mathbf{u}(t_{n-1}, \cdot)}{\Delta t} - \frac{\partial \mathbf{u}(t_n, \cdot)}{\partial t}, \quad \rho_p^n := \frac{p(t_n, \cdot) - p(t_{n-1}, \cdot)}{\Delta t} - \frac{\partial p(t_n, \cdot)}{\partial t}. \quad (5.47)$$

5.6.1 Galerkin orthogonality

We now give a Galerkin orthogonality type argument for analysing the difference between the fully-discrete approximation and the true solution. For this we introduce the continuous counterpart of the fully-discrete combined weak form (5.32) given by

$$B^n[(\mathbf{u}, \mathbf{z}, p), (\mathbf{v}, \mathbf{w}, q)] = (\mathbf{f}(t_n, \cdot), \mathbf{v}) + (\mathbf{b}(t_n, \cdot), \mathbf{w}) + (g(t_n, \cdot), q) \quad \forall (\mathbf{v}, \mathbf{w}, q) \in \mathcal{V}^X,$$

where

$$\begin{aligned} B^n[(\mathbf{u}, \mathbf{z}, p), (\mathbf{v}, \mathbf{w}, q)] &= a(\mathbf{u}(t_n, \cdot), \mathbf{v}) + \mathbf{k}^{-1}(\mathbf{z}(t_n, \cdot), \mathbf{w}) - (p(t_n, \cdot), \nabla \cdot \mathbf{v}) \\ &\quad - (p(t_n, \cdot), \nabla \cdot \mathbf{w}) + (\nabla \cdot \mathbf{u}_t(t_n, \cdot), q) + (\nabla \cdot \mathbf{z}(t_n, \cdot), q). \end{aligned}$$

Lemma 5.6.1. *Assuming $(\mathbf{u}(t_n, \cdot), \mathbf{z}(t_n, \cdot), p(t_n, \cdot)) \in (H^1(\Omega))^d \times H_{div}(\Omega) \times (H^1(\Omega) \cap \mathcal{L}(\Omega))$*

$$B_{\Delta t, h}^n[(\mathbf{e}_u, \mathbf{e}_z, e_p), (\mathbf{v}_h, \mathbf{w}_h, q_h)] = (\nabla \cdot \boldsymbol{\rho}_u^n, q_h) + J(\rho_p^n, q_h) \quad \forall (\mathbf{v}_h, \mathbf{w}_h, q_h) \in \mathcal{V}_h^X.$$

Proof. Subtracting the discrete weak form (5.32) from the continuous weak form (5.6.1), we obtain

$$B^n[(\mathbf{u}, \mathbf{z}, p), (\mathbf{v}_h, \mathbf{w}_h, q_h)] - B_{\Delta t, h}^n[(\mathbf{u}_h, \mathbf{z}_h, p_h), (\mathbf{v}_h, \mathbf{w}_h, q_h)] = 0, \quad \forall (\mathbf{v}_h, \mathbf{w}_h, q_h) \in \mathcal{V}_h^X.$$

Now add $J(p_t(t_n, \cdot), q) = 0$ to the left hand side, see (5.12). Finally add

$(\nabla \cdot (\mathbf{u}_{\delta t}(t_n, \cdot) - \mathbf{u}_t(t_n, \cdot)), q) + J(p_{\delta t}(t_n, \cdot) - p_t(t_n, \cdot), q)$ to the left and the righthand side to obtain the desired result. \square

5.6.2 Auxiliary error estimates

Lemma 5.6.2.

$$\|[\boldsymbol{\theta}_u, \boldsymbol{\theta}_z, \theta_p]\|_B^2 + \|\theta_p\|_{L^\infty(J)}^2 \leq C(T)(h^2 + \Delta t^2). \quad (5.48)$$

Proof. Using Lemma 5.6.1 and choosing $\mathbf{v}_h^n = \boldsymbol{\theta}_{\delta t, u}^n + \pi_h^1 \mathbf{v}_{p_h^n}$, $\mathbf{w}_h^n = \boldsymbol{\theta}_z^n$, $q_h^n = \theta_p^n$, we get

$$\begin{aligned} & B_{\Delta t, h}^n[(\boldsymbol{\theta}_u^n + \boldsymbol{\eta}_u^n, \boldsymbol{\theta}_z^n + \boldsymbol{\eta}_z^n, \theta_p^n + \eta_p^n), (\boldsymbol{\theta}_{\delta t, u}^n + \pi_h^1 \mathbf{v}_{p_h^n}, \boldsymbol{\theta}_z^n, \theta_p^n)] \\ &= (\nabla \cdot \boldsymbol{\rho}_u^n, \theta_p^n) + J(\rho_p^n, \theta_p^n). \end{aligned}$$

Rearranging gives

$$\begin{aligned} & B_{\Delta t, h}^n[(\boldsymbol{\theta}_u^n, \boldsymbol{\theta}_z^n, \theta_p^n), (\boldsymbol{\theta}_{\delta t, u}^n + \pi_h^1 \mathbf{v}_{p_h^n}, \boldsymbol{\theta}_z^n, \theta_p^n)] \\ &= (\nabla \cdot \boldsymbol{\rho}_u^n, \theta_p^n) + J(\rho_p^n, \theta_p^n) - B_{\Delta t, h}^n[(\boldsymbol{\eta}_u^n, \boldsymbol{\eta}_z^n, \eta_p^n), (\boldsymbol{\theta}_{\delta t, u}^n + \pi_h^1 \mathbf{v}_{p_h^n}, \boldsymbol{\theta}_z^n, \theta_p^n)]. \end{aligned}$$

Expanding the righthand side, noting that $(\eta_p^n, \nabla \cdot (\boldsymbol{\theta}_{\delta t, u}^n + \pi_h^1 \mathbf{v}_p)) = 0$, $(\eta_p^n, \nabla \cdot \boldsymbol{\theta}_z^n) = 0$, multiplying both sides by Δt and summing gives

$$\sum_{n=1}^N \Delta t B_{\Delta t, h}^n[(\boldsymbol{\theta}_u^n, \boldsymbol{\theta}_z^n, \theta_p^n), (\boldsymbol{\theta}_{\delta t, u}^n + \pi_h^1 \mathbf{v}_{p_h^n}, \boldsymbol{\theta}_z^n, \theta_p^n)] = \sum_{i=1}^7 \Phi_i,$$

where

$$\begin{aligned}
\Phi_1 &:= - \sum_{n=1}^N \Delta t a(\boldsymbol{\eta}_{\mathbf{u}}^n, \boldsymbol{\theta}_{\delta t, \mathbf{u}}^n), & \Phi_2 &:= - \sum_{n=1}^N \Delta t (\mathbf{k}^{-1}(\boldsymbol{\eta}_{\mathbf{z}}^n, \boldsymbol{\theta}_{\mathbf{z}}^n)), \\
\Phi_3 &:= - \sum_{n=1}^N \Delta t a(\boldsymbol{\eta}_{\mathbf{u}}^n, \pi_h^1 \mathbf{v}_p), & \Phi_4 &:= - \sum_{n=1}^N \Delta t J(\eta_{\delta t, p}^n, \theta_p^n), \\
\Phi_5 &:= \sum_{n=1}^N \Delta t (\nabla \cdot \boldsymbol{\rho}_{\mathbf{u}}^n, \theta_p^n), & \Phi_6 &:= \sum_{n=1}^N \Delta t J(\rho_p^n, \theta_p^n), \\
\Phi_7 &:= - \sum_{n=1}^N \Delta t (\theta_p^n, \nabla \cdot (\boldsymbol{\eta}_{\delta t, \mathbf{u}}^n + \boldsymbol{\eta}_{\mathbf{z}}^n)).
\end{aligned}$$

We now individually consider the terms on the right hand side of (5.49):

To bound the first quantity, we use (5.21), Lemma 5.3.1, the triangle, Cauchy-Schwarz and Young's inequalities, $\boldsymbol{\theta}_{\mathbf{u}}^0 = 0$, and (5.2),

$$\begin{aligned}
\Phi_1 &= - \sum_{n=1}^N a(\boldsymbol{\eta}_{\mathbf{u}}^n, \boldsymbol{\theta}_{\mathbf{u}}^n - \boldsymbol{\theta}_{\mathbf{u}}^{n-1}) \\
&= -a(\boldsymbol{\eta}_{\mathbf{u}}^N, \boldsymbol{\theta}_{\mathbf{u}}^N) + \sum_{n=1}^N a(\boldsymbol{\eta}_{\mathbf{u}}^n - \boldsymbol{\eta}_{\mathbf{u}}^{n-1}, \boldsymbol{\theta}_{\mathbf{u}}^{n-1}) \\
&= -a(\boldsymbol{\eta}_{\mathbf{u}}^N, \boldsymbol{\theta}_{\mathbf{u}}^N) + \Delta t \sum_{n=1}^N a \left((I - \pi_h^1) \left(\boldsymbol{\rho}_{\mathbf{u}}^n + \frac{\partial \mathbf{u}(t_n, \cdot)}{\partial t} \right), \boldsymbol{\theta}_{\mathbf{u}}^{n-1} \right) \\
&\leq \epsilon C \|\boldsymbol{\theta}_{\mathbf{u}}^N\|_{1,\Omega}^2 + \frac{Ch^2}{\epsilon} \|\mathbf{u}^N\|_{2,\Omega}^2 + \epsilon C \|\boldsymbol{\theta}_{\mathbf{u}}\|_{L^2(H^1)}^2 + \frac{Ch^2}{2\epsilon} \|\mathbf{u}_t\|_{L^2(H^2)}^2 + \frac{C\Delta t^2}{2\epsilon} \|\mathbf{u}_{tt}\|_{L^2(H^1)}^2.
\end{aligned} \tag{5.49}$$

Next, using (5.4), Young's inequality, (5.16) and Lemma 5.3.1,

$$\Phi_2 \leq \frac{\epsilon}{2} \|\boldsymbol{\theta}_z\|_{L^2(L^2)}^2 + \frac{\lambda_{min}^{-2} h^2}{2\epsilon} \|z\|_{L^2(H^1)}^2.$$

Using (5.2), Young's inequality and Lemma 5.3.1,

$$\Phi_3 \leq \frac{\epsilon}{2} \|\pi_h^1 \mathbf{v}_{p_h^n}\|_{L^2(H^1)}^2 + \frac{C}{2\epsilon} \|\boldsymbol{\eta}_u\|_{L^2(H^1)}^2 \leq \frac{\epsilon \hat{c}^2}{2} \|\theta_p\|_{L^2(L^2)}^2 + \frac{Ch^2}{2\epsilon} \|u\|_{L^2(H^2)}^2.$$

The bound on Φ_4 is obtained using a similar argument to the bound on Φ_1 ,

$$\Phi_4 \leq \epsilon \|\theta_p\|_{L^2(J)}^2 + \frac{h^2}{2\epsilon} \|p_t\|_{L^2(H^1)}^2 + \frac{\Delta t^2}{2\epsilon} \|p_{tt}\|_{L^2(H^1)}^2.$$

Using the Cauchy-Schwarz and Young's inequalities and lemma 5.3.1,

$$\Phi_5 \leq \frac{\epsilon}{2} \|\theta_p\|_{L^2(L^2)}^2 + \frac{\Delta t^2}{2\epsilon} \|u_{tt}\|_{L^2(L^2)}^2 \text{ and } \Phi_6 \leq \frac{\epsilon}{2} \|\theta_p\|_{L^2(J)}^2 + \frac{\Delta t^2}{2\epsilon} \|p_{tt}\|_{L^2(L^2)}^2.$$

Finally, using the Cauchy-Schwarz and Young's inequalities, and a similar argument to the bound on Φ_1 ,

$$\Phi_7 \leq \frac{3\epsilon}{2} \|\theta_p\|_{L^2(L^2)}^2 + \frac{h^2}{2\epsilon} \|u_t\|_{L^2(H^2)}^2 + \frac{\Delta t^2}{2\epsilon} \|u_{tt}\|_{L^2(H^1)}^2 + \frac{h^2}{2\epsilon} \|z\|_{L^2(H^2)}^2.$$

Combining these bounds with an application of coercivity Lemma 5.5.1 to (5.49), noting the assumed regularity of the continuous solution and choosing

ϵ sufficiently small, gives

$$\|\boldsymbol{\theta}_u^N\|_{1,\Omega}^2 + |\theta_p^N|_{J,\Omega}^2 + \|\boldsymbol{\theta}_z\|_{L^2(L^2)}^2 + \|\theta_p\|_{L^2(L^2)}^2 \leq C \left(\|\boldsymbol{\theta}_u\|_{L^2(H^1)}^2 + \|\theta_p\|_{L^2(J)}^2 + h^2 + \Delta t^2 \right). \quad (5.50)$$

An application of Gronwall's lemma gives

$$\|\boldsymbol{\theta}_u^N\|_{1,\Omega}^2 + |\theta_p^N|_{J,\Omega}^2 + \|\boldsymbol{\theta}_z\|_{L^2(L^2)}^2 + \|\theta_p\|_{L^2(L^2)}^2 \leq C(T) (h^2 + \Delta t^2).$$

Because the above holds for all time steps $n = 0, 1, \dots, N$, we can get the desired L^∞ bounds to complete the proof of the theorem. \square

We now present an a-priori auxiliary error estimate of the fluid flux, in its natural $Hdiv$ norm.

Lemma 5.6.3. *Assuming $\mathbf{u} \in H^2(0, T; (H^1(\Omega))^d) \cap H^1(0, T; (H^2(\Omega))^d)$, $\mathbf{z} \in L^2(0, T; (H^2(\Omega))^d)$ and $p \in H^2(0, T; J \cap \mathcal{L}(\Omega)) \cap H^1(0, T; H^1(\Omega))$, then the finite element solution (5.7) satisfies the auxillary error estimate*

$$\|\nabla \cdot \boldsymbol{\theta}_z\|_{L^2(L^2)}^2 \leq C(T)(h^2 + \Delta t^2). \quad (5.51)$$

Proof. Similarly to the approach taken in obtaining (5.43) we may easily obtain the following identity

$$\sum_{n=1}^N \Delta t \mathcal{B}_h^n[(\boldsymbol{\theta}_u^n, \boldsymbol{\theta}_z^n, \theta_p^n), (\beta \boldsymbol{\theta}_{\delta t, u}^n + \pi_h^1 \mathbf{v}_{\theta_{\delta t, p}^n}, \beta \boldsymbol{\theta}_z^n, \beta \theta_{\delta t, p}^n + \nabla \cdot \boldsymbol{\theta}_z^n)] = \sum_{i=1}^6 \Psi_i,$$

where

$$\begin{aligned}\Psi_1 &= -\sum_{n=1}^N \Delta t a(\boldsymbol{\eta}_{\delta t, \mathbf{u}}^n, \beta \boldsymbol{\theta}_{\delta t, \mathbf{u}}^n + \pi_h^1 \mathbf{v}_{\theta_{\delta t, p}^n}), \quad \Psi_2 = -\sum_{n=1}^N \Delta t (\nabla \cdot (\boldsymbol{\eta}_{\delta t, \mathbf{u}}^n + \boldsymbol{\eta}_{\mathbf{z}}^n), \nabla \cdot \boldsymbol{\theta}_{\mathbf{z}}^n + \beta \theta_{\delta t, p}^n), \\ \Psi_3 &= \sum_{n=1}^N \Delta t J(\eta_{\delta t, p}^n, \beta \theta_{\delta t, p}^n + \nabla \cdot \boldsymbol{\theta}_{\mathbf{z}}^n), \quad \Psi_4 = -\sum_{n=1}^N \Delta t (\mathbf{k}^{-1}(\boldsymbol{\eta}_{\delta t, \mathbf{z}}^n, \beta \boldsymbol{\theta}_{\mathbf{z}}^n)), \\ \Psi_5 &= \sum_{n=1}^N \Delta t J(\rho_p^n, \beta \theta_{\delta t, p}^n + \nabla \cdot \boldsymbol{\theta}_{\mathbf{z}}^n), \quad \Psi_6 = \sum_{n=1}^N \Delta t (\nabla \cdot \boldsymbol{\rho}_{\mathbf{u}}^n, \beta \theta_{\delta t, p}^n + \nabla \cdot \boldsymbol{\theta}_{\mathbf{z}}^n).\end{aligned}$$

We now bound the terms on the right hand side of (5.52) using machinery developed during the previous proof:

$$\begin{aligned}\Psi_1 &\leq \frac{C\epsilon}{2} \|\boldsymbol{\theta}_{\delta t, \mathbf{u}}\|_{L^2(H^1)}^2 + \frac{\hat{c}^2\epsilon}{2} \|\theta_{\delta t, p}\|_{L^2(L^2)}^2 + \frac{Ch^2}{2\epsilon} \|\mathbf{u}_t\|_{L^2(H^2)}^2 \\ &\quad + \frac{C}{2\epsilon} \Delta t^2 \|\mathbf{u}_{tt}\|_{L^2(H^1)}^2,\end{aligned}\tag{5.52}$$

$$\begin{aligned}\Psi_2 &\leq \epsilon \|\nabla \cdot \boldsymbol{\theta}_{\mathbf{z}}\|_{L^2(L^2)}^2 + \epsilon \|\theta_{\delta t, p}\|_{L^2(L^2)}^2 + \frac{Ch^2}{2\epsilon} \left(\|\mathbf{u}_t\|_{L^2(H^2)}^2 + \|\mathbf{z}\|_{L^2(H^2)}^2 \right) \\ &\quad + \frac{C}{2\epsilon} \Delta t^2 \|\mathbf{u}_{tt}\|_{L^2(H^1)}^2,\end{aligned}\tag{5.53}$$

$$\Psi_3 \leq \epsilon C \|\nabla \cdot \boldsymbol{\theta}_{\mathbf{z}}\|_{L^2(L^2)}^2 + \epsilon \|\theta_{\delta t, p}\|_{L^2(J)}^2 + \frac{Ch^2}{2\epsilon} \|p_t\|_{L^2(H^1)}^2\tag{5.54}$$

$$+ \frac{C}{2\epsilon} \Delta t^2 \|p_{tt}\|_{L^2(J)}^2,\tag{5.55}$$

$$\Psi_4 \leq \epsilon \|\boldsymbol{\theta}_{\mathbf{z}}\|_{L^2(L^2)}^2 + \frac{Ch^2}{2\epsilon} \|\mathbf{z}_t\|_{L^2(H^1)}^2 + \frac{C}{2\epsilon} \Delta t^2 \|\mathbf{z}_{tt}\|_{L^2(L^2)}^2,\tag{5.56}$$

$$\Psi_5 \leq \epsilon \|\theta_{\delta t, p}\|_{L^2(J)}^2 + \epsilon C \|\nabla \cdot \boldsymbol{\theta}_{\mathbf{z}}\|_{L^2(L^2)}^2 + \frac{C\Delta t^2}{2\epsilon} \|p_{tt}\|_{L^2(J)}^2,\tag{5.57}$$

$$\Psi_6 \leq \epsilon \|\theta_{\delta t, p}\|_{L^2(L^2)}^2 + \epsilon \|\nabla \cdot \boldsymbol{\theta}_{\mathbf{z}}\|_{L^2(L^2)}^2 + \frac{C}{2\epsilon} \Delta t^2 \|\mathbf{u}_{tt}\|_{L^2(H^1)}^2.\tag{5.58}$$

We can now combine the individual bounds (5.52), (5.53), (5.55), (5.56),

(5.57), and (5.58), with the coercivity result Lemma 5.5.3, choose β sufficiently large, use the assumption $\boldsymbol{\theta}_z^0 = 0$, the assumed regularity of \mathbf{u}, \mathbf{z} and p , and choose ϵ sufficiently small to obtain

$$\|\boldsymbol{\theta}_z^N\|_{0,\Omega}^2 + \|\nabla \cdot \boldsymbol{\theta}_z\|_{L^2(L^2)}^2 \leq C\|\boldsymbol{\theta}_z\|_{L^2(L^2)}^2 + C(h^2 + \Delta t^2).$$

Applying Gronwall's lemma, we get the desired result. \square

5.6.3 The a priori error estimate

Combining the previous lemmas we have the following.

Theorem 5.6.4. *Assuming $\mathbf{u} \in H^2(0, T; (L^2(\Omega))^d) \cap H^1(0, T; (H^2(\Omega))^d)$, $\mathbf{z} \in L^2(0, T; (H^1(\Omega))^d)$ and $p \in H^2(0, T; H^1(\Omega) \cap \mathcal{L}(\Omega))$, then the finite element solution (5.7) satisfies the error estimate*

$$\|\mathbf{e}_{\mathbf{u}}, \mathbf{e}_{\mathbf{z}}, e_p\|_B^2 \leq C(h^2 + \Delta t^2).$$

Assuming $\mathbf{u} \in H^2(0, T; (H^1(\Omega))^d) \cap H^1(0, T; (H^2(\Omega))^d)$, $\mathbf{z} \in L^2(0, T; (H^2(\Omega))^d)$ and $p \in H^2(0, T; J \cap \mathcal{L}(\Omega)) \cap H^1(0, T; H^1(\Omega))$, then the finite element solution (5.7) satisfies the error estimate

$$\|\mathbf{e}_{\mathbf{u}}, \mathbf{e}_{\mathbf{z}}, e_p\|_B^2 + \|\nabla \cdot \mathbf{e}_{\mathbf{z}}\|_{L^2(L^2)}^2 \leq C(h^2 + \Delta t^2).$$

Proof. We first write the errors as $\mathbf{e}_{\mathbf{u}}^n = \boldsymbol{\eta}_{\mathbf{u}}^n + \boldsymbol{\theta}_{\mathbf{u}}^n$, and similarly for the other variables. Using lemma 5.3.1 we can bound the projection errors, and using

lemma 5.6.2 and lemma 5.6.3 we can bound the auxillary errors to give the desired result. \square

5.7 Implementation

For the implementation we used the C++ library libmesh [54], and the multi-frontal direct solver mumps [4] to solve the resulting linear system. To solve the full Biot model problem (3.39), we need to solve the following linear system at each time step:

$$\begin{bmatrix} \mathbf{A} & 0 & \alpha \mathbf{B}^T \\ 0 & \mathbf{M} & \mathbf{B}^T \\ -\alpha \mathbf{B} & -\Delta t \mathbf{B} & c_0 \mathbf{Q} + \mathbf{J} \end{bmatrix} \begin{bmatrix} \mathbf{u}^n \\ \mathbf{z}^n \\ \mathbf{p}^n \end{bmatrix} = \begin{bmatrix} \mathbf{r} \\ \mathbf{s} \\ \Delta t \mathbf{g} - \mathbf{B} \mathbf{u}^{n-1} + c_0 \mathbf{Q} \mathbf{p}^{n-1} + \mathbf{J} \mathbf{p}^{n-1} \end{bmatrix},$$

where we have defined the following matrices and vectors:

$$\mathbf{A} = [\mathbf{a}_{ij}], \quad \mathbf{a}_{ij} = \int_{\Omega} 2\mu_s \nabla \phi_i : \nabla \phi_j + \lambda (\nabla \cdot \phi_i) (\nabla \cdot \phi_j),$$

$$\mathbf{M} = [\mathbf{m}_{ij}], \quad \mathbf{m}_{ij} = \int_{\Omega} k^{-1} \phi_i \cdot \phi_j,$$

$$\mathbf{B} = [\mathbf{b}_{ij}], \quad \mathbf{b}_{ij} = - \int_{\Omega} \psi_i \nabla \cdot \phi_j,$$

$$\mathbf{Q} = [\mathbf{q}_{ij}], \quad \mathbf{q}_{ij} = \int_{\Omega} \psi_i \cdot \psi_j,$$

$$\mathbf{J} = [\mathbf{j}_{ij}], \quad \mathbf{j}_{ij} = \delta \sum_K \int_{\partial K \setminus \partial \Omega} h_{\partial K}[\psi_i][\psi_j] \, ds,$$

$$\mathbf{r} = [\mathbf{r}_i], \quad \mathbf{r}_i = \int_{\Omega} \mathbf{f}_i \cdot \phi_i + \int_{\Gamma_t} \mathbf{t}_{Ni} \cdot \phi_i,$$

$$\mathbf{s} = [\mathbf{s}_i], \quad \mathbf{s}_i = \int_{\Omega} \mathbf{b}_i \cdot \phi_i - \int_{\Gamma_p} p_D \phi_i \cdot \mathbf{n},$$

$$\mathbf{g} = [\mathbf{g}_i], \quad \mathbf{g}_i = \int_{\Omega} g \psi_i.$$

Here ϕ_i are vector valued linear basis functions such that the displacement vector can be written as $\mathbf{u}^n = \sum_{i=1}^{n_u} \mathbf{u}_i^n \phi_i$, with $\sum_{i=1}^{n_u} \mathbf{u}_i^n \phi_i \in \mathbf{W}_h^E$. Similarly for the relative fluid vector we have $\mathbf{z}^n = \sum_{i=1}^{n_z} \mathbf{z}_i^n \phi_i$, with $\sum_{i=1}^{n_z} \mathbf{z}_i^n \phi_i \in \mathbf{W}_h^D$. The scalar valued constant basis functions ψ_i are used to approximate the pressure, such that $\mathbf{p}^n = \sum_{i=1}^{n_p} p_i^n \psi_i$, with $\sum_{i=1}^{n_p} p_i^n \psi_i \in Q_h$.

5.7.1 Algorithm to assemble the stabilization matrix

Let $K \in \mathcal{T}_h$ be an element and $\mathcal{D}(K)$ be the pressure degree of freedom associated with element K . We define $\mathcal{A}(K)$ to be the set of elements $L \in \mathcal{T}_h$ neighboring K .

Algorithm 1 Stabilization matrix \mathbf{J} assembly

```
for every  $K \in \mathcal{T}_h$  do
    for every  $L \in \mathcal{A}(K)$  do
        Calculate  $h_{\partial K}$ 
         $i \leftarrow \mathcal{D}(K)$ 
         $j \leftarrow \mathcal{D}(L)$ 
         $\mathbf{J}_{ii} \leftarrow \mathbf{J}_{ii} + (\delta h_{\partial K} \text{ in 2D}, \delta h_{\partial K}^{3/2} \text{ in 3D})$ 
         $\mathbf{J}_{ij} \leftarrow \mathbf{J}_{ij} - (\delta h_{\partial K} \text{ in 2D}, \delta h_{\partial K}^{3/2} \text{ in 3D})$ 
    end for
end for
```

5.8 Numerical Results

We first present convergence studies for both two- and three-dimensional test problems which illustrate the predicted convergence rates for the fully-discrete finite element method. We then apply our method to the popular 2D cantilever bracket problem and demonstrate that our stabilization techniques overcomes the spurious pressure oscillations that have been experienced by other methods. Finally, a 3D unconfined compression problem is presented that highlights the added mass effect of the method for different choices of the stabilization parameter δ .

5.8.1 2D test problem

Choosing $\lambda = \mu = \alpha = 1$, $c_0 = 0$ and $\mathbf{k} = \mathbf{I}$ in (5.1) we solve the problem

$$-2\nabla(\nabla \cdot \mathbf{u}) - \nabla^2 \mathbf{u} + \nabla p = \mathbf{f} \quad \text{in } \Omega, \quad (5.59\text{a})$$

$$\mathbf{z} + \nabla p = 0 \quad \text{in } \Omega, \quad (5.59\text{b})$$

$$\nabla \cdot (\mathbf{u}_t + \mathbf{z}) = g \quad \text{in } \Omega, \quad (5.59\text{c})$$

$$\mathbf{u}(t) = \mathbf{u}_D \quad \text{on } \Gamma_d, \quad (5.59\text{d})$$

$$\mathbf{z}(t) \cdot \mathbf{n} = q_D \quad \text{on } \Gamma_f, \quad (5.59\text{e})$$

$$\mathbf{u}(0, \mathbf{x}) = 0, \quad p(0, \mathbf{x}) = 0 \quad \mathbf{x} \in \Omega. \quad (5.59\text{f})$$

The domain, Ω , is the unit square and the source terms and boundary conditions are chosen so that the true solution is

$$\mathbf{u} = \begin{pmatrix} -\frac{1}{4\pi} \cos(2\pi x) \sin(2\pi y) \sin(2\pi t) \\ -\frac{1}{4\pi} \sin(2\pi x) \cos(2\pi y) \sin(2\pi t) \end{pmatrix}, \quad \mathbf{z} = \begin{pmatrix} -2\pi \cos(2\pi x) \sin(2\pi y) \sin(2\pi t) \\ -2\pi \sin(2\pi x) \cos(2\pi y) \sin(2\pi t) \end{pmatrix},$$

and $p = \sin(2\pi x) \sin(2\pi y) \sin(2\pi t)$, with $t \in [0, 0.25]$.

Choice of δ

The most appropriate choice of stabilization parameter δ is not known a priori. Small values of δ can result in spurious pressure solutions, as shown in Figure 5.1a for $\delta = 0.1$. Larger values of the stabilization parameter produce smooth pressure solution, as shown in Figure 5.1b for a value of $\delta = 1$. The

value of δ required to produce a stable solution depends on the geometry and material parameters of the particular problem under investigation, but is independent of any mesh parameters.

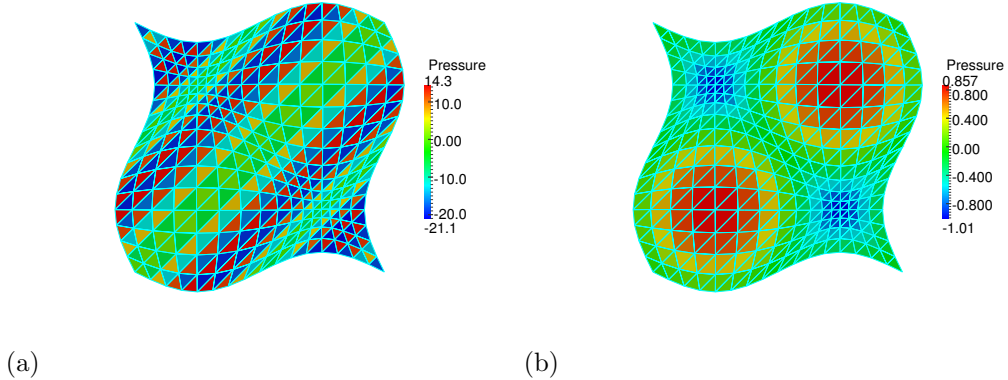


Figure 5.1: (a) Unstable pressure field, caused by not choosing the stabilization parameter δ large enough, with $\delta = 0.1$, at $t = 0.25$. (b) Stable pressure field, with $\delta = 1$ at $t = 0.25$.

2D convergence study

The convergence of the method with discretization parameters is illustrated in Figure 5.2a – 5.2e for $\delta = 1, 10, 100$. The convergence rates observed in the appropriate norms agree with the theoretically derived error estimates.

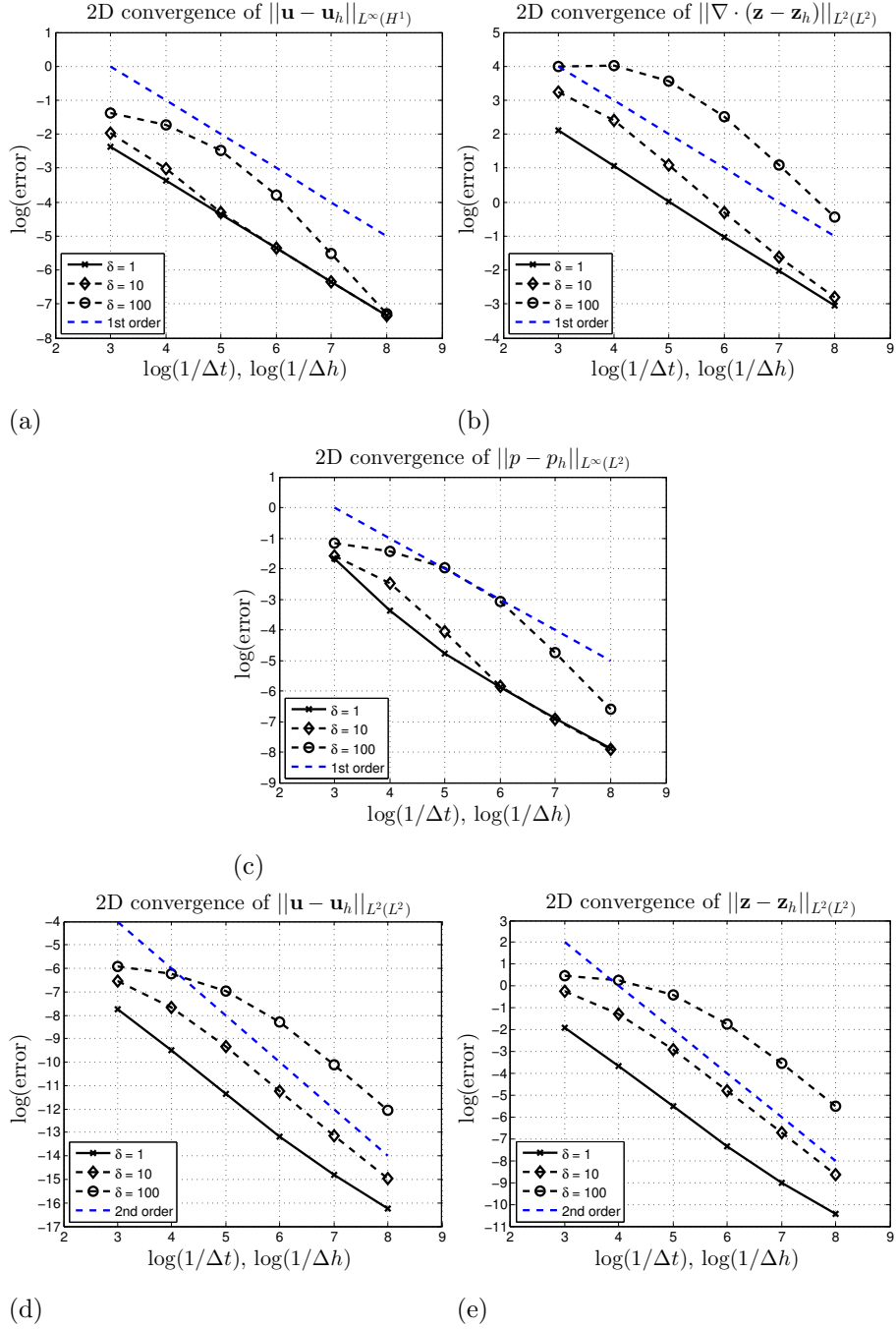


Figure 5.2: Convergence of the displacement, fluid flux, and pressure errors in their respective norms of the simplified poroelastic 2D test problem with different (stable) values for the stabilization parameter δ .

Alternative stabilization techniques

In Figure 5.3 we illustrate the convergence of the pressure error for three possible stabilization forms. As demonstrated in Section 5.8.1, the stabilization $J(p_{\delta t,h}, q_h)$ yields a stable solution and optimal convergence rate. A more naive approach, inserting the stabilization $J(p_h, q_h)$ results in the solution becoming unstable after the first refinement step. This is because the stabilization becomes relatively small as Δt decreases. To overcome this issue one could chose to scale the stabilization, and try $\frac{1}{\Delta t} J(p_h, q_h)$. Although this stabilization now stays stable during refinement, it does not converge at an optimal rate.

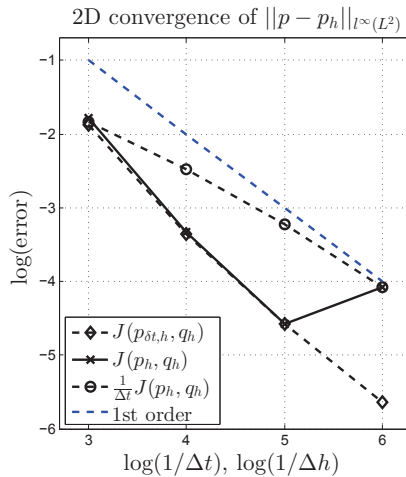


Figure 5.3: Convergence of the pressure error for three different stabilization forms, with $\delta = 1$.

5.8.2 3D test problem

Extending the test problem in Section 5.8.1 to the unit cube, we set

$$\mathbf{u} = \begin{pmatrix} -\frac{1}{6\pi} \cos(2\pi x) \sin(2\pi y) \sin(2\pi z) \sin(2\pi t) \\ -\frac{1}{6\pi} \sin(2\pi x) \cos(2\pi y) \sin(2\pi z) \sin(2\pi t) \\ -\frac{1}{6\pi} \sin(2\pi x) \sin(2\pi y) \cos(2\pi z) \sin(2\pi t) \end{pmatrix},$$

$$\mathbf{z} = \begin{pmatrix} -2\pi \cos(2\pi x) \sin(2\pi y) \sin(2\pi z) \sin(2\pi t) \\ -2\pi \sin(2\pi x) \cos(2\pi y) \sin(2\pi z) \sin(2\pi t) \\ -2\pi \sin(2\pi x) \sin(2\pi y) \cos(2\pi z) \sin(2\pi t) \end{pmatrix},$$

and

$$p = \sin(2\pi x) \sin(2\pi y) \sin(2\pi z) \sin(2\pi t).$$

The expected rates of convergence for each variable in the appropriate norm are illustrated in the numerical results presented in figure 5.4a – 5.4e for $\delta = 0.001, 0.01, 0.1$. The stabilization factor δ may be chosen to be very much smaller for 3D problems as compared to 2D problems and the effect of the stabilization term on the solution is negligible. This can be explained by the improved ratio of solid displacement and fluid flux nodes to pressure nodes in three dimensions, making the LBB condition easier to satisfy.

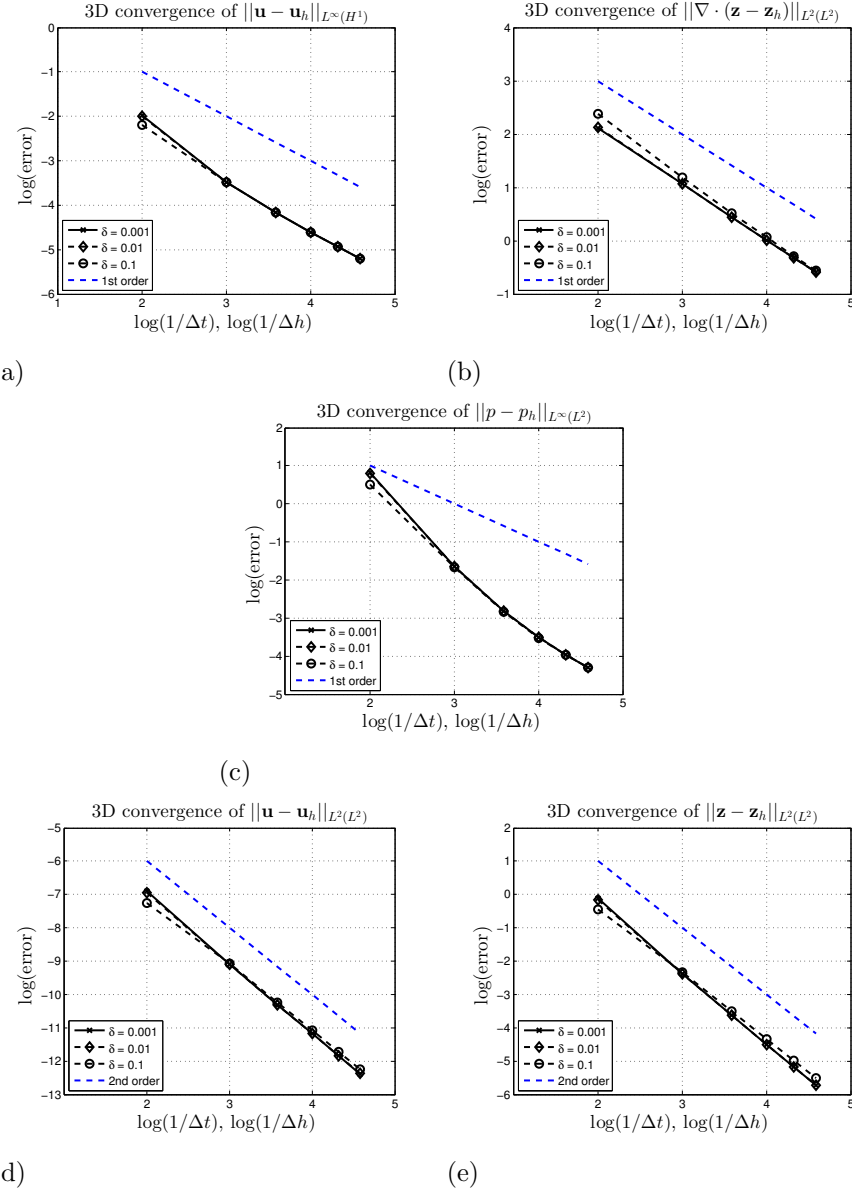


Figure 5.4: Convergence of the displacement, fluid flux, and pressure errors in their respective norms of the simplified poroelastic 3D test problem with different (stable) values for the stabilization parameter δ .

5.8.3 2D cantilever bracket problem

We consider the 2D cantilever bracket problem used in [81] to illustrate the problem of spurious pressure oscillation. This problem was also used in [68] and [107] to demonstrate their methods ability to overcome these spurious pressure oscillations. The cantilever bracket problem (shown in Figure 5.5a) is solved on a unit square $[0, 1]^2$. No-flow flux boundary conditions are applied along all sides, the deformation is fixed ($\mathbf{u} = 0$) along the left hand-side ($x = 0$), and a downward traction force, $\mathbf{t}_N \cdot \mathbf{n} = -1$, is applied along the top edge ($y = 1$). The right and bottom sides are traction-free. For this numerical experiment, we set $\Delta t = 0.001$, $h = 1/96$, $\delta = 5 \times 10^{-6}$, The material parameters λ and μ are chosen such that Youngs's modulus, $E = 10^5$ and Poisson's ratio $\nu = 0.4$ and $\alpha = 0.93$, $c_0 = 0$, $\mathbf{k} = 1 \times 10^{-7} \mathbf{I}$, values shown in [81] to typically cause locking. The proposed stabilized finite element method yields a smooth pressure solution without any oscillations as is shown in Figure 5.5b.

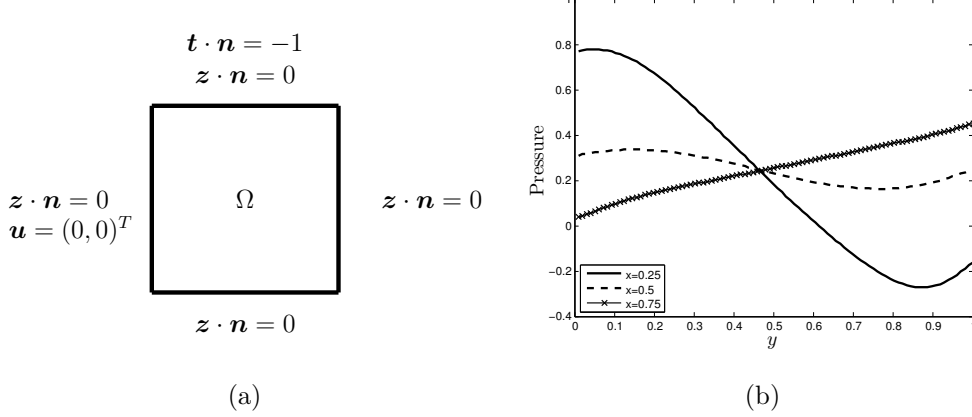


Figure 5.5: (a) Boundary conditions for the cantilever bracket problem. (b) Pressure solution of the cantilever bracket problem at $t = 0.005$.

5.8.4 3D unconfined compression stress relaxation

In this test, a cylindrical specimen of porous tissue is exposed to a prescribed displacement in the axial direction while left free to expand radially. (Note that the two plates are not explicitly modelled in the simulation, but are re-alised through displacement boundary conditions.) After loading the tissue, the displacement is held constant while the tissue relaxes in the radial direction due to interstitial fluid flow through the radial boundary. For the special case of a cylindrical geometry [5] found a closed-form analytical solution for the radial displacement u given by

$$\frac{u}{a}(a, t) = \epsilon_0 \left[\nu + (1 - 2\nu)(1 - \nu) \sum_{n=1}^{\infty} \frac{\exp(-\alpha_n^2 \frac{Mkt}{a^2})}{\alpha_n^2(1 - \nu)^2 - (1 - \nu)} \right]. \quad (5.60)$$

where α_n are the solutions to the characteristic equation $J_1(x) - (1-\nu)xJ_0(x)/(1-2\nu) = 0$, where J_0 and J_1 are Bessel functions, ϵ_0 is the amplitude of the applied axial strain, a is the radius of the cylinder, and t_g is the characteristic time of diffusion (relaxation) $t_g = a^2/Mk$, where $M = \lambda + 2\mu$ is the P-wave modulus of the elastic solid skeleton, and k is the permeability.

The analytical solution available for this test problem describes the displacement of the outer radius which is directly dependent on the amount of mass in the system since the porous medium is assumed to be incompressible and fully saturated. It is therefore an ideal test problem for analyzing the effect that the added stabilization term has on the conservation of mass. In Figure 6.2 we can see that for large values of δ the numerical solution loses mass faster and comes to a steady state that has less mass than the analytical solution. This is a clear limitation of the method and the stability parameter therefore needs to be chosen carefully. However, for 3D problems δ can be chosen to be very small so this effect is negligible, as can be seen in Figure 6.2 for a stable value of $\delta = 0.001$.

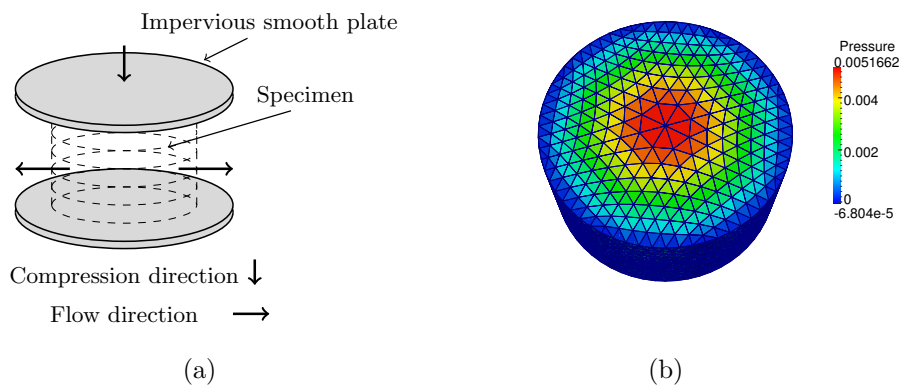


Figure 5.6: (a) Sketch of the test problem. The porous medium is being compressed between two smooth impervious plates. The frictionless plates permit the porous medium to expand in order to conserve volume and then to gradually relax as the fluid seeps out radially. (b) Pressure field solution at $t = 5$, using a mesh with 28160 tetrahedra.

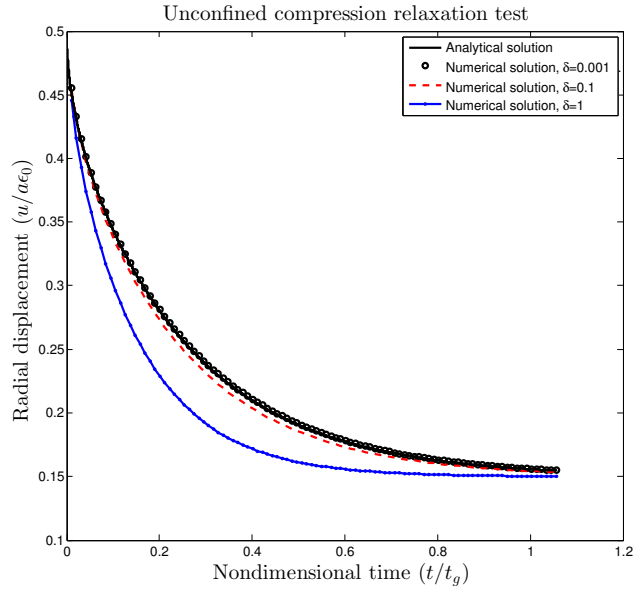


Figure 5.7: Normalized radial displacement versus normalized time calculated using the analytical solution, and using the proposed numerical method with different values of δ . At $t = 0$ the radial expansion is half of the axial compression indicating the instantaneous incompressibility of the poroelastic tissue. The final amount of tissue recoil depends on the intrinsic Poisson ratio of the tissue skeleton.

5.9 Conclusion

The local pressure jump stabilization method [22] is commonly used to solve the Stokes or Darcy equations using piecewise linear approximations for the velocities, and piecewise constant approximations for the pressure variable. The main contribution of this chapter has been to extend these ideas to three-field poroelasticity. We have presented a stability result for the discretized equations that guarantees the existence of a unique solution at each time step,

and derived an energy estimate which can be used to prove weak convergence of the solution to the discretized system to the solution to the continuous problem as the mesh parameters tend to zero. We also derived an optimal error estimate which includes an error for the fluid flux in its natural $H\text{div}$ norm. We have also presented numerical experiments in 2D and 3D that illustrate the convergence of the method, the effectiveness of the method in overcoming spurious pressure oscillations, and the added mass effect of the stabilization term.

Chapter 6

A stabilized finite element method for nonlinear poroelasticity valid in large deformations

6.1 Introduction

In chapter 5, we developed a stabilized, low-order, mixed finite-element method for the fully saturated, incompressible, poroelasticity equations, in the linear, small deformation case. In this chapter we extend this work to the nonlinear, large deformation case.

In section 6.2, we recall the large deformation quasi-static incompressible

poroelastic model. In section 6.3 we present the stabilized nonlinear finite-element method, and provide some implementation details in section 6.4. In section 6.5, we present a range of 3D numerical experiments to verify the accuracy of the method and illustrate its ability to reliably capture steep pressure gradients.

6.2 The model

Following [8] and [3], we recall the governing equations (3.38) for a fully saturated, incompressible poroelastic model valid in large deformations. The problem is to find $\chi(\mathbf{X}, t)$, $\mathbf{z}(\mathbf{x}, t)$ and $p(\mathbf{x}, t)$ such that

$$\begin{aligned}
-\nabla \cdot (\boldsymbol{\sigma}_e - p\mathbf{I}) &= \rho \mathbf{f} && \text{in } \Omega_t, \\
\mathbf{k}^{-1} \mathbf{z} + \nabla p &= \rho^f \mathbf{f} && \text{in } \Omega_t, \\
\nabla \cdot (\mathbf{v}^s + \mathbf{z}) &= g && \text{in } \Omega_t, \\
\chi &= \mathbf{X} + \mathbf{u}_D && \text{on } \Gamma_d, \\
(\boldsymbol{\sigma}_e - p\mathbf{I}) \mathbf{n} &= \mathbf{t}_N && \text{on } \Gamma_t, \\
\mathbf{z} \cdot \mathbf{n} &= q_D && \text{on } \Gamma_f, \\
p &= p_D && \text{on } \Gamma_p, \\
\chi(0) &= \mathbf{X} + \mathbf{u}^0 && \text{in } \Omega_0.
\end{aligned} \tag{6.1}$$

where $\mathbf{v}^s(\mathbf{x}, t) = \frac{\partial}{\partial t} \chi(\mathbf{X}, t)$.

Remark 6.2.1. *It is a straightforward extension to include the solid inertia*

\mathbf{a}^s which can be discretized using a Newmark scheme, see e.g. [23], [64], [85].

6.3 The stabilized finite element method

For ease of presentation, we will assume all Dirichlet boundary conditions are homogeneous, ie., $\mathbf{u}_D = 0, q_D = 0, p_D = 0$.

6.3.1 Weak formulation

To keep the notation similar to chapter 5, we solve for the displacement $\mathbf{u}(\mathbf{X}, t) = \boldsymbol{\chi}(\mathbf{X}, t) - \mathbf{X}$ rather than the deformation map $\boldsymbol{\chi}(\mathbf{X}, t)$, and define the following spaces for deformed location, fluid flux and pressure respectively,

$$\mathbf{W}^E(\Omega) = \{\mathbf{u} \in (H^1(\Omega))^d : \mathbf{u} = 0 \text{ on } \Gamma_D\},$$

$$\mathbf{W}^D(\Omega) = \{\mathbf{z} \in H_{div}(\Omega) : \mathbf{z} \cdot \mathbf{n} = 0 \text{ on } \Gamma_F\},$$

$$\mathcal{L}(\Omega) = \begin{cases} L^2(\Omega) & \text{if } \Gamma_n \cup \Gamma_p \neq \emptyset \\ L_0^2(\Omega) & \text{if } \Gamma_n \cup \Gamma_p = \emptyset, \end{cases},$$

where $L_0^2(\Omega) = \{q \in L^2(\Omega) : \int_{\Omega} q \, dx = 0\}$. We combine these to construct the mixed solution space

$$\mathcal{W}^X = \{\mathbf{W}^E(\Omega) \times \mathbf{W}^D(\Omega) \times \mathcal{L}(\Omega)\}.$$

We make use of the identity $\nabla \cdot (\boldsymbol{\sigma}_e \mathbf{v}) = \nabla \cdot \boldsymbol{\sigma}_e \cdot \mathbf{v} - \boldsymbol{\sigma}_e : \nabla \mathbf{v}$, and the symmetry of $\boldsymbol{\sigma}_e$ to yield the following continuous weak problem. Find $\mathbf{u}(\mathbf{X}, t) \in \mathbf{W}^E(\Omega)$, $\mathbf{z}(\mathbf{x}, t) \in \mathbf{W}^D(\Omega)$, and $p(\mathbf{x}, t) \in \mathcal{L}(\Omega)$ for any time $t \in [0, T]$ such that

$$\begin{aligned} \int_{\Omega_t} \boldsymbol{\sigma}_e : \nabla^S \mathbf{v} \, dv - \int_{\Omega_t} p \nabla \cdot \mathbf{v} \, dv &= \int_{\Omega_t} \rho \mathbf{f} \cdot \mathbf{v} \, dv + \int_{\Gamma_t} \mathbf{t}_N \cdot \mathbf{v} \, ds \quad \forall \mathbf{v} \in \mathbf{W}^E(\Omega), \\ \int_{\Omega_t} \mathbf{k}^{-1} \mathbf{z} \cdot \mathbf{w} \, dv - \int_{\Omega_t} p \nabla \cdot \mathbf{w} \, dv &= \int_{\Omega_t} \rho^f \mathbf{f} \cdot \mathbf{w} \, dv \quad \forall \mathbf{w} \in \mathbf{W}^D(\Omega), \\ \int_{\Omega_t} q \nabla \cdot \mathbf{u}_t \, dv + \int_{\Omega_t} q \nabla \cdot \mathbf{z} \, dv &= \int_{\Omega_t} g q \, dv \quad \forall q \in \mathcal{L}(\Omega). \end{aligned} \tag{6.2}$$

Here $\nabla^S \mathbf{s} = \frac{1}{2} (\nabla \mathbf{s} + (\nabla \mathbf{s})^T)$ for some vector \mathbf{s} .

6.3.2 The fully discrete model

Let \mathcal{T}^h be a partition of Ω into non-overlapping elements K , where h denotes the size of the largest element in \mathcal{T}^h and assume that the partition is quasi-uniform. We define the following finite element spaces,

$$\begin{aligned} \mathbf{W}_h^E &= \left\{ \mathbf{u}_h \in C^0(\Omega) : \mathbf{u}_h|_K \in P_1(K) \quad \forall K \in \mathcal{T}^h, \mathbf{u}_h = 0 \text{ on } \Gamma_D \right\}, \\ \mathbf{W}_h^D &= \left\{ \mathbf{z}_h \in C^0(\Omega) : \mathbf{z}_h|_K \in P_1(K) \quad \forall K \in \mathcal{T}^h, \mathbf{z}_h \cdot \mathbf{n} = 0 \text{ on } \Gamma_F \right\}, \\ Q_h &= \begin{cases} \left\{ p_h : p_h|_K \in P_0(K) \quad \forall K \in \mathcal{T}^h \right\} & \text{if } \Gamma_n \cup \Gamma_p \neq \emptyset \\ \left\{ p_h : p_h|_K \in P_0(K), \int_{\Omega} p_h = 0 \quad \forall K \in \mathcal{T}^h \right\} & \text{if } \Gamma_n \cup \Gamma_p = \emptyset \end{cases}, \end{aligned}$$

where $P_0(K)$ and $P_1(K)$ are respectively the spaces of constant and linear polynomials on K . We partition $[0, T]$ into N evenly spaced non-overlapping

regions $(t_{n-1}, t_n]$, $n = 1, 2, \dots, N$, where $t_n - t_{n-1} = \Delta t$. For any sufficiently smooth function $v(t, x)$ we define $v^n(x) = v(t_n, x)$ and the discrete time derivative by $v_{\Delta t}^n := \frac{v^n - v^{n-1}}{\Delta t}$.

The fully discrete weak problem is: For $n = 1, 2, \dots, N$, find $\mathbf{u}_h^n \in \mathbf{W}_h^E$, $\mathbf{z}_h^n \in \mathbf{W}_h^D$ and $p_h^n \in Q_h$ such that

$$\begin{aligned} \int_{\Omega_t} \boldsymbol{\sigma}_{e,h}^n : \nabla^S \mathbf{v}_h \, dv - \int_{\Omega_t} p_h^n \nabla \cdot \mathbf{v}_h \, dv &= \int_{\Omega_t} \rho \mathbf{f}^n \cdot \mathbf{v}_h \, dv + \int_{\Gamma_t} \mathbf{t}_N^n \cdot \mathbf{v}_h \, ds \quad \forall \mathbf{v}_h \in \mathbf{W}_h^E, \\ \int_{\Omega_t} \mathbf{k}^{-1} \mathbf{z}_h^n \cdot \mathbf{w}_h \, dv - \int_{\Omega_t} p_h^n \nabla \cdot \mathbf{w}_h \, dv &= \int_{\Omega_t} \rho^f \mathbf{f}^n \cdot \mathbf{w}_h \, dv \quad \forall \mathbf{w}_h \in \mathbf{W}_h^D, \\ \int_{\Omega_t} q_h \nabla \cdot \mathbf{u}_{h,\delta t}^n \, dv + \int_{\Omega_t} q_h \nabla \cdot \mathbf{z}_h^n \, dv + J(p_{\delta t,h}^n, q_h) &= \int_{\Omega_t} g^n q_h \, dv \quad \forall q_h \in Q_h. \end{aligned} \tag{6.3}$$

6.3.3 Newton's Method

Since the system of equations (6.3) is highly nonlinear, its solution requires a scheme such as Newton's method. With Newton's method, an improved solution is obtained from a linear approximation of the nonlinear equation at an already computed solution. This first order Taylor expansion corresponds in finite element applications to the linearization of the weak form, and can be obtained by the directional derivative, explained in section 6.3.3. Let $\mathbf{u}^n = \{\mathbf{u}_h^n, \mathbf{z}_h^n, p_h^n\}$ denote the solution vector at a particular time step, $\xi \mathbf{u} = \{\xi \mathbf{u}, \xi \mathbf{z}, \xi p\}$ denote the solution increment vector, and $\mathbf{v} = \{\mathbf{v}_h, \mathbf{w}_h, q_h\}$ the corresponding vector of test functions. Then the nonlinear system of

equations (6.3) can be recast in the form

$$G(\mathbf{u}, \mathbf{v}) = 0, \quad (6.4)$$

where

$$\begin{aligned} G(\mathbf{u}, \mathbf{v}) &= \int_{\Omega_t} \boldsymbol{\sigma}_{e,h}^n : \nabla^S \mathbf{v}_h - p_h^n \nabla \cdot \mathbf{v}_h \\ &+ \int_{\Omega_t} \mathbf{k}^{-1} \mathbf{z}_h^n \cdot \mathbf{w}_h - p_h^n \nabla \cdot \mathbf{w}_h + q_h \nabla \cdot (\mathbf{u}_{\delta t,h}^n + \mathbf{z}_h^n) \, dv + J(p_{\delta t,h}^n, q_h) \\ &- \int_{\Omega_t} \rho \mathbf{f}^n \cdot \mathbf{v}_h + \rho^f \mathbf{f}^n \cdot \mathbf{w}_h + g q_h \, dv - \int_{\Gamma_t} \mathbf{t}_N^n \cdot \mathbf{v}_h \, ds. \end{aligned} \quad (6.5)$$

Considering a trial solution $\bar{\mathbf{u}}$, equation (6.4) can now be linearized in the direction of an increment $\xi \mathbf{u}$ at $\bar{\mathbf{u}}$ as

$$G(\bar{\mathbf{u}}, \mathbf{v}) + DG(\bar{\mathbf{u}}, \mathbf{v})[\xi \mathbf{u}] = 0, \quad (6.6)$$

or

$$DG(\bar{\mathbf{u}}, \mathbf{v})[\xi \mathbf{u}] = -G(\bar{\mathbf{u}}, \mathbf{v}), \quad (6.7)$$

which essentially is Newton's method (see algorithm 2 for the fully discrete version).

Linearization

In biphasic tissue problems, it is common to approximate the tangent by taking the nonlinear elasticity term as the only nonlinearity present and

ignoring the other nonlinearities [94, 103].

The dominant nonlinearity in (6.5) is the elasticity term denoted by

$$E((\mathbf{u}_h^n, p_h^n), \mathbf{v}_h) = \int_{\Omega_t} \boldsymbol{\sigma}_{e,h}^n : \nabla^S \mathbf{v}_h - p_h^n \nabla \cdot \mathbf{v}_h \, dv. \quad (6.8)$$

For Newton's method we require the directional derivative of $E(\mathbf{u}_h, \mathbf{v}_h)$ at a particular trial solution $\bar{\mathbf{u}}_h$ in the direction $\xi \mathbf{u}$, given by (see [106, section 3.5.3])

$$\begin{aligned} DE((\bar{\mathbf{u}}_h^n, \bar{p}_h^n), \mathbf{v}_h)[\xi \mathbf{u}] &= \int_{\Omega_t} \nabla^S \mathbf{v}_h : \bar{\boldsymbol{\Theta}}_h^n : \nabla^S \xi \mathbf{u} \\ &\quad + \bar{\boldsymbol{\sigma}}_{e,h}^n : ((\nabla \xi \mathbf{u})^T \cdot \nabla \mathbf{v}_h) \, dv, \end{aligned} \quad (6.9)$$

where $\bar{\boldsymbol{\Theta}}_h^n$ is the fully-discrete, fourth-order spatial tangent modulus tensor and $\bar{\boldsymbol{\sigma}}_{e,h}^n$ is the effective (elastic) stress tensor both evaluated at a trial solution $\bar{\mathbf{u}}_h^n$. Any variable with a bar above it will correspond to it being evaluated at a trial solution and will therefore be considered as a known quantity. In the fully discrete algorithm 2, this trial solution will correspond to the solution of the previous Newton step. The spatial tangent modulus tensor $\boldsymbol{\Theta}$, due to its complexity, is described in section A.1. For a detailed explanation and derivation see [16, 106]. The approximate linearization of

the nonlinear problem (6.4) is thus given by

$$\begin{aligned}
& DG(\bar{\mathbf{u}}, \mathbf{v}) \xi \mathbf{u} \\
& \approx \int_{\Omega_t} \nabla^S \mathbf{v}_h : \overline{\Theta_h^n} : \nabla^S \xi \mathbf{u} \\
& + \overline{\sigma_{e,h}} : ((\nabla \xi \mathbf{u})^T \cdot \nabla \mathbf{v}_h) - \xi p \nabla \cdot \mathbf{v}_h \, dv \\
& + \int_{\Omega_t} \bar{\mathbf{k}}^{-1} \xi \mathbf{z} \cdot \mathbf{w}_h - \xi p \nabla \cdot \mathbf{w}_h \, dv + \int_{\Omega_t} q_h \nabla \cdot \left(\frac{\xi \mathbf{u}}{\Delta t} + \xi \mathbf{z} \right) \, dv + J(p_{\delta t,h}^n, q_h).
\end{aligned} \tag{6.10}$$

The fully discretized weak problem at each Newton step, to get an update for the approximate solution, is to find $\xi \mathbf{u} \in \mathbf{W}_h^E$, $\xi \mathbf{z} \in \mathbf{W}_h^D$ and $\xi p \in Q_h$ such that:

$$\begin{aligned}
& \int_{\Omega_t} \nabla^S \mathbf{v}_h : \overline{\Theta_h^n} : \nabla^S \xi \mathbf{u} + \overline{\sigma_{e,h}^n} : ((\nabla \xi \mathbf{u})^T \cdot \nabla \mathbf{v}_h) - \xi p \nabla \cdot \mathbf{v}_h \, dv \\
& + \int_{\Omega_t} \bar{\mathbf{k}}^{-1} \xi \mathbf{z} \cdot \mathbf{w}_h \, dv - \xi p \nabla \cdot \mathbf{w}_h \, dv \\
& + \int_{\Omega_t} q_h \nabla \cdot \left(\frac{\xi \mathbf{u}}{\Delta t} + \xi \mathbf{z} \right) \, dv + J \left(\frac{\xi p}{\Delta t}, q_h \right) \\
& = \int_{\Omega_t} \frac{1}{2} \overline{\sigma_{e,h}^n} : (\nabla \mathbf{v}_h + (\nabla \mathbf{v}_h)^T) - \overline{p_h^n} \nabla \cdot \mathbf{v}_h - \overline{\rho f^n} \cdot \mathbf{v}_h \, dv - \int_{\Gamma_t} \mathbf{t}_N^n \cdot \mathbf{v}_h \, ds \\
& + \int_{\Omega_t} \bar{\mathbf{k}}^{-1} \overline{\mathbf{z}_h^n} \cdot \mathbf{w}_h \, dv - \overline{p_h^n} \cdot \nabla \mathbf{w}_h \, dv - \overline{\rho f^n} \cdot \mathbf{w} \, dv \\
& + \int_{\Omega_t} q_h \nabla \cdot (\overline{\mathbf{u}_{\delta t,h}} + \overline{\mathbf{z}_h}) + J(\overline{p_{\delta t,h}}, q_h) - g q_h \, dv \quad \forall (\mathbf{v}_h, \mathbf{w}_h, q_h) \in \mathbf{W}_h^E, \mathbf{W}_h^D, Q_h.
\end{aligned} \tag{6.11}$$

We can rewrite this using more compact notation

$$DG(\bar{\mathbf{u}}, \mathbf{v})\xi \mathbf{u} = -G(\bar{\mathbf{u}}, \mathbf{v}). \quad (6.12)$$

6.4 Implementation details

6.4.1 Newton algorithm

We will now let $\mathbf{u}_i^n := \{\mathbf{u}_i^n, \mathbf{z}_i^n, p_i^n\}$ denote the fully discrete solution at the i th step within the Newton method at time t^n . To ease the notation, we have suppressed the lower case h , previously used to denote the spatial discretization. To solve the nonlinear poroelastic problem using Newton's method at a particular time step, we perform the following steps:

Algorithm 2 Fully discrete Newton's algorithm

- 1: $i = 0$
 - 2: $\mathbf{u}_0^n = \{\mathbf{u}^{n-1}, \mathbf{z}^{n-1}, p^{n-1}\}$
 - 3: **while** $\| \mathbf{R}(\mathbf{u}_i^n, \mathbf{u}^{n-1}) \| > \text{TOL} \& i < \text{ITEMAX}$ **do**
 - 4: Assemble $\mathbf{R}(\mathbf{u}_i^n, \mathbf{u}^{n-1})$ and $\mathbf{K}(\mathbf{u}_i^n)$
 - 5: Solve $\mathbf{K}(\mathbf{u}_i^n) \xi \mathbf{u}_{i+1}^n = -\mathbf{R}(\mathbf{u}_i^n, \mathbf{u}^{n-1})$
 - 6: Compute $\mathbf{u}_{i+1}^n = \mathbf{u}_i^n + \xi \mathbf{u}_{i+1}^n$
 - 7: Update the mesh, $\Omega_t = \mathbf{X} + \mathbf{u}_i^n$
 - 8: $i = i + 1$
 - 9: **end while**
-

where $\mathbf{K}(\mathbf{u}_i^n)$ and $\mathbf{R}(\mathbf{u}_i^n, \mathbf{u}^{n-1})$ are the matrix and vector representations of $DG(\mathbf{u}_i^n)$ and $G(\mathbf{u}_i^n, \mathbf{u}^{n-1})$, respectively. At each Newton iteration we solve the linear system

$$\mathbf{K}(\mathbf{u}_i^n)\xi\mathbf{u}_{i+1}^n = -\mathbf{R}(\mathbf{u}_i^n, \mathbf{u}^{n-1}), \quad (6.13)$$

which can be expanded, and written as

$$\begin{bmatrix} \mathbf{K}^e & 0 & \mathbf{B}^T \\ 0 & \mathbf{M} & \mathbf{B}^T \\ -\mathbf{B} & -\Delta t \mathbf{B} & \mathbf{J} \end{bmatrix} \begin{bmatrix} \xi \mathbf{u}_{i+1}^n \\ \xi z_{i+1}^n \\ \xi \mathbf{p}_{i+1}^n \end{bmatrix} = - \begin{bmatrix} \mathbf{r}_1(\mathbf{u}_i^n, p_i^n) \\ \mathbf{r}_2(\mathbf{u}_i^n, \mathbf{z}_i^n, p_i^n) \\ \mathbf{r}_3(\mathbf{u}_i^n, \mathbf{u}^{n-1}, \mathbf{z}_i^n, p_i^n) \end{bmatrix},$$

where we have defined the following matrices:

$$\begin{aligned} \mathbf{K}^e &= [\mathbf{a}_{kl}], \quad \mathbf{k}_{kl}^e = \int_{\Omega_t} \mathbf{E}_k^T \mathbf{D}(\mathbf{u}_i^n) \mathbf{E}_l + (\nabla \phi_k)^T \boldsymbol{\sigma}_e(\mathbf{u}_i^n) \nabla \phi_l \, dv, \\ \mathbf{M} &= [\mathbf{m}_{kl}], \quad \mathbf{m}_{kl} = \int_{\Omega_t} \mathbf{k}^{-1}(\mathbf{u}_i^n) \phi_k \cdot \phi_l \, dv, \\ \mathbf{B} &= [\mathbf{b}_{kl}], \quad \mathbf{b}_{kl} = - \int_{\Omega_t} \psi_k \nabla \cdot \phi_l \, dv, \\ \mathbf{J} &= [\mathbf{j}_{kl}], \quad \mathbf{j}_{kl} = \delta \sum_K \int_{\partial k \setminus \partial \Omega_t} h_{\partial K}[\psi_k] [\psi_k] \, ds. \\ \mathbf{r}_1 &= [\mathbf{r}_{1i}], \quad \mathbf{r}_{1i} = \int_{\Omega_t} (\boldsymbol{\sigma}_e(\mathbf{u}_i^n) - p_i^n \mathbf{I}) : \nabla \phi_i - \rho(\mathbf{u}_i^n) \phi_i \cdot \mathbf{f} \, dv - \int_{\Gamma_t} \phi_i \cdot \mathbf{t}_N \, ds, \\ \mathbf{r}_2 &= [\mathbf{r}_{2i}], \quad \mathbf{r}_{2i} = \int_{\Omega_t} \mathbf{k}^{-1}(\mathbf{u}_i^n) \phi_i \cdot \mathbf{z}_i^n - p_i^n \nabla \cdot \phi_i - \rho^f(\mathbf{u}_i^n) \phi_i \cdot \mathbf{f} \, dv, \\ \mathbf{r}_3 &= [\mathbf{r}_{3i}], \quad \mathbf{r}_{3i} = \int_{\Omega_t} \psi_i \nabla \cdot (\mathbf{u}_i^n - \mathbf{u}^{n-1}) + \Delta t \psi_i \nabla \cdot \mathbf{z}_i^n - \Delta t \psi_i g \, dv \\ &\quad + \delta \sum_K \int_{\partial k \setminus \partial \Omega_t} h_{\partial K}[\psi_i] [p_i^n - p^{n-1}] \, ds. \end{aligned}$$

Here ϕ_k are vector valued linear basis functions such that the displacement vector at the i th iteration can be written as $\mathbf{u}_i^n = \sum_{k=1}^{n_u} \mathbf{u}_{i,k}^n \phi_k$, with $\sum_{k=1}^{n_u} \mathbf{u}_{i,k}^n \phi_k \in \mathbf{W}_h^E$. Similarly for the fluid flux vector we have $\mathbf{z}_i^n = \sum_{k=1}^{n_z} \mathbf{z}_{i,k}^n \phi_k$, with $\sum_{k=1}^{n_z} \mathbf{z}_{i,k}^n \phi_k \in \mathbf{W}_h^D$. The scalar valued constant basis functions ψ_i are used to approximate the pressure, such that $\mathbf{p}_i^n = \sum_{k=1}^{n_p} p_{i,k}^n \psi_k$, with $\sum_{k=1}^{n_p} p_{i,k}^n \psi_k \in Q_h$. Also to aid the assembly of the fourth order tensor we have adopted the matrix voigt notation. In particular \mathbf{D} is the matrix form of Θ , and \mathbf{E}_k is the matrix version of $\nabla^S \phi_k$, see (A.3) and (A.4) for details.

6.4.2 No-flux boundary condition

We introduce a Lagrange multiplier Λ , to enforce the no-flux boundary condition $\mathbf{z} \cdot \mathbf{n} = 0$ along the boundary Γ_f . Let $W^f = \{\Lambda \in H_{div}(\Gamma_f, \mathbb{R})\}$. The resulting modified continuous weak-form is now:

$$\begin{aligned} G((\mathbf{u}, \mathbf{z}, p), (\mathbf{v}, \mathbf{w}, q)) + (\Lambda, \mathbf{w} \cdot \mathbf{n})_{\Gamma_f} &= 0 \quad \forall (\mathbf{v}, \mathbf{w}, q) \in \mathbf{W}^E(\Omega), \mathbf{W}^D(\Omega), \mathcal{L}(\Omega), \\ (\mathbf{z} \cdot \mathbf{n}, \mathbf{l})_{\Gamma_f} &= 0, \quad \forall \mathbf{l} \in W^f. \end{aligned} \tag{6.14}$$

The discretization and implementation of this additional constraint is straightforward and results in a linear system with additional degrees of freedom for every node on Γ_f . The terms $(\Lambda, \mathbf{w} \cdot \mathbf{n})_{\Gamma_f}$ and $(\mathbf{z} \cdot \mathbf{n}, \mathbf{l})_{\Gamma_f}$ are nonlinear since the normal is a function of the displacement. However we have found that treating these terms as linear terms does not affect the convergence of

the Newton algorithm. Alternatively these terms could be linearized as has been described in detail for the traction boundary condition, see [106, section 4.2.5].

6.5 Numerical results

We present four numerical examples to test the performance of the proposed stabilized finite element method. The first two examples are from mechanobiology and geotechnical applications, the third is a swelling example that undergoes significant large deformations and the fourth is an application from respiratory physiology. For the implementation we used the C++ library libmesh [54], and the multi-frontal direct solver mumps [4] to solve the resulting linear systems. For the strain energy law we chose a Neo-Hookean law taken from [106, eqn. (3.119)], with the penalty term chosen such that $0 \leq \phi < 1$, namely

$$W(\mathbf{C}) = \frac{\mu}{2}(\text{tr}(\mathbf{C}) - 3) + \frac{\lambda}{4}(J^2 - 1) - (\mu + \frac{\lambda}{2})\ln(J - 1 + \phi_0). \quad (6.15)$$

For further discussion on strain energy laws for poroelasticity we refer to [24] and [97]. The material parameters μ and λ in (6.15) can be related to the Young's modulus E and the Poisson ratio ν by $\mu = E/(2(1 + \nu))$ and $\lambda = (E\nu)/((1 + \nu)(1 - 2\nu))$. Details of the effective stress tensor and

fourth-order spatial tangent modulus for this particular law can be found in A.3. For the permeability law we chose

$$\mathbf{k}_0(\mathbf{C}) = k_0 \mathbf{I}. \quad (6.16)$$

6.5.1 3D unconfined compression stress relaxation

In this test, a cylindrical specimen of porous tissue is exposed to a prescribed displacement in the axial direction while left free to expand radially. The original experiment involved a specimen of articular cartilage being compressed via impervious smooth plates as shown in Figure 6.1a. Note that the two plates are not explicitly modelled in the simulation, but are realised through displacement boundary conditions. After loading the tissue, the displacement is held constant and the tissue is allowed to relax in the radial direction. The fluid pressure was constrained to zero at the outer radial surface. The outer radial boundary is permeable and free-draining, the upper and lower fluid boundaries are impermeable and frictionless. The outer radius and height of the cylinder is 5mm, whereas the axial compression is 0.01mm. The parameters used for the simulation can be found in Table 6.1. For the special case of a cylindrical geometry, [5] provides a closed-form analytical solution for the radial displacement on the porous medium in response to a step loading function.

The analytical solution for the radial displacement to this unconfined

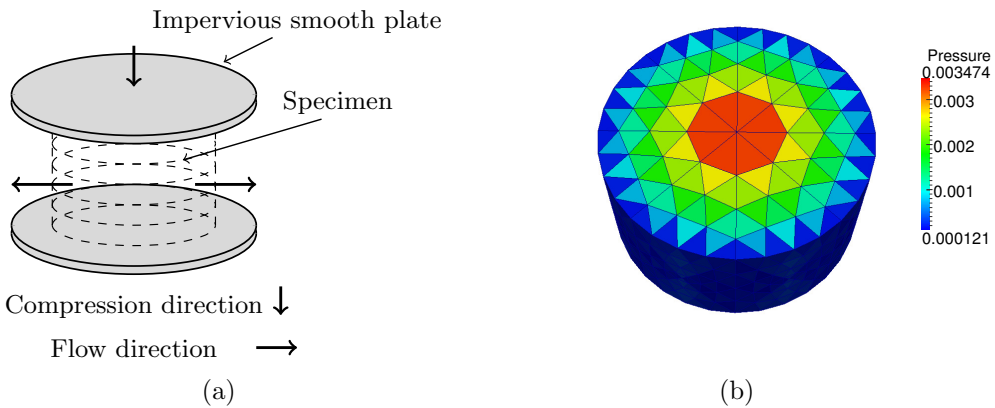


Figure 6.1: (a) The test problem. (b) Pressure field at $t = 200\text{s}$ using a mesh with 3080 tetrahedra.

Parameter	Description	Value
k	Dynamic permeability	$10^{-3} \text{ m}^3 \text{s kg}^{-1}$
ν	Poisson's ratio	0.15
E	Young's modulus	$1000 \text{ kg m}^{-1} \text{s}^{-2}$
Δt	Time step used in the simulation	4 s
T	Final time of the simulation	1000 s
δ	Stabilization parameter	10^{-3}

Table 6.1: Parameters used for the unconfined compression test problem.

compression test is given by

$$\frac{u}{a}(a, t) = \epsilon_0 \left[\nu + (1 - 2\nu)(1 - \nu) \sum_{n=1}^{\infty} \frac{\exp(-\alpha_n^2 \frac{Mkt}{a^2})}{\alpha_n^2(1 - \nu)^2 - (1 - \nu)} \right]. \quad (6.17)$$

Here α_n are the solutions to the characteristic equation, given by $J_1(x) - (1 - \nu)xJ_0(x)/(1 - 2\nu) = 0$, where J_0 and J_1 are Bessel functions. We also have that ϵ_0 is the amplitude of the applied axial strain, a is the radius of the cylinder, and t_g is the characteristic time of diffusion given by $t_g = a^2/Mk$,

where $M = \lambda + 2\mu$ is the P-wave modulus of the elastic solid skeleton, and k is the permeability. The computed radial displacement (Figure 6.2) shows good agreement with the analytical solution provided by [5]. The same problem has been used to test other large deformation poroelastic software such as FEBio [69]. The effect of the stabilization parameter on the numerical solution has already been investigated in section 6.5.1.

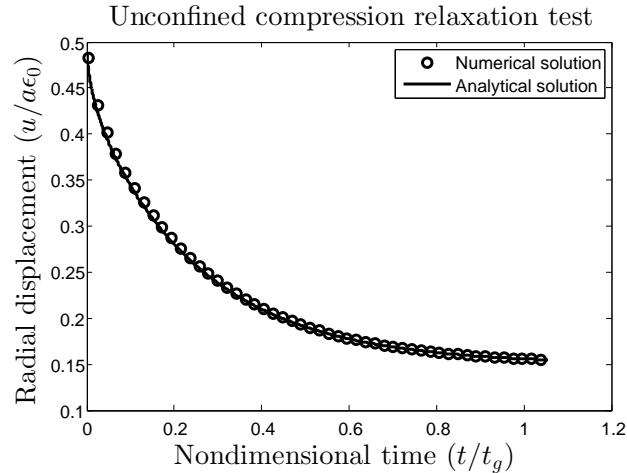


Figure 6.2: Radial expansion versus time comparing the analytical and numerical solutions with $\delta = 0.001$.

6.5.2 Terzaghi's problem

This is a classical geomechanics example with an analytical solution, and has been used to investigate finite element pressure oscillations, caused by overshooting of the numerical solution near the boundary [73, 103]. The domain consists of a porous column of unit height, bounded at the sides and

bottom by rigid and impermeable walls. The top is free to drain ($p_D = 0$) and has a downward traction force, p_0 , applied to it. The boundary and initial conditions for this 1D problem can be written as

$$\begin{aligned} t_N &= -p_0, \quad p_D = 0 \text{ on } x = 0, \\ u &= 0, \quad z = 0, \text{ on } x = 1, \\ u &= 0, \quad z = 0, \quad p = 0 \text{ in } (0, 1). \end{aligned} \tag{6.18}$$

The analytical pressure solution, in non-dimensional form is given by

$$p^* = \sum_n^{\infty} \frac{2}{\pi(n + 1/2)} \sin(\pi(n + 1/2)) \exp^{-\pi(n+1/2)(\lambda+2\mu)kt}. \tag{6.19}$$

When the poroelastic medium is subjected to the sudden loading, the saturating fluid undergoes an overpressurization. Subsequently this overpressure progressively vanishes, owing to the diffusion process of the fluid towards the boundary at the top of the column, which remains drained. For a detailed explanation and derivation of this solution see [106, section 5.2.2]. We discretized the column using 60 hexahedra elements and solved the problem using the proposed stabilized low-order finite element method and a higher-order inf-sup stable finite element method that uses a piecewise linear pressure approximation. The simulation results of the pressure for the two methods, taken at $t = 0.01s$ and $t = 1s$ are shown in Figure 6.3. The material parameters used for the simulation can be found in Table 6.2. At $t = 0.01s$ the piecewise linear (continuous) approximation suffers from over-

shooting due to the boundary layer solution (Figure 6.3a). The proposed method, which uses a piecewise constant pressure approximation does not suffer from this problem, and captures the pressure boundary layer solution reliably (Figure 6.3b). At $t = 1\text{s}$ the boundary layer has grown and both the piecewise linear (Figure 6.3c) and piecewise constant (Figure 6.3d) approximation yield satisfactory results.

Parameter	Description	Value
k_0	Dynamic permeability	$10^{-5} \text{ m}^3 \text{s kg}^{-1}$
ν	Poisson ratio	0.25
E	Young's modulus	$100 \text{ kg m}^{-1} \text{s}^{-2}$
Δt	Time step used in the simulation	0.01 s
T	Final time of the simulation	1 s
δ	Stabilization parameter	2×10^{-5}

Table 6.2: Parameters used for Terzaghi's problem.

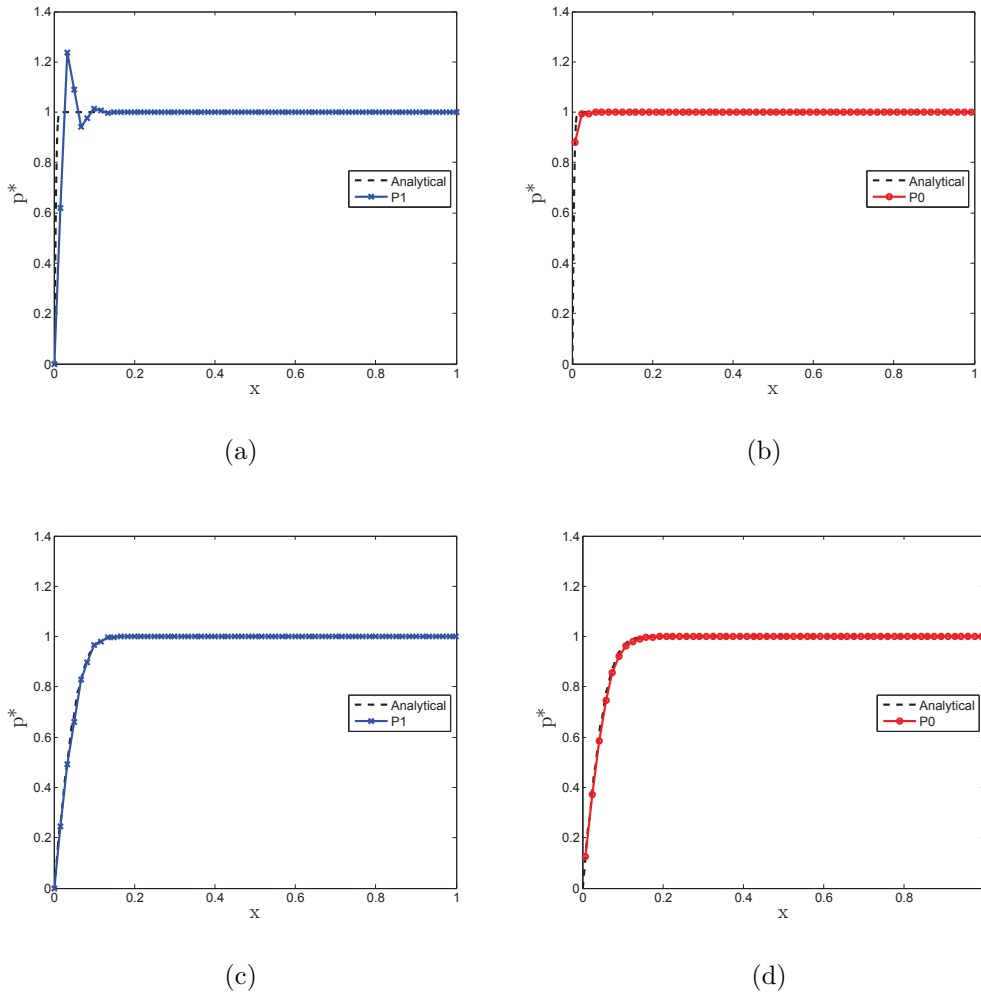


Figure 6.3: (a) Pressure at $t = 0.01s$ using a continuous linear pressure approximation. (b) Pressure at $t = 0.01s$ using a discontinuous piecewise constant approximation. (c) Pressure at $t = 1s$ using a continuous linear pressure approximation. (d) Pressure at $t = 1s$ using a discontinuous piecewise constant approximation.

6.5.3 Swelling test

This problem is similar to the one in [23] and highlights the method's ability to reliably capture jumps in the pressure solution due to changes in material parameters. Given a unit cube of material, a fluid pressure gradient is imposed between the two opposite faces at $X = 0$ and $X = 1$. The pressure p_D on the inlet face $X = 0$ is increased very rapidly from zero to a limiting value of 10kPa, i.e., $p_D = 10^4(1 - \exp(-t^2/0.25))$ Pa). On the outlet face $X = 1$, the pressure is fixed to be zero, $p_D = 0$. There are no sources or sinks of fluid. A zero flux condition is applied for the fluid velocity on the four other faces ($Y = 0, 1$, $Z = 0, 1$). Normal displacements are required to be zero on the planes $X = 0$, $Y = 0$ and $Z = 0$. The permeability of the cube $0 < X < 0.5, 0.5 < Y < 1, 0 < Z < 0.5$ (1/8 of the volume of the unit cube) is smaller than in the rest of the domain by a factor of 500. The computational domain shown in Figure 6.4a, highlighting the region of reduced permeability. The parameters chosen for this test problem are shown in Table 6.3.

Fluid enters the region from the inlet face and the material swells like a sponge, undergoing large deformation as shown in Figure (6.4b). The evolution of the pressure and the Jacobian at the points at $(0, 0, 1)$, $(0.5, 0, 1)$ and $(1, 0, 1)$ in the reference configuration is shown in Figures (6.5a) and (6.5b) respectively. These position are indicated by the red, blue and green balls in Figure 6.4a. The pressure decreases roughly linearly with x , the increase in volume also follows a similar pattern. The pressure and volume change at

the point $(0, 1, 0)$ (black ball in Figure 6.4a) is also shown in Figures (6.5a) and (6.5b). Due to its reduced permeability this region is much slower to swell and achieve its ultimate equilibrium state and the fluid mainly flows around the area of reduced permeability, see Figure 6.4b. The steep pressure gradients at the boundary of the less permeable region seen in Figure 6.4b are well approximated by the piecewise constant (discontinuous) pressure space even on this relatively coarse discretization. Continuous pressure spaces would require a much finer discretization in this region.

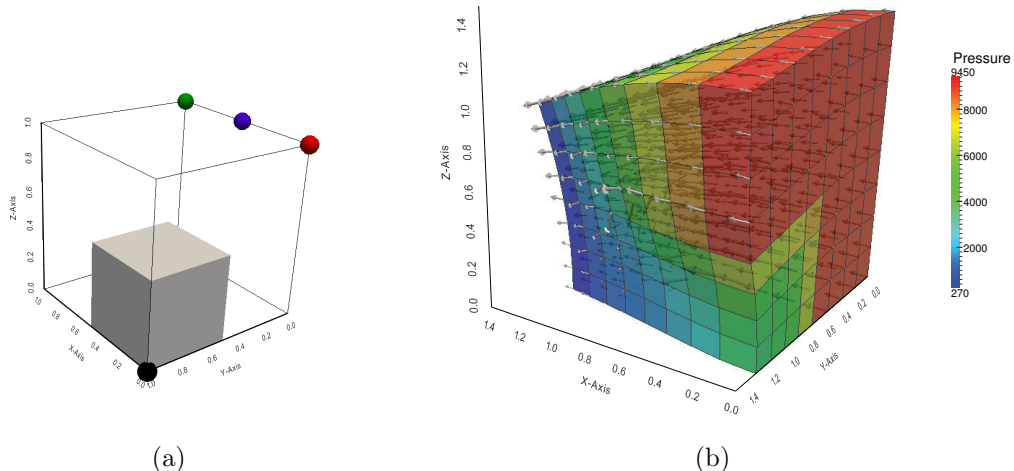


Figure 6.4: (a) Initial simulation setup. The grey cube represents the area of reduced permeability. The colored balls highlight the position of the points used for tracking the pressure and volume change during the simulation, shown in Figures 6.5a and 6.5b. (b) The deformed cube after 1s. The pressure solution is plotted and the jumps in pressure at the interface between the high and low permeability regions can clearly be seen. The arrows illustrate the fluid-flux profile.

Parameter	Value
k_0	$10^{-5} \text{ m}^3 \text{s kg}^{-1}$
ν	0.3
E	$8000 \text{ kg m}^{-1} \text{s}^{-2}$
Δt	0.02 s
T	20 s
δ	10^{-4}

Table 6.3: Parameters used for the swelling test problem.

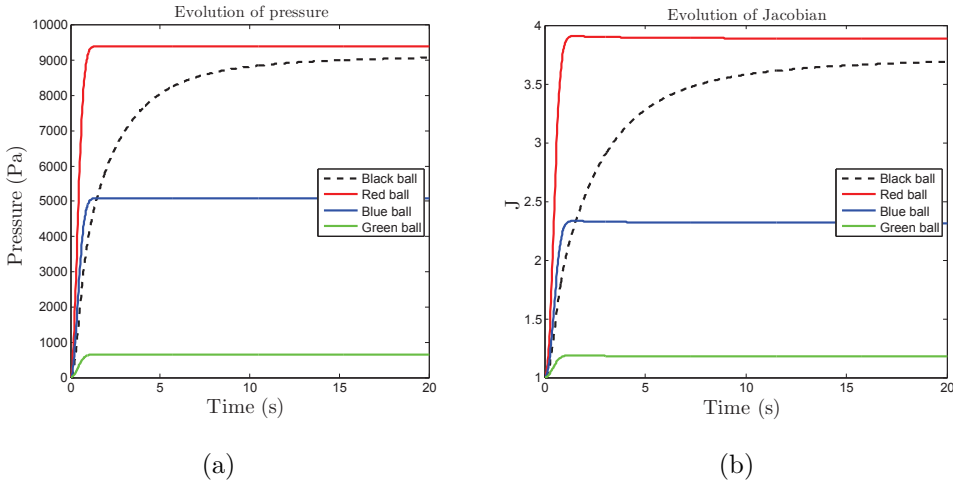


Figure 6.5: Pressure (a) and volume change, J , (b) are plotted against time for four points, $(0, 0, 1)$ (red), $(0.5, 0, 1)$ (blue), $(1, 0, 1)$ (green), and $(1, 0, 1)$ (black) in the reference configuration. The position of these balls is also shown in Figure 6.4a.

6.6 Conclusion

The main contribution of this chapter has been to extend the local pressure jump stabilization method [22], already applied to three-field linear poro-

lasticity in chapter 5 to the large deformation case. Thus, the proposed scheme is built on an existing scheme, for which rigorous theoretical results about the stability and optimal convergence have been proven, and numerical experiments have confirmed its ability to overcome spurious pressure oscillations. Due to the discontinuous pressure approximation, sharp pressure gradients due to changes in material coefficients or boundary layer solutions can be captured reliably, circumventing the need for severe mesh refinement. Also, the addition of the stabilization term introduces minimal additional computational work, can be assembled locally on each element using standard element information, and leads to a symmetric addition to the original system matrix, thus preserving any existing symmetry. As the numerical examples have demonstrated, the stabilization scheme is robust and leads to high-quality solutions.

Chapter 7

A poroelastic-fluid-network model of the lung

7.1 Introduction

The aim of this chapter is not to present the most complete or accurate ventilation or deformation lung model to date. Instead we aim to present a new methodology and highlight some of the modelling assumptions required for a poroelastic lung model. We hope that this model will in future be extended to include sophisticated flow models of the airways, more advanced constitutive laws that make use of additional imaging data to parametrize the model, and improved registration algorithms, to yield a more realistic and accurate full organ lung model.

The rest of this chapter is organized as follows. In section 5.2 we present

the assumptions and define the mathematical lung model and describe its implementation. In section 7.5 we describe the generation of the computational lung geometry and boundary conditions, and in section 7.6 we present numerical simulations of tidal breathing, and investigate the effect of airway constriction and tissue weakening. Finally in section 7.7, we conclude and outline future work to improve the current lung model.

7.2 Lung model assumptions

7.2.1 Approximating lung parenchyma using a poroelastic medium

Averaging over the tissue: One of the major assumptions is that we can approximate the lung parenchyma using a poroelastic continuum description. This makes our model computationally tractable and allows us to use the well established theory of poroelasticity to couple the air with the tissue.

The use of a continuum model can be further supported by looking at the different length scales and structures of the tissue. For the microscopic length scale denoted by l of the parenchyma we will use the diameter of an alveolus that can be approximated to be 0.02 cm [74]. The macroscopic length scale L can be taken to be the diameter of a segment which measures around 4 cm of tissue. So the ratio of the different length scales is small i.e

$\epsilon := \frac{l}{L} \approx 0.005 \ll 1$. This along with the assumption that the structure of an acinus is porous (see Figures 2.1b and 2.1a) and approximately periodic supports the use of averaging techniques over the tissue to obtain a continuum description in the form of a poroelastic medium. To further simplify the poroelastic equations we assume that the poroelastic continuum can be described by a solid phase (blood and tissue) and a fluid phase (air), where both phases are assumed to be incompressible. The interaction between the fluid pressure and the deformation of the solid skeleton is assumed to obey the effective stress principle. Note that by averaging over the tissue we do not seek to model individual alveoli but introduce macroscopic parameters such as the permeability and elasticity coefficients. In general, lung diseases usually affect significant regions of alveoli (lung tissue), thus, by changing the macro-scale parameters over the affected area of tissue we are still able to model changes in the tissue due to disease.

Ignoring blood flow: Apart from collagen, fibers and air the other major component in the lung is blood. The volume taken up by collagen and elastin fibers is similar to the volume occupied by the capillaries filled with blood (illustrated in Figure 2.1b). In fact, the space not occupied by air is about 7% of the parenchymal volume and is made up of 50% capillary blood and 50% of collagen and elastin fibers [99]. Also the density of blood is similar to the density of tissue and much larger than that of air ($1060 \text{ kg m}^{-3} \gg 1.18 \text{ kg m}^{-3}$). Since the capillaries are constantly filled with blood and the density of blood is similar to that of alveolar tissue we will make the simplifying assumption

that the blood is simply part of the tissue (solid phase) and thus ignore accelerations and any redistribution of blood during breathing.

Assuming incompressibility of the solid and the fluid: Blood and tissue can be assumed to be incompressible. Under physiological conditions, air can also be assumed to be incompressible [49].

Ignoring solid inertia forces: Simple calculations considering the sinusoidal motion of tissue near the diaphragm during normal breathing yield an estimate of 0.02 ms^{-2} for the maximum acceleration of lung parenchyma. Compared to the acceleration of gravity this is negligible, and it is therefore reasonable to ignore the inertia forces in the tissue.

Ignoring fluid inertia forces: The fluid's Reynolds number in the lower airways that form part of the lung parenchyma, has been estimated to be around 1 to 0.01 [78]. Due to this relatively low Reynolds number we choose to ignore fluid inertia forces in the poroelastic medium.

Ignoring viscous forces in the fluid: A dimensional analysis shows that the viscous stress in the fluid is small compared to the drag forces between the fluid and the porous structure, when the ratio of the different length scales is small [70]. We will therefore neglect the fluid viscous stress implying that the fluid behaves more or less inviscid within the porous structure.

7.2.2 Approximating the airways using a fluid network model

In order to make the coupled model computationally feasible we assume that a simple laminar flow model can describe the air flow in the airways and we make the common Poiseuille flow assumption. This flow assumption is also made in [60, 89] where the air flow in a whole airway tree, from trachea down to the final bronchioles was assumed to be governed by Poiseuille flow. Diseases affecting the airway tree can be modelled effectively by changing resistance (airway radius) parameters in the network flow model.

7.3 Mathematical model

7.3.1 A poroelastic model for lung parenchyma

Having made the assumptions in section 7.2 for the tissue we are left with the large deformation quasi-static incompressible poroelastic model (3.38).

Constitutive laws.

To close the poroelastic model for the tissue (3.38) we need to choose constitutive laws for the permeability and strain energy. We will use the same permeability law that has already been proposed in [56] to model lung parenchyma,

$$\mathbf{k}_0 = k_0 \left(J \frac{\phi}{\phi_0} \right)^{2/3} \mathbf{I}. \quad (7.1)$$

Exponential strain energy laws for lung parenchyma exist, for example the popular law by [38]. However little is known about how the constants in these laws should be interpreted and altered to model weakening of the tissue in an diseased state. Further, the constants in these laws are thought to have no physical meaning [92]. To make the interpretation of the elasticity constants and dynamics of the model as simple as possible we chose a Neo-Hookean law taken from [106], with the penalty term chosen such that $0 \leq \phi < 1$,

$$W(\mathbf{C}) = \frac{\mu}{2}(\text{tr}(\mathbf{C}) - 3) + \frac{\lambda}{4}(J^2 - 1) - (\mu + \frac{\lambda}{2})\ln(J - 1 + \phi_0). \quad (7.2)$$

The material parameters μ and λ can be related to the more familiar Young's modulus E and the Poisson ratio ν by $\mu = \frac{E}{2(1+\nu)}$ and $\lambda = \frac{E\nu}{(1+\nu)(1-2\nu)}$. The values of these constants for modelling lung tissue have been investigated [31, 100, 111] and are shown in Table 7.1.

7.3.2 A network flow model for the airway tree

The flow rate Q_i through the i th pipe segment in the fluid network is given by the pressure-flow relationship

$$P_{i,1} - P_{i,2} = R_i Q_i, \quad (7.3)$$

where $R_i = \frac{8l\mu_f}{\pi r^4}$ is the Poiseuille flow resistance of a pipe segment (r is the radius, l is the length of the pipe, μ_f is the dynamic viscosity) and $P_{i,1}$ and

$P_{i,2}$ are the pressures at the proximal and distal nodes of the pipe segment, respectively. We also have conservation of flow at branches such that

$$Q_i = \sum_{Q_{i,j} \in Q_i} Q_{i,j}, \quad (7.4)$$

where $Q_{i,j}$ are the flow rates of the children branches of the i th flow segment. The outlet pressure of the fluid network is set using the boundary condition $P_0 = \hat{P}$.

Coupling the fluid network to the poroelastic model.

We introduce subdomains to identify the region of the domain that is supplied with fluid from a specific branch of the fluid network and returns fluid through that branch. We construct an approximate Voronoi tessellation based on the terminal end locations of the fluid network, so that the i th subdomain Ω_t^i is the set of finite elements whose centroids are closer to the i th inlet than any of the other inlets. Obviously we have $\Omega_t = \sum_i^N \Omega_t^i$. The introduction of subdomains allows each endpoint of the fluid network to supply and remove fluid from the poroelastic medium at different spatial locations. The i th subdomain Ω_t^i is defined as the volume closest to the position of the i th inlet, denoted by $\text{pos}(P_{di})$.

$$\Omega_t^i := \{\mathbf{x} \in \Omega_t : \|\mathbf{x} - \text{pos}(P_{di})\| < \|\mathbf{x} - \text{pos}(P_{dj})\|, j = 1, 2, \dots, N, j \neq i\}. \quad (7.5)$$

For notational purposes we have added subscript di to the most distal branches that have no further conducting branches coming from them but instead enter a group of acinar units (approximated by the poroelastic model). In Figure 7.1 we demonstrate how the domain is coupled to the distal branches using a simple 2D example. The discretization of this 2D example is described in section 7.4.1.

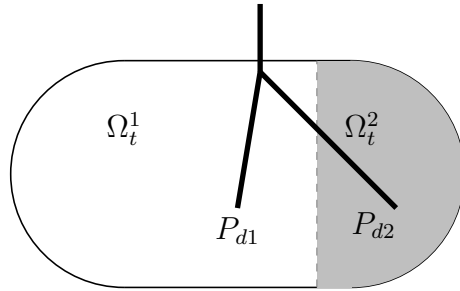


Figure 7.1: A simple example of a 2D domain being split into two subdomains dependent on the position of end points of the fluid network.

We couple the airway network to the poroelastic domain by adding the flow contribution from each distal airway to the poroelastic domain as a source term in the poroelastic mass conservation equation (3.38c), such that

$$\nabla \cdot (\mathbf{v}^s + \mathbf{z}) = Q_{di} \quad \text{in } \Omega_t^i. \quad (7.6)$$

We also couple the airway network to the poroelastic domain by setting the average pressure in the poroelastic domain within Ω_t^i to be the same as the

corresponding distal pressure node P_{di} of the flow segment Q_{di} ,

$$\frac{1}{|\Omega_t^i|} \int_{\Omega_t^i} p = P_{di}, \quad (7.7)$$

where $|\Omega_t^i|$ denotes the volume of the segment Ω_t^i . Equation (7.7) enforces the assumption that the end pressure in a terminal bronchiole is the same as the alveolar pressure in the surrounding tissue.

7.3.3 Summary of the coupled lung model.

To solve the coupled poroelastic-fluid-network lung model we need to find $\chi(\mathbf{X}, t)$, $\mathbf{z}(\mathbf{x}, t)$, $p(\mathbf{x}, t)$, P_i and Q_i such that

$$-\nabla \cdot (\boldsymbol{\sigma}_e - p\mathbf{I}) = \rho \mathbf{f} \quad \text{in } \Omega_t, \quad (7.8a)$$

$$\mathbf{k}^{-1} \mathbf{z} + \nabla p = \rho^f \mathbf{f} \quad \text{in } \Omega_t, \quad (7.8b)$$

$$\nabla \cdot (\mathbf{v}^s + \mathbf{z}) = Q_{di} \quad \text{in } \Omega_t^i, \quad (7.8c)$$

$$\chi = \mathbf{X} + \mathbf{u}_D \quad \text{on } \Gamma_d, \quad (7.8d)$$

$$(\boldsymbol{\sigma}_e - p\mathbf{I})\mathbf{n} = \mathbf{t}_N \quad \text{on } \Gamma_t, \quad (7.8e)$$

$$\mathbf{z} \cdot \mathbf{n} = q_D \quad \text{on } \Gamma_f, \quad (7.8f)$$

$$p = p_D \quad \text{on } \Gamma_p, \quad (7.8g)$$

$$\chi(0) = \mathbf{X} + \mathbf{u}^0, \quad \text{in } \Omega_0, \quad (7.8h)$$

$$P_0 = \hat{P}, \quad (7.8i)$$

$$P_{i,1} - P_{i,2} = R_i Q_i, \quad (7.8j)$$

$$Q_i = \sum_{Q_{i,j} \in Q_i} Q_{i,j}, \quad (7.8k)$$

$$\frac{1}{|\Omega_t^i|} \int_{\Omega_t^i} p = P_{di}. \quad (7.8l)$$

7.4 Implementation

Since the system of equations (7.8) is highly nonlinear, its solution requires a scheme such as Newton's method. In chapter 6 a finite element scheme using Newton's method for the solution of the poroelastic equations valid in large deformations (3.38) has already been presented. In this chapter we adopt the same finite element scheme as presented in chapter 6 for solving the poroelastic equations and expand the linear system (discretized linearization) to include additional matrices required for solving the fluid network and its coupling to the poroelastic medium (equations (7.8c,7.8j,7.8k,7.8l)). This results in a monolithic coupling scheme that ensures good convergence even for problems with strong coupling interactions between the poroelastic medium and the fluid network (see section 7.6.2). For details on how the stiffness matrix \mathbf{K} (discretized linearization of the full lung model (7.8)), and the residual vector \mathbf{R} are built, see section 7.4.2. To solve the nonlinear poroelastic problem using Newton's method at a particular time step, we perform the steps already described in algorithm 2. We set the relative tolerance to be $\text{TOL} = 10^{-4}$. For the subsequent numerical results shown in section 7.6, a maximum of 5 Newton iterations were required to solve each time step.

7.4.1 Discrete coupling of the fluid network to the poroelastic model

If we discretize the space using triangles and employ a piecewise constant pressure approximation (one node at the center of each element), the resulting coupling for the simple 2D example (Figure 7.1) is shown in Figure 7.2a. Once we refine the mesh (Figure 7.2b), the discretized division of subdomains tends to the subdivision of the original problem (Figure 7.1). The i th discretized subdomain Ω_t^i is defined as the set of elements, E , closest to the position of the i th inlet, denoted by $\text{pos}(P_{di})$.

$$\Omega_t^i := \{E \in \Omega_t : \|\text{pos}(P_{di}) - \text{cent}(E)\| < \|\text{pos}(P_{dk}) - \text{cent}(E)\|, k = 1, 2, \dots, N, k \neq i\}, \quad (7.9)$$

where $\text{cent}(E)$ denotes the centroid of an element.

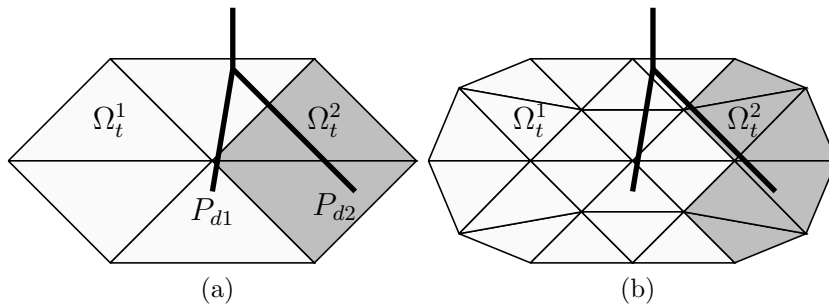


Figure 7.2: (a) Coupling between the discretized domain and the fluid network using a piecewise constant pressure approximation for the example shown in Figure 7.1. (b) Coupling between the discretized domain and the fluid network after mesh refinement.

7.4.2 Finite element matrices

For the fully-coupled large deformation poroelastic fluid network model we need to solve the linear system $\mathbf{K}(\mathbf{u}_i^n)\xi\mathbf{u}_{i+1}^n = -\mathbf{R}(\mathbf{u}_i^n, \mathbf{u}^{n-1})$ at each Newton iteration. This can be expanded as

$$\begin{bmatrix} \mathbf{K}^e & 0 & \mathbf{B}^T & 0 & 0 & 0 & 0 & 0 \\ 0 & \mathbf{M} & \mathbf{B}^T & \mathbf{L}^T & 0 & 0 & 0 & 0 \\ -\mathbf{B} & -\Delta t\mathbf{B} & \mathbf{J} & 0 & 0 & 0 & 0 & -\Delta t\mathbf{G}^T \\ 0 & \mathbf{L} & 0 & 0 & 0 & 0 & 0 & 0 \\ 0 & 0 & 0 & 0 & \mathbf{T}_{11} & \cdots & \cdots & \mathbf{T}_{14} \\ 0 & 0 & 0 & 0 & \vdots & & & \vdots \\ 0 & 0 & 0 & 0 & \mathbf{T}_{31} & \cdots & \cdots & \mathbf{T}_{34} \\ 0 & 0 & \mathbf{G} & 0 & 0 & -\mathbf{X} & 0 & 0 \end{bmatrix} \begin{bmatrix} \xi\mathbf{u}^n \\ \xi\mathbf{z}^n \\ \xi\mathbf{p}^n \\ \xi\mathbf{\Lambda}^n \\ \xi\mathbf{P}^n \\ \xi\mathbf{P}_d^n \\ \xi\mathbf{Q}^n \\ \xi\mathbf{Q}_d^n \end{bmatrix} = -\begin{bmatrix} \mathbf{r}_1 \\ \mathbf{r}_2 \\ \mathbf{r}_3 - \Delta t\mathbf{G}^T\mathbf{Q}_d^n \\ 0 \\ 0 \\ 0 \\ 0 \\ \mathbf{G}\mathbf{p}^n - \mathbf{X}\mathbf{P}_d^n \end{bmatrix},$$

where we have defined the following matrices and vectors:

$$\mathbf{K}^e = [\mathbf{a}_{kl}], \quad \mathbf{k}_{kl}^e = \int_{\Omega_t} \mathbf{E}_k^T \mathbf{D}(\mathbf{u}_i^n) \mathbf{E}_l + (\nabla \boldsymbol{\phi}_k)^T \boldsymbol{\sigma}_e(\mathbf{u}_i^n) \nabla \boldsymbol{\phi}_l \, dv,$$

$$\mathbf{M} = [\mathbf{m}_{kl}], \quad \mathbf{m}_{kl} = \int_{\Omega_t} \mathbf{k}^{-1}(\mathbf{u}_i^n) \boldsymbol{\phi}_k \cdot \boldsymbol{\phi}_l \, dv,$$

$$\mathbf{B} = [\mathbf{b}_{kl}], \quad \mathbf{b}_{kl} = - \int_{\Omega_t} \psi_k \nabla \cdot \boldsymbol{\phi}_l \, dv,$$

$$\mathbf{J} = [\mathbf{j}_{kl}], \quad \mathbf{j}_{kl} = \delta \sum_K \int_{\partial K \setminus \partial \Omega_t} h_{\partial K}[\psi_k][\psi_k] \, ds.$$

$$\begin{aligned}\mathbf{r}_1 &= [\mathbf{r}_{1i}], \quad \mathbf{r}_{1i} = \int_{\Omega_t} (\boldsymbol{\sigma}_e(\mathbf{u}_i^n) - p_i^n \mathbf{I}) : \nabla \phi_i - \rho(\mathbf{u}_i^n) \phi_i \cdot \mathbf{f} \, dv - \int_{\Gamma_t} \phi_i \cdot \mathbf{t}_N \, ds, \\ \mathbf{r}_2 &= [\mathbf{r}_{2i}], \quad \mathbf{r}_{2i} = \int_{\Omega_t} \mathbf{k}^{-1}(\mathbf{u}_i^n) \phi_i \cdot \mathbf{z}_i^n - p_i^n \nabla \cdot \phi_i - \rho^f(\mathbf{u}_i^n) \phi_i \cdot \mathbf{f} \, dv,\end{aligned}$$

$$\begin{aligned}\mathbf{r}_3 &= [\mathbf{r}_{3i}], \quad \mathbf{r}_{3i} = \int_{\Omega_t} \psi_i \nabla \cdot (\mathbf{u}_i^n - \mathbf{u}^{n-1}) + \Delta t \psi_i \nabla \cdot \mathbf{z}_i^n - \Delta t \psi_i g \, dv \\ &\quad + \delta \sum_K \int_{\partial K \setminus \partial \Omega_t} h_{\partial K}[\psi_i] [p_i^n - p^{n-1}] \, ds.\end{aligned}$$

$$\mathbf{L} = [\mathbf{l}_{ij}], \quad \mathbf{l}_{ij} = \int_{\Omega} \epsilon_i \phi_j \cdot \mathbf{n},$$

$$\begin{aligned}\mathbf{X} &= [\mathbf{x}_{ij}], \quad \mathbf{x}_{ij} := \begin{cases} 1 & \text{if } ||\text{pos}(P_{di}) - \text{cent}(E_j)|| < ||\text{pos}(P_{dk}) - \text{cent}(E_j)||, k = 1, 2, \dots, N, k \neq i, \\ 0 & \text{otherwise,} \end{cases} \\ \mathbf{G} &= [\mathbf{g}_{ij}], \quad \mathbf{g}_{ij} = \int_{\Omega} \mathbf{x}_{ij} \frac{\phi_j}{|E_j|},\end{aligned}$$

\mathbf{T} represents the matrix entries required for the fluid network.

Here $\boldsymbol{\epsilon}_k$ are scalar valued linear basis functions such that the Lagrangian multiplier vector at the i th iteration can be written as $\boldsymbol{\Lambda}_i^n = \sum_{k=1}^{n_{\Lambda}} \boldsymbol{\Lambda}_{i,k}^n \boldsymbol{\epsilon}_k$, and $\text{cent}(E_j)$ denotes the centroid of the j th element. All other terms have already been defined in section 6.4.1.

7.5 Model generation

7.5.1 Mesh generation

We derive a whole organ lung model, of the right lung, from a high-resolution CT image taken at total lung capacity (TLC) and functional residual capacity (FRC). The bulk lung is first segmented from the CT data (slice thickness and pixel size 0.73 mm) using the commercially available segmentation software Mimics¹. We then use the open-source image processing toolbox iso2mesh [34] to generate a Tetrahedral mesh containing 38369 elements. The conducting airways are also segmented from the CT data taken at TLC level, and a centerline with radial information is calculated. To approximate the remaining airways up to generation 8-13 we use a volume filling airway generation algorithm to generate a mesh of the airway tree containing 13696 nodes, with 2140 terminal branches [17].

7.5.2 Reference state, boundary conditions and initial conditions

The poroelastic framework we have described requires a stress free reference state. Biological tissues do not possess a ‘reference state’ in space where the material is free of both stress and strain. The cells that make up tissues are born into stressed states and live out their lives in these stressed states [37].

¹<http://biomedical.materialise.com/mimics>

In this work, we scale the lung from FRC to a configuration, the reference state, in which the internal stresses and strains are assumed to be zero. The geometry of the reference state is then used as the initial configuration of the lung model. The lung model is then uniformly inflated from the reference state to create a pre-stressed FRC configuration which has a mean elastic recoil of about 0.49×10^3 Pa, commonly understood to be a typical value [101]. From there we simulate tidal breathing. A similar approach has also been used in [61].

We register the expiratory (FRC) segmentation to the segmentation at TLC using a simple registration procedure that uses three scalings in the x , y and z direction to map between the bounding boxes of the segmentations at FRC and TLC. This yields a rough estimate of the deformation field for the lung surface from expiration to inspiration. To simulate tidal breathing we assume a sinusoidal breathing cycle and expand the lung surface from FRC to 40% of the deformation from FRC to TLC,

$$\mathbf{u}_D(t) = 0.2 \left(1 + \sin \left(\frac{t\pi}{2} + \frac{3\pi}{2} \right) \right) \mathbf{u}_{D,TLC} \quad \text{on } \Gamma_d. \quad (7.10)$$

Here $\mathbf{u}_{D,TLC}$ is the deformation of the lung surface from FRC to TLC, obtained using the registration procedure. For our mesh and registration this results in a physiologically realistic tidal volume of 0.59 liters. We simulate breathing for a total of 8 seconds (2 breathing cycles) resulting in a breathing frequency of 15 breaths per minute. Due to the incompressibility of the

poroelastic tissue this also determines the total volume of air inspired/expired and the flowrate at the trachea, see Figure 7.4a and 7.4b respectively. For the fluid boundary condition we have that the whole lung is sealed so that no fluid can escape through the lung surface, with $\mathbf{z} \cdot \mathbf{n} = 0$ along the whole boundary. For the airway network boundary condition we set the outlet pressure of the airway network to zero atmospheric pressure, $P_0 = 0$.

7.5.3 Simulation parameters

Several parameters for lung tissue elasticity and poroelasticity have been proposed [31, 58, 75, 100, 111]. There is no consensus in the values in the literature. In this study we have chosen parameters from the literature, as shown in Table 7.1. These parameters are within range of existing models, and result in physiologically realistic simulation results (see section 7.6).

Parameter	Value	Reference
ϕ_0	0.99	[58]
κ_0	$10^{-5} \text{ m}^3 \text{ s kg}^{-1}$	[58]
E	$0.73 \times 10^3 \text{ Pa}$	[31]
ν	0.3	[31]
μ_f	$1.92 \times 10^{-5} \text{ kg m}^{-1} \text{ s}^{-1}$	[89]
T	8s	-
Δt	0.2s	-
δ	10^{-5}	-

Table 7.1: Parameters for breathing simulations.

7.6 Model exploration

We will now explore the behavior of the proposed model using a series of simulations to investigate the coupling between the airways and the tissue, hysteresis effects and how mass is conserved within the tissue.

In the subsequent analysis the total and elastic stress is calculated as $\sqrt{\lambda_1^2 + \lambda_2^2 + \lambda_3^2}$, where $\lambda_1, \lambda_2, \lambda_3$ are the three eigenvalues of the stress tensor, respectively. We define the relative Jacobian, denoted by J_V , as a measure for ventilation, which is calculated to be the volume ratio between the current state and FRC, i.e., $J_V = J/J_{FRC}$, and is a direct measure of tissue expansion. By running simulations over many breaths we have found that differences between the second breath and subsequent breaths were negligible, and therefore only results from the second breath, $t = 4s$ to $t = 8s$ are presented. The sagittal slice shown in Figure 7.3a gives a good representation of the general dynamics within the tissue. Unless otherwise stated, all subsequent figures that do not show time courses are taken at $t = 5.8s$ just before peak inhalation of the second time breath the simulation.

7.6.1 Normal breathing

To simulate tidal breathing we apply the boundary conditions and simulation parameters previously discussed in sections 7.5.2 and 7.5.3, respectively.

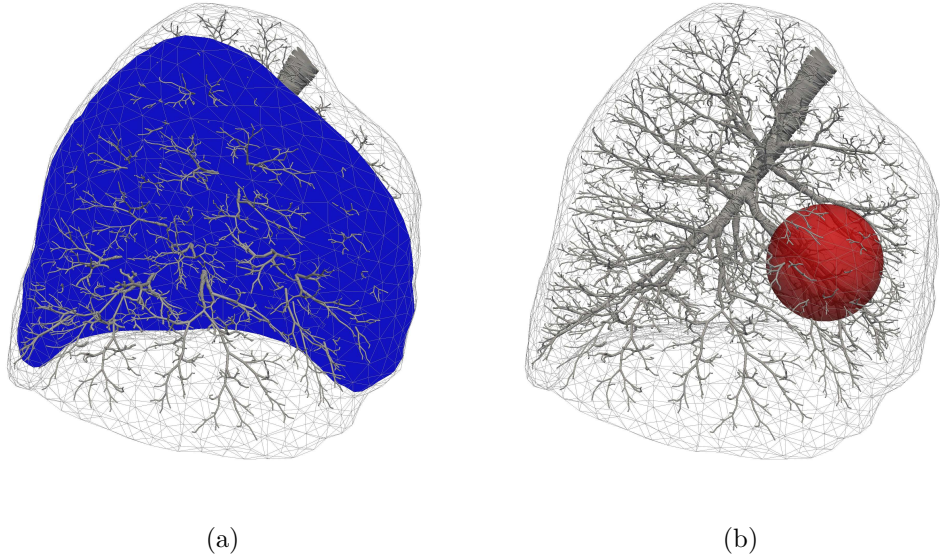


Figure 7.3: (a) The blue sagittal slice indicates the position of subsequent slices used for the data analysis of the tissue. (b) The red ball represents the structurally modified region, used to prescribe airway constriction and tissue weakening.

Lung volume, flow and pressure drop

Figure 7.4 details the lung tidal volume, flow rate and pressure drop obtained from simulations of tidal breathing. Due to the incompressibility of the poroelastic medium and the fixed nature of the airway network, the lung tidal volume (Figure 7.4a) and flow rate (Figure 7.4b) follow a sinusoidal pattern that matches the form of the deformation boundary condition prescribed by equation (7.10). The mean pressure drop of the airways, is shown in Figure 7.4c, and agrees with previous simulation studies on full airway trees [49, 89].

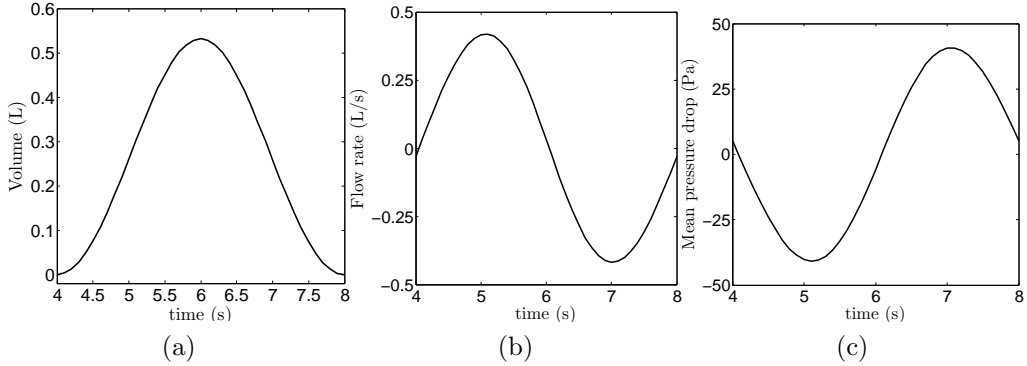


Figure 7.4: Simulated natural tidal breathing: (a) lung tidal volume (volume increase from FRC), (b) flow rate at the inlet, (c) mean pressure drop from the inlet to the most distal branches.

Pathway resistance

The pathway resistance (Poiseuille flow resistance) from the inlet (right bronchus) to each terminal airway is shown in Figure 7.5a for the whole tree. In Figure 7.5b we show the pathway resistance of the terminal airways mapped onto the tissue.

Airway tree-tissue coupling

In order to quantify the contribution of airway resistance to tissue expansion (ventilation), measured by J_V , the correlations between pathway resistance in the tissue and J_V are plotted for each element in Figure 7.6a. There is a clear correlation between pathway resistance and tissue expansion, as is expected since the elastic coefficients are constant throughout the lung model. The Pearson correlation coefficient is -0.55 , hence ventilation decreases as path-

way resistance increases, with a p-value < 0.0001. Figure 7.6b shows there is also a strong correlation between the pathway resistance and pressure in the poroelastic tissue. Here the Pearson correlation coefficients is also -0.55 , and pressure decreases (becomes more negative) with pathway resistance, with a p-value < 0.0001. Note that for a very few regions that are coupled to terminal branches with a low pathway resistance, positive pressures are possible. This results in a pressure gradient that pushes fluid from these well ventilated regions to neighbouring less ventilated regions (collateral ventilation). The distribution of pressure in the airway tree is shown in Figure

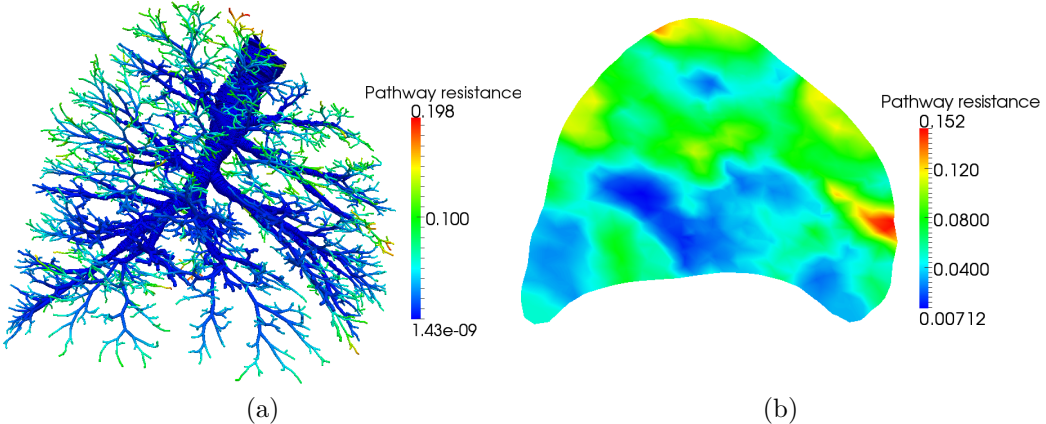


Figure 7.5: (a) Pathway resistance ($\text{Pa mm}^{-3}\text{s}$) from the inlet to the terminal branches in the airway tree. (b) Pathway resistance mapped onto a slice of tissue. The deformation of both the tree and the tissue in this figure correspond to the reference configuration.

7.7a and the pressure inside the poroelastic tissue is shown in Figure 7.7b. Figure 7.7c shows the pressure on the lung surface. The patchy pressure field is well approximated by the piecewise constant pressure elements employed

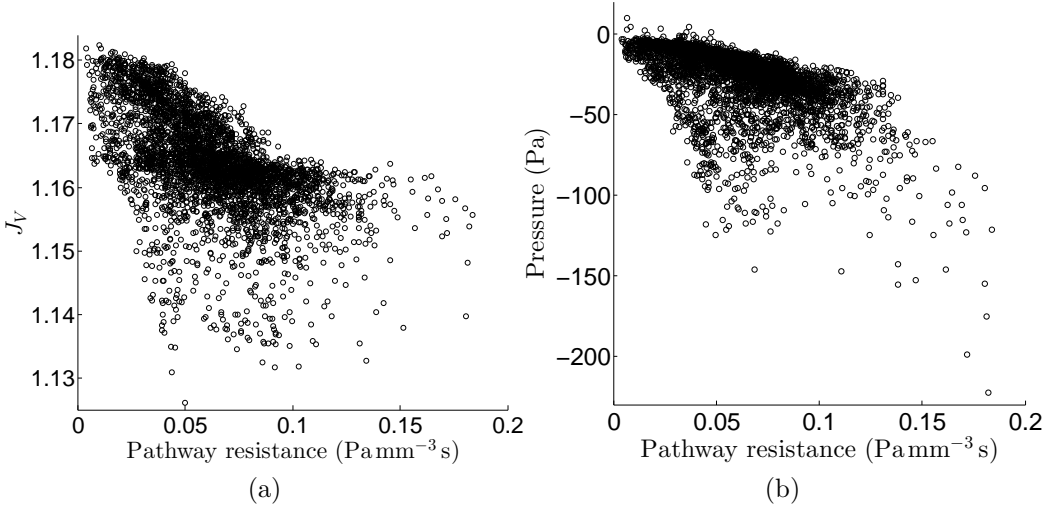


Figure 7.6: (a) Correlation between tissue expansion (ventilation) and resistance of the pathways from the inlet to the terminal branch. (b) Correlation between pressure in the poroelastic medium (alveolar pressure) and pathway resistance.

by the finite element method used to solve the poroelastic equations. Figure 7.7d shows the distribution of tissue expansion. Despite the heterogeneity in the airway tree the variations in tissue expansion are quite small, since the elastic coefficients are constant throughout the computational domain.

7.6.2 Breathing with airway constriction

We now simulate localized constriction of the airways by reducing the radii of the lower airways (with radius less than 4mm) within a ball near the right middle lobe. This region is represented by a red ball in Figure 7.3b. We reduce the radius of the aforementioned lower airways by 0%, 40%, 50%, 60% and 65%. This corresponds to a mean pathway resistance within the ball

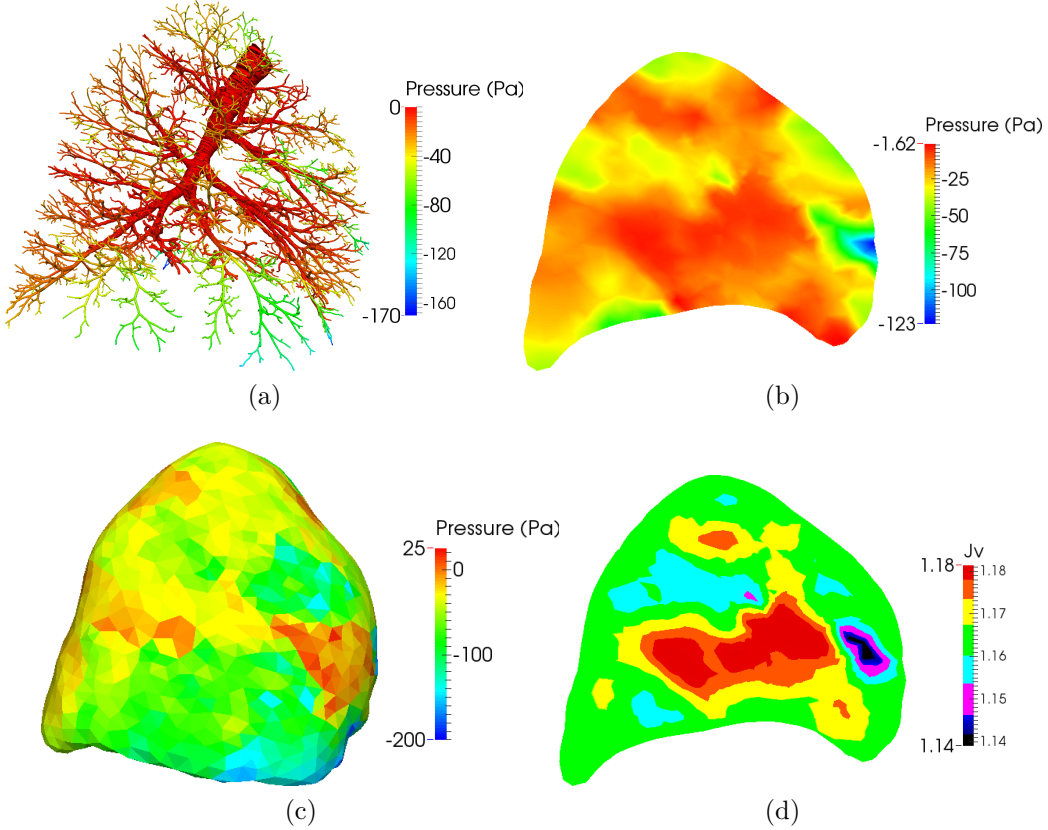


Figure 7.7: (a) Pressure in the airway tree. (b) Sagittal slice showing pressure in the tissue using a linear interpolation. (c) Pressure on the lung surface. (d) Sagittal slice showing tissue expansion from FRC.

of $0.0507, 0.112, 0.188, 0.399$ and $0.651 \text{ Pa mm}^{-3}\text{s}$, respectively. Figure 7.10 shows the changes in variables of physiological interest within the ball as the pathway resistance increases. The amount of tissue expansion during inspiration decreases as the airways become constricted (airway radius decreases and pathway resistance increases), as shown in Figure 7.8a. This is due to the reduced amount of flow in these airways. Further, the standard deviation increases because the pathway resistance of each branch increases

by a different amount, depending on its original length and radius. Long and narrow branches will be affected most by the constriction. The pressure decreases with increasing pathway resistance as shown in Figure 7.8b, since a larger pressure drop is needed to force the air down the constricted branches. Figure 7.8c shows the elastic stress in the tissue decreases as pathway resistance increases due to the decrease in tissue deformation (strain). However, as seen in Figure 7.9c, a large elastic stress appears near the boundary of the constricted region where the tissue is expanded by the surrounding tissue..

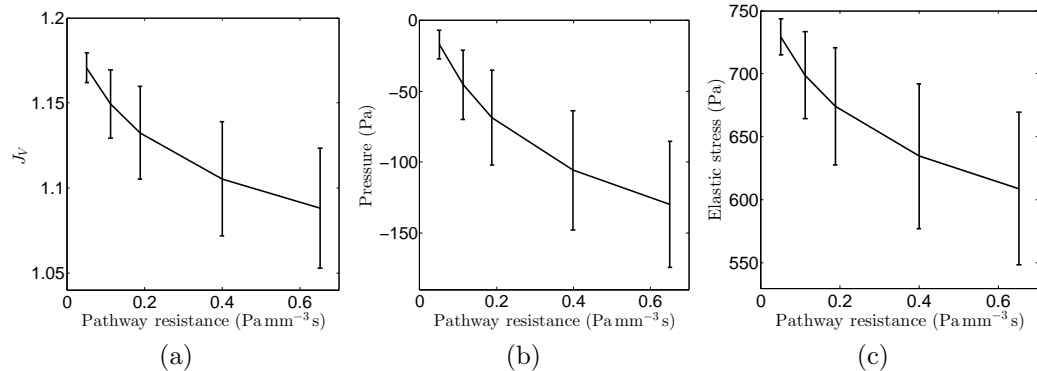


Figure 7.8: (a) Mean and standard deviations of the relative Jacobian from FRC, (b) pressure in the tissue and (c) elastic stress are plotted against increasing pathway resistance within the structurally modified region.

The simulations results shown in Figure 7.9 were performed with 65% airway constriction in the lower airways, applied within the structurally modified region. The volume conserving property (mass conservation) of the method is illustrated in Figure 7.9b where the tissue surrounding the constricted area is expanding to compensate for the reduction of tissue expansion due to the constriction within the structurally modified region. Figure 7.9a

shows an increase in pressure near the boundary of this region. This facilitates a pressure gradient that allows for air to flow into the constricted region (collateral ventilation) to partially compensate for the reduced amount of ventilation, as is shown in Figure 7.9d. The magnitude of the maximum flow within the tissue is $8 \times 10^{-4} \text{ ms}^{-1}$, this is quite small and is due to the low permeability applied homogeneously within the model.

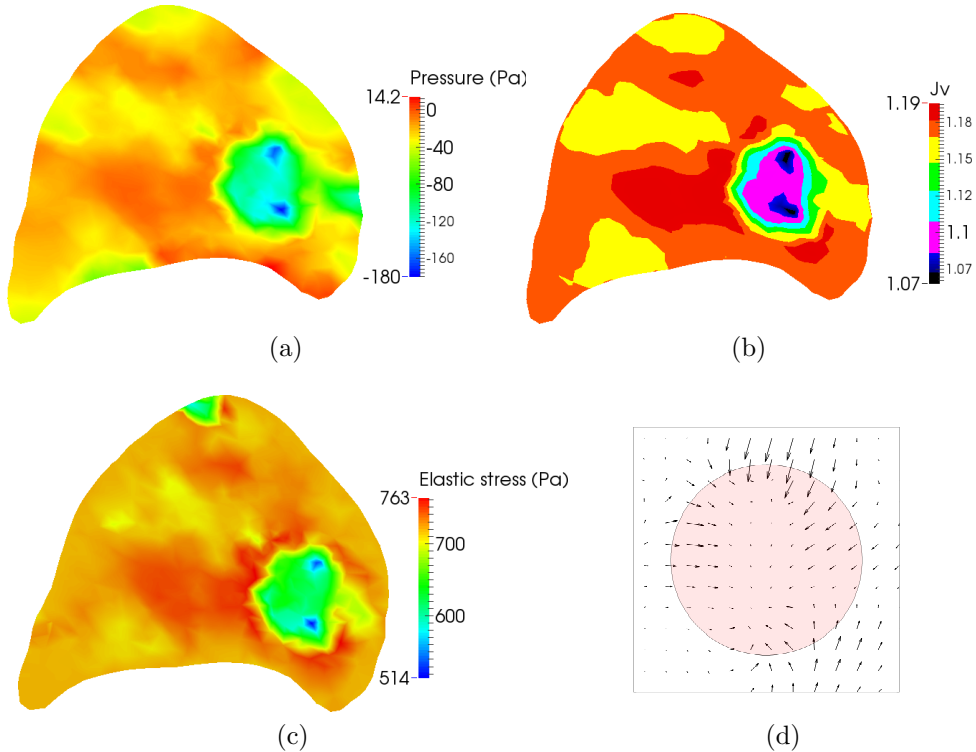


Figure 7.9: (a) Sagittal slices showing the elastic stress, (b) Relative Jacobian, (c) pressure and (d) direction of the fluid flux near the structurally modified (constricted) region.

7.6.3 Breathing with locally weakened tissue

We now simulate localized weakening of the tissue by reducing the Young's modulus of the tissue within the structurally modified region represented by the red ball in Figure 7.3b. We reduce the Young's modulus by 0%, 50%, 75% and 90%. This corresponds to a modified Young's modulus of 730, 365, 182.5 and 73 Pa, respectively. Figures 7.10a-7.10c plot J_V , the pressure and the elastic stress in within the modified region. As expected the local expansion increases as the tissue weakens, and the elastic stress decreases. Note that in all cases the range (heterogeneity) of local ventilation, pressure and elastic stress within the modified region increases dramatically as the stiffness of the modified region decreases.

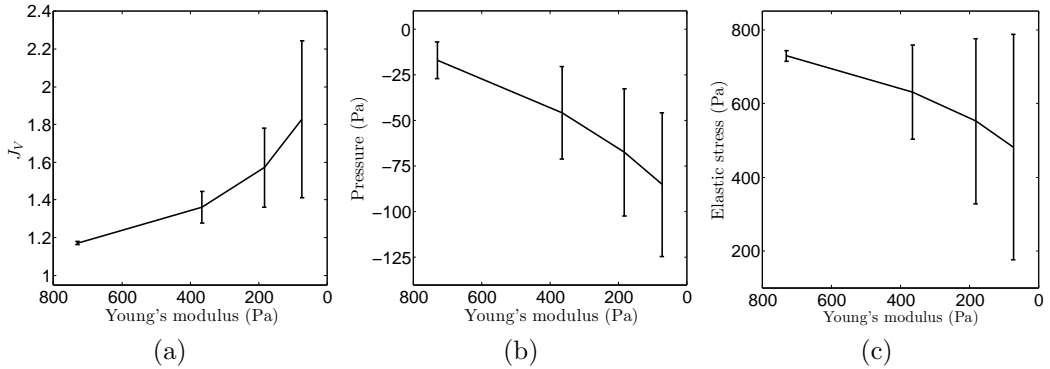


Figure 7.10: (a) Mean and standard deviations of the relative Jacobian from FRC, (b) pressure in the tissue and (c) elastic stress are plotted against Young's modulus within the structurally modified region.

Due to the large amount of tissue expansion within the structurally modified region, the tissue immediately surrounding this region is effectively squeezed between the expanded modified region and the surrounding tissue

and as a result, expands the least as seen in Figure 7.11.

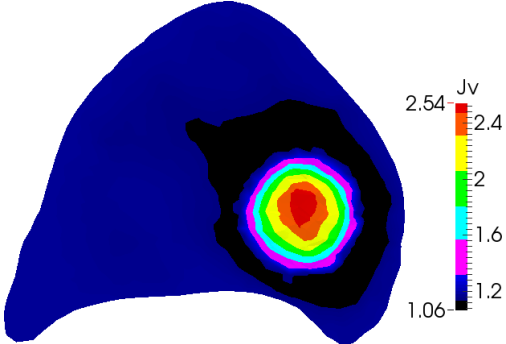


Figure 7.11: Slice showing the amount of tissue expansion (J_V) from FRC during inspiration with 90% localized tissue weakening.

7.6.4 Dynamic hysteresis

With the current choice of hyperelastic strain energy law (7.2) for the tissue mechanics, our model does not produce classic hysteresis effects, often attributed to surface tension within lung tissue [56]. However, we are able to produce dynamic hysteresis effects, caused by delayed emptying and filling of parts of the lung.

Figure 7.12 shows the change in elastic recoil (total stress) with volume throughout the breathing cycle for three different breathing rates. This curve is commonly known as a dynamic pressure-volume (PV) curve, and shows the amount of dynamic hysteresis in the system. We will now explain the main features of this curve.

Figure 7.13a and 7.13b both show the distribution of pressure against pathway resistance within the tissue, shortly after inhalation. At this point

the lung as a whole has started to exhale air. However some segments of the tissue have a negative pressure and are still filling up. These parts of the lung also tend to have a higher pathway resistance associated with them, which can explain the delayed filling. The reason that these parts of the lung continue to fill up, even during expiration, is that the continuum mechanics model of the tissue aims to achieve an energy minimum where the tissue is inflated evenly throughout the lung, thus pulling open delayed segments of tissue. This is because the elasticity coefficients of the tissue have been parametrized homogeneously for these simulations. These negative pressures in the tissue, due to the delayed filling of parts of the lung, result in a larger total stress (elastic recoil), given by $\sigma = \sigma_e - p\mathbf{I}$. This effect is especially noticeable when transitioning from inspiration to expiration (and vice versa), causing the curve to shift right when moving from inspiration to expiration (due to delayed filling) and left when moving from expiration to inspiration (due to delayed emptying).

Also, we can clearly see an increase in the heterogeneity of the tissue's pressure distribution with increased breathing rate when comparing Figures 7.13a and 7.13b, for a four second and a one second breathing cycle, respectively. This increase in pressure heterogeneity is caused by the increased flow rates within the tree, and results in an increase in total stress. Therefore, a faster breathing rate causes an increasing amount of hysteresis (widening of the dynamic PV curve in Figure 7.12).

The increase of hysteresis in the dynamic PV curve and its shift as the

breathing rate increases agrees with findings in the literature [44, 84]. In the literature, hysteresis associated with dynamic PV curves is mostly hypothesized to be caused by flow-dependent resistances, pendelluft effects, chest wall rearrangement, and recruitment and derecruitment of lung units [2, 44, 82]. Dynamic hysteresis has also been shown to exist in balloon type lung models [49].

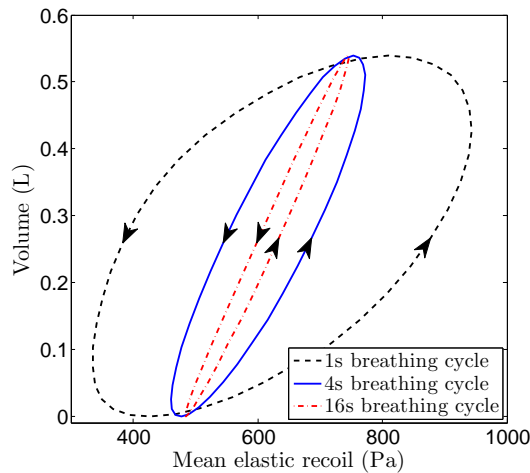


Figure 7.12: Dynamic pressure-volume curve: mean elastic recoil (total stress) against lung tidal volume during one full breathing cycle, for three different breathing rates. The arrows indicate the direction of time during the breathing cycle.

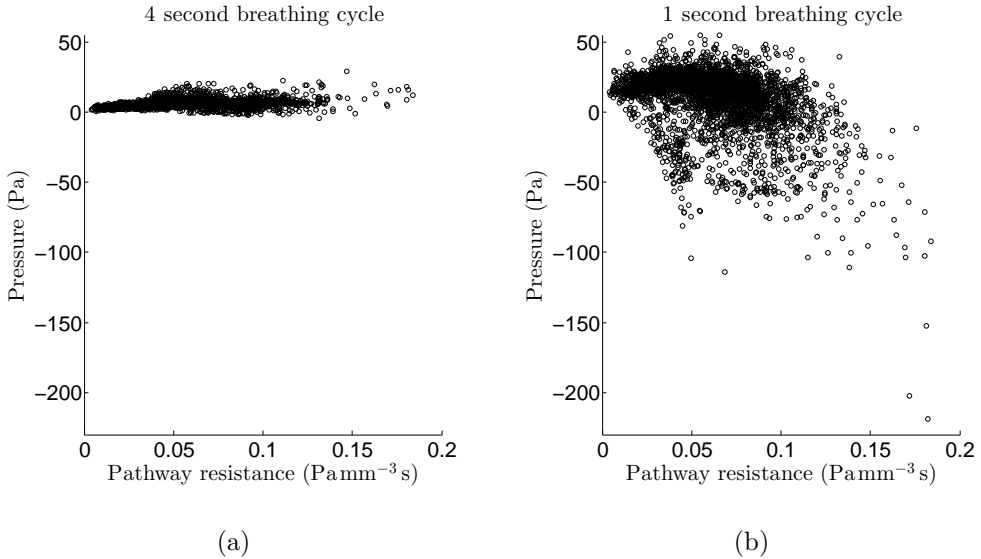


Figure 7.13: (a) Pathway resistance against pressure with a 4 second breathing cycle, 0.2 seconds after peak inhalation. (c) Pathway resistance against pressure with a 1 second breathing cycle, 0.05 seconds after peak inhalation.

7.7 Discussion

We have presented a mathematical model of the lung that tightly couples tissue deformation with ventilation using a poroelastic model coupled to a fluid network model. We have highlighted the assumptions necessary to arrive at such a model, and outlined its limitations. In comparison with previous ventilation models, the current approach models the tissue as a continuum and is therefore able to regionally conserve mass (which means conserve volume as the solid skeleton and fluid are both incompressible), and to model collateral ventilation. Further it is driven by deformation boundary conditions

extracted from imaging data to avoid having to prescribe a pleural pressure which is impractical to be measured experimentally. In simulations of normal breathing, the model is able to produce physiologically realistic global measurements and dynamics. In simulations with altered airway resistance and tissue stiffness, the model illustrates the interdependence of the tissue and airway mechanics and thus the importance of a fully coupled model.

7.7.1 Contributors of airway resistance and tissue mechanics to lung function

We have found that there is a strong correlation between airway resistance and ventilation, see Figure 7.6a. Also, due to heterogeneity in airway resistance, hysteresis effects appear during breathing (Figure 7.12) and result in a complex ventilation distribution, caused by delayed filling and emptying of the tissue. Due to the Poiseuille law that governs the flow through the airways, small changes in airway radii can result in large changes in pathway resistance, which in turn can significantly affect the results of the coupled model. Thus, parametrizing the airways correctly is very important. However this is notoriously difficult since CT data is only available down to the 5-6th generation, and small errors and biases in the segmentation, that get propagated by the airway generation algorithm, can have large influences in determining the simulation results. Changes in tissue elasticity coefficients also play an important role in determining the function of the lung model.

This has been demonstrated in section 7.6.3 where a reduction in the Young's modulus within a specified region causes significant changes in ventilation, pressure and stress.

7.7.2 Limitations and future work

In order to move towards a more realistic model of the lung breathing, many steps need to be taken. We will list the main limitations that exist in the airway tree model, the poroelastic model, the boundary conditions and the geometry, and give indications on how these could be addressed in a future model.

Airway tree limitations: (1) The airway tree flow model currently implemented makes the Poiseuille flow assumption for the whole tree. The Poiseuille flow assumption requires flow to be fully developed and laminar. This may be true for the smaller airways where the Reynolds number is small but is certainly false for the larger upper airways where high Reynolds number flows occur. Such a model will therefore not be able to capture the high Reynolds number flows and turbulent effects that are known to exist in the upper airways. This could be improved by modifying the airway resistance at different generations according to the Reynolds number [77, 89]. Further improvements could be made by using a more sophisticated flow model for the airways, such as the 3D-0D model presented in [49]. (2) The coupling of each terminal branch to the tissue currently assumes that there is no added resistance to air flowing from the terminal branch to each alveolar unit within

the tissue. This could be improved by adding a simple resistive (impedance) model considering the volume of tissue that the terminal branch is feeding. This would also slightly increase the mean pressure drop of the lung model.

(3) At the moment the airway tree is assumed to be static, and its configuration is not influenced by the deformation and stresses in the tissue. This could be improved by modelling the interaction of stresses and strains on the airway wall, opening up the airways during inspiration.

Poroelastic tissue limitations: (1) We have assumed a Neo-Hookean law for strain energy law to make the interpretation of the elasticity constants and dynamics of the model as simple as possible. However lung parenchyma is known to follow an exponential stress-strain relation, especially past tidal volume, where a law such as the one proposed by [38] might be more appropriate. Also little is known about the form of the strain-energy law during disease (e.g. fibrosis or emphysema). Similarly, for the permeability law little is known about its form for healthy or diseased tissue. Further experiments and modelling investigation would be needed to develop these. (2) Currently the tissue has been parameterized homogeneously to simplify the analysis of the results. Density information from CT images could be used to parameterize the initial porosity and elasticity coefficients. (3) We have ignored the effect of blood in the tissue. The inertia and gravity forces of blood acting on the tissue could be of importance when predicting deformation and ventilation in the lung. Due to the modular framework of the poroelastic theory it should be possible to include blood as a separate phase in a future version of

the model. A vascular tree could also be generated from CT images and coupled to the poroelastic medium. (4) The airflow within the poroelastic tissue has been assumed to be inviscid. However, if we were to consider diseased states such as emphysema, where large areas of lung tissue completely break down leaving big holes, it could be argued that viscous forces could well play an important role, making it important to include them in our model. In a future version of the model the Darcy flow model could be replaced with a Brinkman, or even a Stokes flow model for big holes.

Boundary condition limitations: (1) The current registration should be updated to a more sophisticated non-linear registration algorithm (e.g. [46, 50, 109]) that is able to account for the complicated deformation of the lung surface during breathing. (2) It is known that the lung surface is able to slide freely within the plueral cavity. This feature could be implemented using methods already presented in [56] and [8].

Geometry limitations: (1) To model the complete organ and give a more accurate pressure drop, both the right and left lung, and the trachea and mouth should be included. (2) The airway tree generated in this work goes down to generations 8-13. More generations should be added to result in a fuller and more realistic tree. This would also require a finer mesh to approximate the lung tissue to resolve the coupling between each terminal branch and a subregion of lung tissue. (3) Cavities in the lung parenchyma due to large airways are currently not accounted for, i.e. it is assumed that the volume occupied by the airways is zero. To improve on this, a mesh of the

lung with the larger upper airways removed would need to be generated. This new mesh could also incorporate a model of the cartilage found in the upper airways. (4) Additional no-flux boundaries should be introduced to represent the well defined and thought to be impermeable boundaries, between lobes (fissures) and lung segments.

7.8 Conclusion

The model presented in this chapter can be used to investigate mechanical problems dependent on coupled deformation and ventilation in the lung. The numerical simulations are shown to be able to reproduce global physiologically realistic measurements. A fully nonlinear formulation permits the inclusion of various constitutive models, allowing investigation into different diseased states during various breathing conditions. A finite element method has been used to discretize the equations in a monolithic way to ensure convergence of the nonlinear problem, even under strong poroelastic-fluid-network coupling conditions. Due to the flexibility of the model, further improvements in its physiological accuracy are possible. It is hoped that the model presented here can form the basis for studies on the importance of airway and tissue heterogeneity on lung function, testing of mechanical hypothesis for the progression of disease, and investigations into phenomena such as hyperinflation, fibrosis and constriction.

Chapter 8

Conclusion

8.1 Review and remarks

In this Thesis, we presented a novel finite element method for solving the poroelastic equations valid in small and large deformations. We also presented a mathematical (poroelastic) model of lung parenchyma that is coupled to a fluid network, modelling the airway tree. To the best of our knowledge, this is the first computational lung model built from patient specific imaging data that is able to capture the tight coupling between the tissue deformation and ventilation, seen in Chronic Obstructive Pulmonary Diseases (COPD), such as emphysema. Numerical software to simulate the lung model on patient specific lung geometries, extracted from imaging data has been implemented, and preliminary simulation results show physiologically realistic phenomena. A detailed summary of the main contributions of each

chapter has already been given in section 1.3.

It has not been straightforward to arrive at the final formulation of the proposed stabilized finite element method. Only by performing detailed analysis of the error and stability of the discretized formulation were we able to determine the correct form of the stabilization term that led to a stable and optimally converging method. This highlights the importance of rigorous analysis and testing when developing new numerical schemes. The proposed stabilization performs well for various test problems, for both small and large deformations. A particular nice feature is that in three dimensions only a very small value for δ , the stabilization parameter, is required to yield a stable solution, thus rendering the added mass effect of the stabilization term negligible. This along with the method's simplicity compared to discontinuous and nonconforming finite element methods makes its implementation very appealing.

The computational lung model outlined in this thesis appears to be a valid tool for solving the mechanical problem of tightly coupling lung deformation and ventilation during normal breathing and breathing with disease. We hope that due to the flexibility of the model, further improvements in its physiological accuracy, as outlined in section 7.7.2, will be made to yield an accurate whole organ lung model.

8.2 Future work

There are several areas which might pose interesting future research problems. These areas fall outside the range of coverage here, but provide interesting challenges nonetheless.

8.2.1 Numerics

Preconditioning: By moving towards solving the poroelastic equations on more detailed 3D geometries the resulting linear system can grow to have several million degrees of freedom. For such problems direct solvers become impractical. To ensure robust and fast convergence of iterative methods such as MINRES, we need to precondition the linear system. An effective preconditioner for solving the Stokes problem using stabilized $P1 - P0$ elements has already been proposed in [87, 98]. This block preconditioning approach could be extended to the three-field poroelasticity case.

A-priori error analysis: A-priori error estimates could be derived for the finite element formulation of the linear porelasticity problem, which could be used for adaptive mesh refinement in space and time.

Nonlinear elasticity: There is a growing need for finite element methods of elasticity to capture steep pressure gradients due to material changes. For example changes in tissue types (fat, muscle and skin) when modelling

the breast. To our knowledge there are currently no available finite element methods that use a simple to implement, low-order (discontinuous pressure) approximation to solve the incompressible nonlinear elasticity equations. It would be straightforward to extend the low-order method of nonlinear poroelasticity to incompressible nonlinear elasticity.

8.2.2 Applications

Validation: For this model to be of practical use it is crucial that it is properly validated, this can be achieved by making use of different imaging modalities and phantom studies where model predictions can be tested. Computed tomography and 4D (dynamic) Magnetic resonance imaging (MRI) can be used to track displacements and calculate volume changes of lung structures. MRI of gases such as Hyperpolarized Xenon [51] and Helium 3 can be used to infer the flow and diffusion of gases, and with the use of elastography we are able to image stiffness and strain of lung tissue. Recently there has also been development in using Hyperpolarized Helium 3 MRI to estimate flow velocities and thus calculate pressure gradients [76].

Lung volume reduction surgery: For patients with severe emphysema invasive surgical procedures such as lung volume reduction surgery (LVRS) and endobronchial valve placement are possible treatments. During LVRS part of the lung is excised in order to improve the configuration of the thoracic cavity, improve elastic recoil, and allow for improved lung inflation of the

remaining and presumably better preserved tissue [30]. Due to the high post-surgery mortality rate of around 5 – 10 percent for LVRS and the fact that only some patients show an improvement with this therapy it is currently extremely challenging for doctors to select patients that will benefit from this invasive surgery. Boundary conditions allowing the lung surface to slide along the pleural cavity would have to be implemented, to allow for the removal of whole lobes in the model. A successful computational lung model would predict how much a particular patient will benefit from this high risk treatment, and help clinicians decide whether or not to perform surgery.

In addition to this various minimally invasive bronchoscopic approaches that also try to cure hyperinflation are being investigated. These include valves that reduce the flow of air into the treated lobe during inspiration, stents that keep communications between pulmonary parenchyma and the segmental airways open, and lung volume reduction coils that aim to cause parenchymal compression and reduces the size of the hyperinflated tissue. More investigation into these techniques and which patients are best suited for a particular treatment is needed. A further developed computational lung model could be used to investigate these approaches and help surgeons plan for surgery by trialing different approaches *in silico* before the operation.

Modelling other organs: Finally, the proposed methodology could also be adapted to model other biological tissues where blood vessels flow through

and interact with a deforming tissue. For example, when modelling perfusion of blood flow in the beating myocardium [23, 26], modelling brain oedema [66] or hydrocephalus [105], or microcirculation of blood and interstitial fluid in the liver lobule [62].

Appendix A

Appendix

A.1 Spatial tangent modulus

The spatial tangent modulus, fourth-order tensor, can be written as (see [16, section 5.3.2] and [48, section 6.6])

$$\Theta_{ijkl} = \frac{1}{J} F_{il} F_{jJ} F_{kK} F_{lL} \mathbf{C}_{IJKL}, \quad (\text{A.1})$$

where \mathbf{C} is the associated tangent modulus tensor in the reference configuration, given by

$$\mathbf{C}_{IJKL} = \frac{4\partial^2 W}{\partial C_{IJ}\partial C_{KL}} + pJ \frac{\partial C_{IJ}^{-1}}{\partial C_{KL}}. \quad (\text{A.2})$$

A.2 Matrix Voigt notation

To ease the implementation of the spatial tangent modulus we make use of matrix voigt notation. The matrix form of Θ is given by D , which can be written as (see [16, section 7.4.2])

$$D = \frac{1}{2} \begin{pmatrix} 2\Theta_{1111} & 2\Theta_{1122} & 2\Theta_{1133} & \Theta_{1112} + \Theta_{1121} & \Theta_{1113} + \Theta_{1131} & \Theta_{1123} + \Theta_{1132} \\ & 2\Theta_{2222} & 2\Theta_{2233} & \Theta_{2212} + \Theta_{2221} & \Theta_{2213} + \Theta_{2231} & \Theta_{2223} + \Theta_{2232} \\ & & 2\Theta_{3333} & \Theta_{3312} + \Theta_{3321} & \Theta_{3313} + \Theta_{3331} & \Theta_{3323} + \Theta_{3332} \\ & & & \Theta_{1212} + \Theta_{1221} & \Theta_{1213} + \Theta_{1231} & \Theta_{1223} + \Theta_{1232} \\ & \text{sym.} & & & \Theta_{1313} + \Theta_{1331} & \Theta_{1323} + \Theta_{1332} \\ & & & & & \Theta_{2323} + \Theta_{2332} \end{pmatrix}. \quad (\text{A.3})$$

We also make use of the following implementation friendly matrix notation

for $\nabla^S \phi_k$,

$$E_k = \begin{bmatrix} \phi_{k,1} & 0 & 0 \\ 0 & \phi_{k,2} & 0 \\ 0 & 0 & \phi_{k,3} \\ \phi_{k,2} & \phi_{k,1} & 0 \\ 0 & \phi_{k,3} & \phi_{k,2} \\ \phi_{k,3} & 0 & \phi_{k,1} \end{bmatrix}. \quad (\text{A.4})$$

A.3 Neo-Hookean strain energy

For the numerical examples we have used the following Neo-Hookean strain-energy law

$$W(\mathbf{C}) = \frac{\mu}{2}(\text{tr}(\mathbf{C}) - 3) + \frac{\Lambda}{4}(J^2 - 1) - (\mu + \frac{\Lambda}{2})\ln(J - 1 + \phi_0). \quad (\text{A.5})$$

Thus, the resulting effective stress tensor is given by

$$\boldsymbol{\sigma}_e = \frac{\Lambda}{2} \left(J - \frac{1}{J - 1 + \phi_0} \right) \mathbf{I} + \mu \left(\frac{\mathbf{C}^T}{J} - \frac{\mathbf{I}}{J - 1 + \phi_0} \right), \quad (\text{A.6})$$

and the spatial tangent modulus tensor is given as

$$\boldsymbol{\Theta} = \boldsymbol{\Theta}_e + p(\mathbf{I} \otimes \mathbf{I} - 2\mathcal{Z}), \quad (\text{A.7})$$

where

$$\begin{aligned} \boldsymbol{\Theta}_e = & \left[\Lambda J - 2\mu \left(\frac{1}{2(J - 1 + \phi_0)} - \frac{J}{2(J - 1 + \phi_0)^2} \right) \right] \mathbf{I} \otimes \mathbf{I} \\ & + \left[\frac{2\mu}{J - 1 + \phi_0} - \Lambda(J - \frac{1}{J - 1 + \phi_0}) \right] \mathcal{B}, \end{aligned} \quad (\text{A.8})$$

and

$$\mathcal{B}_{ijkl} = \frac{1}{2}(\delta_{ik}\delta_{jl} + \delta_{il}\delta_{jk}), \quad \mathcal{Z}_{ijkl} = \delta_{ik}\delta_{jl}, \quad \mathbf{I} \otimes \mathbf{I} = \delta_{ij}\delta_{kl}. \quad (\text{A.9})$$

See [16, chapter 5] and [106, chapter 3] for further details.

Bibliography

- [1] Porous elasticity: Lectures on the elasticity of porous materials as an application of the theory of mixtures.
- [2] G. M. Albaiceta, L. Blanch, and U. Lucangelo. Static pressure–volume curves of the respiratory system: were they just a passing fad? *Current opinion in critical care*, 14(1):80–86, 2008.
- [3] E. Almeida and R. Spilker. Finite element formulations for hyperelastic transversely isotropic biphasic soft tissues. *Computer Methods in Applied Mechanics and Engineering*, 151(3):513–538, 1998.
- [4] P. R. Amestoy, I. S. Duff, and J. L'Excellent. Multifrontal parallel distributed symmetric and unsymmetric solvers. *Computer Methods in Applied Mechanics and Engineering*, 184(2):501–520, 2000.
- [5] C. Armstrong, W. Lai, and V. Mow. An analysis of the unconfined compression of articular cartilage. *Journal of Biomechanical Engineering*, 106:73–165, 1984.

- [6] C. Arthurs. *Effcient Simulation of Cardiac Electrical Propagation using Adaptive High-Order Finite Elements*. PhD thesis, University of Oxford, 2012.
- [7] L. Asner. *Effcient numerical methods for the solution of coupled multiphysics problems*. PhD thesis, University of Oxford, 2013.
- [8] G. A. Ateshian, S. Maas, and J. A. Weiss. Finite element algorithm for frictionless contact of porous permeable media under finite deformation and sliding. *Journal of Biomechanical Engineering*, 132(6):061006, 2010.
- [9] I. Babuška. Error-bounds for finite element method. *Numerische Mathematik*, 16(4):322–333, 1971.
- [10] S. Badia, A. Quaini, and A. Quarteroni. Coupling Biot and Navier-Stokes equations for modelling fluid-poroelastic media interaction. *Journal of Computational Physics*, 228(21):7986–8014, 2009.
- [11] H. Barucq, M. Madaune-Tort, and P. Saint-Macary. Some existence-uniqueness results for a class of one-dimensional nonlinear Biot models. *Nonlinear Analysis: Theory, Methods & Applications*, 61(4):591–612, 2005.
- [12] J. Bates. *Lung mechanics: an inverse modeling approach*. Cambridge University Press, 2009.

- [13] M. Bernabeu. *An open source HPC-enabled model of cardiac defibrillation of the human heart*. PhD thesis, University of Oxford, 2011.
- [14] P. Bochev and C. Dohrmann. A computational study of stabilized, low-order C₀ finite element approximations of Darcy equations. *Computational Mechanics*, 38(4):323–333, 2006.
- [15] R. Boer. *Trends in continuum mechanics of porous media*, volume 18. Springer, 2005.
- [16] J. Bonet and R. Wood. *Nonlinear continuum mechanics for finite element analysis*. Cambridge University Press, 1997.
- [17] R. Bordas, C. Lefevre, B. Veeckmans, J. Pitt-Francis, C. Fetita, D. Kay, S. Siddiqui, and K. Burrowes. Development and validation of patient-based complete conducting airways models. *PLoS ONE (submitted)*, 2014.
- [18] R. Bowen. Incompressible porous media models by use of the theory of mixtures. *International Journal of Engineering Science*, 18(9):1129–1148, 1980.
- [19] S. C. Brenner and L. R. Scott. *The mathematical theory of finite element methods*, volume 15. Springer, 2008.
- [20] F. Brezzi and M. Fortin. *Mixed and hybrid finite element methods*. Springer-Verlag, 1991.

- [21] F. Brezzi and M. Fortin. *Mixed and hybrid finite element methods*. Springer-Verlag New York, Inc., 1991.
- [22] E. Burman and P. Hansbo. A unified stabilized method for Stokes' and Darcy's equations. *Journal of Computational and Applied Mathematics*, 198(1):35–51, 2007.
- [23] D. Chapelle, J. Gerbeau, J. Sainte-Marie, and I. Vignon-Clementel. A poroelastic model valid in large strains with applications to perfusion in cardiac modeling. *Computational Mechanics*, 46(1):91–101, 2010.
- [24] D. Chapelle and P. Moireau. General coupling of porous flows and hyperelastic formulations—from thermodynamics principles to energy balance and compatible time schemes. *European Journal of Mechanics-B/Fluids*, 46:82–96, 2014.
- [25] P. G. Ciarlet. *The Finite Element Method for Elliptic Problems*. SIAM, classics in applied mathematics edition, 2002.
- [26] A. Cookson, J. Lee, C. Michler, R. Chabiniok, E. Hyde, D. Nordsletten, M. Sinclair, M. Siebes, and N. Smith. A novel porous mechanical framework for modelling the interaction between coronary perfusion and myocardial mechanics. *Journal of Biomechanics*, 45(5):850 – 855, 2012.
- [27] J. E. Cotes, D. J. Chinn, and M. R. Miller. *Lung function: physiology, measurement and application in medicine*. John Wiley & Sons, 2009.

- [28] O. Coussy. *Poromechanics*. John Wiley & Sons Inc, 2004.
- [29] O. Coussy, L. Dormieux, and E. Detournay. From mixture theory to biot's approach for porous media. *International Journal of Solids and Structures*, 35(34):4619–4635, 1998.
- [30] G. J. Criner, F. Cordova, A. L. Sternberg, and F. J. Martinez. The national emphysema treatment trial (nett) part ii: lessons learned about lung volume reduction surgery. *American Journal of Respiratory and Critical Care Medicine*, 184(8):881–893, 2011.
- [31] R. De Wilde, J. Clement, J. Hellemans, M. Decramer, M. Demedts, R. Boving, and K. Van de Woestijne. Model of elasticity of the human lung. *Journal of Applied Physiology*, 51(2):254–261, 1981.
- [32] D. A. Di Pietro and A. Ern. *Mathematical aspects of discontinuous Galerkin methods*, volume 69. Springer, 2011.
- [33] H. Elman, D. Silvester, and A. Wathen. *Finite elements and fast iterative solvers: with applications in incompressible fluid dynamics*. Oxford University Press, USA, 2005.
- [34] Q. Fang and D. A. Boas. Tetrahedral mesh generation from volumetric binary and grayscale images. In *Biomedical Imaging: From Nano to Macro, 2009. ISBI'09. IEEE International Symposium*, pages 1142–1145. IEEE, 2009.

- [35] X. Feng and Y. He. Fully discrete finite element approximations of a polymer gel model. *SIAM Journal on Numerical Analysis*, 48(6):2186–2217, 2010.
- [36] M. Feronato, N. Castelletto, and G. Gambolati. A fully coupled 3-D mixed finite element model of Biot consolidation. *Journal of Computational Physics*, 229(12):4813–4830, 2010.
- [37] A. D. Freed and D. R. Einstein. An implicit elastic theory for lung parenchyma. *International Journal of Engineering Science*, 62:31–47, 2013.
- [38] Y. Fung. Stress, deformation, and atelectasis of the lung. *Circulation Research*, 37(4):481–496, 1975.
- [39] C. J. Galbán, M. K. Han, J. L. Boes, K. A. Chughtai, C. R. Meyer, T. D. Johnson, S. Galbán, A. Rehemtulla, E. A. Kazerooni, F. J. Martinez, et al. Computed tomography-based biomarker provides unique signature for diagnosis of COPD phenotypes and disease progression. *Nature Medicine*, 18(11):1711–1715, 2012.
- [40] F. Galbusera, H. Schmidt, J. Noailly, A. Malandrino, D. Lacroix, H. Wilke, and A. Shirazi-Adl. Comparison of four methods to simulate swelling in poroelastic finite element models of intervertebral discs. *Journal of the Mechanical Behavior of Biomedical Materials*, 4(7):1234 – 1241, 2011.

- [41] P. Galie, R. Spilker, and J. Stegemann. A linear, biphasic model incorporating a Brinkman term to describe the mechanics of cell-seeded collagen hydrogels. *Annals of Biomedical Engineering*, 39:2767–2779, 2011.
- [42] O. Gonzalez and A. Stuart. *A first course in continuum mechanics*, volume 42. Cambridge University Press, 2008.
- [43] J. Haga, H. Osnæs, and H. Langtangen. On the causes of pressure oscillations in low-permeable and low-compressible porous media. *International Journal for Numerical and Analytical Methods in Geomechanics*, 36(12):1507–1522, 2012.
- [44] R. S. Harris. Pressure-volume curves of the respiratory system. *Respiratory Care*, 50(1):78–99, 2005.
- [45] K. Hedges. *A Computational Model of Forced Expiration Through Anatomical Airways in Health and Disease*. PhD Thesis, The University of Auckland, 2009.
- [46] H. Heinrich, M. Jenkinson, M. Brady, and J. A. Schnabel. MRF-based deformable registration and ventilation estimation of lung ct. *Medical Imaging, IEEE Transactions on*, 32(7):1239–1248, 2013.
- [47] M. Holmes and V. Mow. The nonlinear characteristics of soft gels and hydrated connective tissues in ultrafiltration. *Journal of Biomechanics*, 23(11):1145–1156, 1990.

- [48] G. Holzapfel, C. Schulze-Bauer, and M. Stadler. Mechanics of angioplasty: Wall, balloon and stent. *ASME Applied Mechanics*, 242:141–156, 2000.
- [49] M. Ismail, A. Comerford, and W. Wall. Coupled and reduced dimensional modeling of respiratory mechanics during spontaneous breathing. *International Journal for Numerical Methods in Biomedical Engineering*, 29(11):1285–1305, 2013.
- [50] N. Jahani, Y. Yin, E. A. Hoffman, and C.-L. Lin. Assessment of regional non-linear tissue deformation and air volume change of human lungs via image registration. *Journal of Biomechanics*, 47(7):1626–1633, 2014.
- [51] S. Kaushik, Z. Cleveland, G. Cofer, G. Metz, D. Beaver, J. Nouls, M. Kraft, W. Auffermann, J. Wolber, H. McAdams, et al. Diffusion-weighted hyperpolarized ^{129}Xe MRI in healthy volunteers and subjects with chronic obstructive pulmonary disease. *Magnetic Resonance in Medicine*, 2011.
- [52] A.-R. Khaled and K. Vafai. The role of porous media in modeling flow and heat transfer in biological tissues. *International Journal of Heat and Mass Transfer*, 46(26):4989–5003, 2003.
- [53] J. Kim, H. Tchelepi, and R. Juanes. Stability and convergence of sequential methods for coupled flow and geomechanics: Fixed-stress

- and fixed-strain splits. *Computer Methods in Applied Mechanics and Engineering*, 200(13):1591–1606, 2011.
- [54] B. S. Kirk, J. W. Peterson, R. H. Stogner, and G. F. Carey. libMesh: A C++ Library for Parallel Adaptive Mesh Refinement/Coarsening Simulations. *Engineering with Computers*, 22(3–4):237–254, 2006.
- [55] P. Kowalczyk. Mechanical model of lung parenchyma as a two-phase porous medium. *Transport in Porous Media*, 11(3):281–295, 1993.
- [56] P. Kowalczyk and M. Kleiber. Modelling and numerical analysis of stresses and strains in the human lung including tissue-gas interaction. *European Journal of Mechanics. A. Solids*, 13(3):367–393, 1994.
- [57] W. Lai and V. Mow. Drag-induced compression of articular cartilage during a permeation experiment. *Biorheology*, 17(1-2):111, 1980.
- [58] B. Lande and W. Mitzner. Analysis of lung parenchyma as a parametric porous medium. *Journal of Applied Physiology*, 101(3):926–933, 2006.
- [59] Lawrence Berkeley National Laboratory. LBNL LungLab Tour. <http://www.whywasteyourbreath.com/images.html>, 1995.
- [60] D. Leary, T. Winkler, A. Braune, and G. N. Maksym. Effects of airway tree asymmetry on the emergence and spatial persistence of ventilation defects. *Journal of Applied Physiology*, 117(4):353–362, 2014.

- [61] G. Lee, N. Tseng, and Y. Yuan. Finite element modeling of lungs including interlobar fissures and the heart cavity. *Journal of Biomechanics*, 16(9):679–690, 1983.
- [62] K. Leungchavaphongse. *Mathematical modelling of the liver microcirculation*. PhD thesis, Imperial College London, 2013.
- [63] M. Levenston, E. Frank, and A. Grodzinsky. Variationally derived 3-field finite element formulations for quasistatic poroelastic analysis of hydrated biological tissues. *Computer Methods in Applied Mechanics and Engineering*, 156(1-4):231–246, 1998.
- [64] C. Li, R. Borja, and R. Regueiro. Dynamics of porous media at finite strain. *Computer Methods in Applied Mechanics and Engineering*, 193(36):3837–3870, 2004.
- [65] H. Li and Y. Li. A discontinuous Galerkin finite element method for swelling model of polymer gels. *Journal of Mathematical Analysis and Applications*, 398(1):11–25, 2012.
- [66] X. Li, H. Holst, J. Ho, and S. Kleiven. Three dimensional poroelastic simulation of brain edema: Initial studies on intracranial pressure. In *World Congress on Medical Physics and Biomedical Engineering*, pages 1478–1481. Springer, 2010.
- [67] K. Lipnikov. *Numerical methods for the Biot model in poroelasticity*. PhD thesis, University of Houston, 2002.

- [68] R. Liu. *Discontinuous Galerkin finite element solution for poromechanics*. PhD thesis, The University of Texas at Austin, 2004.
- [69] S. A. Maas, B. J. Ellis, G. A. Ateshian, and J. A. Weiss. FEBio: finite elements for biomechanics. *Journal of Biomechanical Engineering*, 134(1):1–10, 2012.
- [70] B. Markert. A constitutive approach to 3-d nonlinear fluid flow through finite deformable porous continua. *Transport in Porous Media*, 70(3):427–450, 2007.
- [71] A. Masud and T. J. Hughes. A stabilized mixed finite element method for darcy flow. *Computer Methods in Applied Mechanics and Engineering*, 191(39):4341–4370, 2002.
- [72] V. Mow, S. Kuei, W. Lai, and C. Armstrong. Biphasic creep and stress relaxation of articular cartilage in compression: Theory and experiments. *Journal of Biomechanical Engineering*, 102:73–84, 1980.
- [73] M. A. Murad and A. F. Loula. On stability and convergence of finite element approximations of Biot’s consolidation problem. *International Journal for Numerical Methods in Engineering*, 37(4):645–667, 1994.
- [74] M. Ochs, J. R. Nyengaard, A. Jung, L. Knudsen, M. Voigt, T. Wahlers, J. Richter, and H. J. G. Gundersen. The number of alveoli in the human lung. *American Journal of Respiratory and Critical Care Medicine*, 169(1):120–124, 2004.

- [75] M. Owen and M. Lewis. The mechanics of lung tissue under high-frequency ventilation. *SIAM Journal on Applied Mathematics*, pages 1731–1761, 2001.
- [76] S. Patz, F. Hersman, I. Muradian, M. Hrovat, I. Ruset, S. Ketel, F. Jacobson, G. Topulos, H. Hatabu, and J. Butler. Hyperpolarized ^{129}Xe mri: A viable functional lung imaging modality? *European Journal of Radiology*, 64(3):335–344, 2007.
- [77] T. Pedley, R. Schroter, and M. Sudlow. Energy losses and pressure drop in models of human airways. *Respiration Physiology*, 9(3):371–386, 1970.
- [78] T. Pedley, R. Schroter, and M. Sudlow. The prediction of pressure drop and variation of resistance within the human bronchial airways. *Respiration Physiology*, 9(3):387–405, 1970.
- [79] P. J. Phillips and M. F. Wheeler. A coupling of mixed and continuous Galerkin finite element methods for poroelasticity i: the continuous in time case. *Computational Geosciences*, 11(2):131–144, 2007.
- [80] P. J. Phillips and M. F. Wheeler. A coupling of mixed and continuous Galerkin finite element methods for poroelasticity ii: the discrete-in-time case. *Computational Geosciences*, 11(2):145–158, 2007.
- [81] P. J. Phillips and M. F. Wheeler. Overcoming the problem of locking

in linear elasticity and poroelasticity: an heuristic approach. *Computational Geosciences*, 13(1):5–12, 2009.

- [82] V. M. Ranieri, R. Giuliani, T. Fiore, M. Dambrosio, and J. Milic-Emili. Volume-pressure curve of the respiratory system predicts effects of PEEP in ARDS: ‘occlusion’ versus ‘constant flow’ technique. *American Journal of Respiratory and Critical Care Medicine*, 149(1):19–27, 1994.
- [83] P.-A. Raviart and J.-M. Thomas. A mixed finite element method for 2-nd order elliptic problems. In *Mathematical aspects of finite element methods*, pages 292–315. Springer, 1977.
- [84] F. Rittner and M. Döring. *Curves and loops in mechanical ventilation*. Dräger Medical Incorporated, 2005.
- [85] M. Sauter and C. Wieners. Robust estimates for the approximation of the dynamic consolidation problem. *IMA Journal of Numerical Analysis*, 30(3):832–856, 2010.
- [86] R. Showalter. Diffusion in poro-elastic media. *Journal of Mathematical Analysis and Applications*, 251(1):310–340, 2000.
- [87] D. Silvester and A. Wathen. Fast iterative solution of stabilised stokes systems part ii: using general block preconditioners. *SIAM Journal on Numerical Analysis*, 31(5):1352–1367, 1994.

- [88] B. Suki and J. Bates. Lung tissue mechanics as an emergent phenomenon. *Journal of Applied Physiology*, 110(4):1111–1118, 2011.
- [89] A. Swan, A. Clark, and M. Tawhai. A computational model of the topographic distribution of ventilation in healthy human lungs. *Journal of Theoretical Biology*, 300(0):222 – 231, 2012.
- [90] M. Tawhai and C. Lin. Image-based modeling of lung structure and function. *Journal of Magnetic Resonance Imaging*, 32(6):1421–1431, 2010.
- [91] M. Tawhai, M. Nash, and E. Hoffman. An Imaging-based Computational Approach to Model Ventilation Distribution and Soft-tissue Deformation in the Ovine Lung. *Academic Radiology*, 13(1):113–120, 2006.
- [92] M. H. Tawhai, M. P. Nash, C.-L. Lin, and E. A. Hoffman. Supine and prone differences in regional lung density and pleural pressure gradients in the human lung with constant shape. *Journal of Applied Physiology*, 107(3):912–920, 2009.
- [93] V. Thomée. *Galerkin finite element methods for parabolic problems*, volume 25. Springer, 2006.
- [94] K. Ün and R. Spilker. A penetration-based finite element method for hyperelastic 3D biphasic tissues in contact. Part II: finite element simulations. *Journal of Biomechanical Engineering*, 128:934, 2006.

- [95] J. G. Venegas, T. Winkler, G. Musch, M. F. V. Melo, D. Layfield, N. Tgavalekos, A. J. Fischman, R. J. Callahan, G. Bellani, and R. S. Harris. Self-organized patchiness in asthma as a prelude to catastrophic shifts. *Nature*, 434(7034):777–782, 2005.
- [96] R. Verfürth. A posteriori error estimators for convection-diffusion equations. *Numerische Mathematik*, 80(4):641–663, 1998.
- [97] A.-T. Vuong, L. Yoshihara, and W. Wall. A general approach for modeling interacting flow through porous media under finite deformations. *Computer Methods in Applied Mechanics and Engineering*, 2014.
- [98] A. Wathen and D. Silvester. Fast iterative solution of stabilised stokes systems. part i: Using simple diagonal preconditioners. *SIAM Journal on Numerical Analysis*, 30(3):630–649, 1993.
- [99] L. Weichert. *Computational Modeling of Multi-Field and Multi-Scale Phenomena in Respiratory Mechanics*. PhD Thesis, Technischen Universität München, 2011.
- [100] R. Werner, J. Ehrhardt, R. Schmidt, and H. Handels. Patient-specific finite element modeling of respiratory lung motion using 4D CT image data. *Medical physics*, 36(5):1500–1511, 2009.
- [101] J. West. *Respiratory physiology: the essentials*. Lippincott Williams & Wilkins, 2008.

- [102] M. F. Wheeler and X. Gai. Iteratively coupled mixed and Galerkin finite element methods for poro-elasticity. *Numerical Methods for Partial Differential Equations*, 23(4):785–797, 2007.
- [103] J. White and R. Borja. Stabilized low-order finite elements for coupled solid-deformation/fluid-diffusion and their application to fault zone transients. *Computer Methods in Applied Mechanics and Engineering*, 197(49-50):4353–4366, 2008.
- [104] J. A. White and R. I. Borja. Block-preconditioned Newton–Krylov solvers for fully coupled flow and geomechanics. *Computational Geosciences*, 15(4):647–659, 2011.
- [105] B. Wirth and I. Sobey. An axisymmetric and fully 3D poroelastic model for the evolution of hydrocephalus. *Mathematical Medicine and Biology*, 23(4):363–388, 2006.
- [106] P. Wriggers. *Nonlinear finite element methods*. Springer Verlag, 2008.
- [107] S.-Y. Yi. A coupling of nonconforming and mixed finite element methods for Biot’s consolidation model. *Numerical Methods for Partial Differential Equations*, 2013.
- [108] Y. Yin, J. Choi, E. A. Hoffman, M. H. Tawhai, and C.-L. Lin. Simulation of pulmonary air flow with a subject-specific boundary condition. *Journal of Biomechanics*, 43(11):2159–2163, 2010.

- [109] Y. Yin, J. Choi, E. A. Hoffman, M. H. Tawhai, and C.-L. Lin. A multiscale MDCT image-based breathing lung model with time-varying regional ventilation. *Journal of Computational Physics*, 244:168–192, 2013.
- [110] A. Ženíšek. The existence and uniqueness theorem in Biot’s consolidation theory. *Aplikace Matematiky*, 29(3):194–211, 1984.
- [111] T. Zhang, N. P. Orton, T. R. Mackie, and B. R. Paliwal. Technical note: A novel boundary condition using contact elements for finite element based deformable image registration. *Medical Physics*, 31(9):2412–2415, 2004.